

Radial basis function collocation methods for band structure computation of phononic crystals

Thesis

in fulfillment of the requirements for the degree of
Doctor of Engineering (Dr.-Ing.)
at the School of Science and Technology
of the University of Siegen

by

Hui Zheng

First reviewer (Advisor): Prof. Dr.-Ing. habil. Dr. h. c. Chuanzeng Zhang

Second reviewer: Prof. Dr.-Ing. Ulrich P. Schmitz

Date of the oral examination: September 9th, 2016

ABSTRACT

The main aim of this thesis is to develop an accurate and efficient numerical tool based on the radial basis function collocation method (RBFCM) for the band structure calculations of elastic and acoustic waves in one-dimensional (1D) and two-dimensional (2D) phononic crystals. Some new numerical techniques are proposed to accurately deal with the derivative computations of the field quantities near/on the boundaries/interfaces required by the boundary conditions and the continuity conditions on the interfaces. By using these novel numerical techniques, the stability of the RBFCM can be significantly improved, which leads to an enhanced accuracy and efficiency. Both the global RBFCM (GRBFCM) and the local RBFCM (LRBFCM) are presented and discussed in the thesis. Then, the accuracy and the efficiency of the RBFCM are verified by the numerical results obtained by the finite element method (FEM), and applied to the band structure computations of 1D and 2D solid/solid as well as 2D solid/fluid and fluid/solid phononic crystals with different acoustic impedance mismatches, material combinations, scatterer shapes, and lattice forms. The effects of the key geometrical and material parameters on the band structures especially the bandgaps of 1D and 2D phononic crystals are also investigated and discussed.

Kurzfassung

Das Hauptziel dieser Arbeit ist es, ein genaues und effizientes numerisches Programm zu entwickeln, welches auf der Basis der radialen Basisfunktions-Kollokationsmethode (RBFCM) die Bandstrukturberechnung von elastischen und akustischen Wellen in eindimensionalen (1D) und zweidimensionalen (2D) phononischen Kristallen ermöglicht. Es werden einige neue numerische Techniken vorgeschlagen, um die Ableitungsberechnungen der Feldgrößen in der Nähe von oder auf den Rändern/Grenzflächen, welche für die Randbedingungen und die Kontinuitätsbedingungen an den Grenzflächen erforderlich sind, genau zu behandeln. Durch die Verwendung dieser neuartigen numerischen Techniken kann die Stabilität der RBFCM wesentlich gesteigert werden, was zu einer verbesserten Genauigkeit und Effizienz führt. Sowohl die globale RBFCM (GRBFCM) als auch die lokale RBFCM (LRBFCM) werden in der Arbeit vorgestellt und diskutiert. Anschließend werden die Genauigkeit und die Effizienz der RBFCM durch die mit der Finite-Elemente-Methode (FEM) erhaltenen numerischen Ergebnisse verifiziert, und die entwickelten RBFCM werden auf die Bandstrukturberechnung von 1D und 2D fest-festen sowie 2D fest-flüssigen und flüssig-festen phononischen Kristallen mit verschiedenen akustischen Impedanzunterschieden, Materialkombinationen, Streuerformen und Gitterformen angewandt. Die Auswirkungen der wichtigsten geometrischen und materiellen Parameter auf die Bandstrukturen, insbesondere auf die Bandlücken von 1D und 2D phononischen Kristallen werden ebenfalls untersucht und diskutiert.

Acknowledgments

This thesis was completed in the course of my research activity as a PhD candidate from 2012 to 2016 at the Chair of Structural Mechanics, Department of Civil Engineering, School of Science and Technology, University of Siegen, Germany.

I would like to sincerely thank my advisor, Prof. Dr.-Ing. habil. Dr. h. c. Chuanzeng Zhang for his instructive guidance, useful suggestions, and continuous support during my research. His help and patience have contributed greatly to this thesis. I am deeply grateful for his advices over the past years.

My sincere thanks to Prof. Dr.-Ing. Ulrich P. Schmitz as the second reviewer of my thesis for his precious time spent to read and check my thesis in details. I would like also to thank Prof. Dr.-Ing. Claus-Peter Fritzen and Prof. Dr.-Ing. Richard A. Herrmann acting as members of the Doctoral Commission for their time and effort.

I would like to express my thanks to my Master supervisor, Prof. Dr. Wen Chen, who has helped me with the great chance to pursue my PhD study in Germany. I would like to extend my thanks to Prof. Yuesheng Wang, Prof. Jan Sladek and Prof. Vladimir Sladek for many useful discussions related to my PhD research work. The time and effort they spent to my research work are highly appreciated. I would like to thank Prof. Šarler Božidar for offering me a chance to visit his research group.

I highly appreciate and acknowledge many helps and supports from Dr. Longtao Xie and other team members at the Chair of Structural Mechanics, Department of Civil Engineering, School of Science and Technology, University of Siegen, Germany. Additionally, my sincere thanks to Dr. Yanfeng Wang and Mr. Tianxue Ma, who have provided me a continuous support regarding the application of the software COMSOL Multiphysics. Thanks to Elias Perras, Pedro Villamil, and Benjamin Ankaý for the translation of the abstract of my PhD thesis. Thanks to Meike Stricker for her great helps and supports during my stay in Siegen, Germany.

Last but not least, I would like to thank my parents, my sister and her husband for their nonrestrictive love and support. This work was supported by the China Scholarship Council (CSC), which is gratefully acknowledged.

September 2016, Siegen

Hui Zheng

Contents

ABSTRACT	II
ACKNOWLEDGEMENTS	IV
LIST OF FIGURES	IX
LIST OF TABLES	XIV
LIST OF ABBREVIATIONS	XV

1 Introduction

1.1 Current state of research on phononic crystals	1
1.2 Numerical methods for band structure computations	5
1.3 Objectives of the thesis	8
1.4 Outline of the thesis	9

2 Governing equations of elastic and acoustic wave propagation in phononic crystals

2.1 1D elastic wave propagation	12
2.1.1 1D elastic wave equation	12
2.1.2 Interface continuity conditions	13
2.1.3 Periodic boundary conditions	14
2.2 2D anti-plane elastic wave propagation	14
2.2.1 2D anti-plane elastic wave equation	14
2.2.2 Interface continuity conditions	15
2.2.3 Periodic boundary conditions	16
2.3 2D in-plane elastic wave propagation	16
2.3.1 2D in-plane elastic wave equations	16
2.3.2 Interface continuity conditions	17
2.3.3 Periodic boundary conditions	17
2.4 2D mixed elastic and acoustic wave propagation	18
2.4.1 Elastic wave equations and acoustic wave equation	18

2.4.2	Interface continuity conditions	18
2.4.3	Periodic boundary conditions	19
2.4.3.1	Fluid scatterers embedded in an elastic matrix	19
2.4.3.2	Elastic scatterers embedded in a fluid matrix	19
3	Radial basis function collocation methods (RBFCM)	
3.1	Global radial basis function collocation method (GRBFCM)	20
3.2	Local radial basis function collocation method (LRBFCM)	22
3.3	Treatments of the boundary and interface continuity conditions	24
3.3.1	Dirichlet boundary conditions	24
3.3.2	Neumann boundary conditions	25
3.3.3	Interface continuity conditions	28
3.4	Summary	28
4	Global RBFCM for 1D solid/solid phononic crystals	
4.1	GRBFCM formulation for 1D solid/solid phononic crystals	31
4.2	Numerical results and discussions	32
4.2.1	Numerical results of the inverse MQ RBF	32
4.2.2	Numerical results of the Gaussian RBF	37
4.2.3	Numerical results of the MQ RBF	43
4.3	Summary	48
5	Local RBFCM for anti-plane wave propagation analysis in 2D solid/solid phononic crystals	
5.1	LRBFCM formulation of the eigenvalue problems	51
5.1.1	Discretized governing equations	51
5.1.2	Discretized interface continuity conditions	51
5.1.3	Discretized periodic boundary conditions of square lattice	52
5.1.4	Discretized periodic boundary conditions of triangular lattice	54
5.2	Numerical results and discussions	57

5.2.1	Effects of the shape parameter	57
5.2.2	Aurum scatterers embedded in epoxy matrix	58
5.2.3	Aluminum scatterers embedded in epoxy matrix	63
5.3	Analysis of the computational efficiency	67
5.4	Summary	69
6	Local RBFCM for in-plane elastic wave propagation analysis in 2D solid/solid phononic crystals	
6.1	LRBFCM formulation of the eigenvalue problems	70
6.1.1	Discretized governing equations	70
6.1.2	Discretized interface continuity conditions	71
6.1.3	Discretized periodic boundary conditions of square lattice	73
6.1.4	Discretized periodic boundary conditions of triangular lattice	76
6.2	Numerical results and discussions	77
6.2.1	Square and rectangular scatterers in square and triangular lattices	78
6.2.2	Circular scatterers in square and triangular lattices	82
6.2.3	Triangular scatterers in square and triangular lattices	85
6.3	Analysis of the computational efficiency	88
6.4	Summary	92
7	Local RBFCM for wave propagation analysis in 2D solid/fluid and fluid/solid phononic crystals	
7.1	LRBFCM formulation of the eigenvalue problems	94
7.1.1	Discretized governing equations	94
7.1.2	Discretized interface continuity conditions	95
7.1.3	Discretized periodic boundary conditions	96
7.1.3.1	Solid/fluid phononic crystals	96
7.1.3.1.1	Square lattice	97
7.1.3.1.2	Triangular lattice	97
7.1.3.2	Fluid/solid phononic crystals	98

7.1.3.2.1 Square lattice	98
7.1.3.2.2 Triangular lattice	99
7.1.4 Eigenvalue equations	101
7.1.4.1 Square lattice	101
7.1.4.2 Triangular lattice	103
7.2 Numerical results and discussions	104
7.2.1 Solid/fluid phononic crystals	104
7.2.2 Fluid/solid phononic crystals	111
7.3 Analysis of the computational efficiency	119
7.4 Summary	124
8 Conclusions and outlook	
8.1 Conclusions	125
8.2 Outlook	127
References	128

LIST OF FIGURES

1.1 1D, 2D and 3D phononic crystals.....	1
1.2 The band structures of Ni-Al composite: Ni/Al system with the filling fraction $f=0.1$ (left) and Al/Ni system with the filling fraction $f =0.75$ (right) for transverse waves.....	2
1.3 A phononic sculpture consisting of periodic steel cylinders (left), and the sound attenuation results (right).....	3
2.1 One-dimensional (1D) phononic crystal	12
2.2 A unit-cell of the 1D phononic crystal.....	13
2.3 The considered phononic crystal structures: (a1), (a2) and (a3) are the square lattice, its corresponding square unit-cell and the first Brillouin zone; (b1), (b2) and (b3) are the triangular lattice, its corresponding hexagonal unit-cell and the first Brillouin zone.....	15
3.1 Schematic sketch for the direct method.....	25
3.2 Schematic sketch for the indirect method.....	26
3.3 Schematic sketch for the fictitious nodes method.....	27
3.4 Special node distribution for a circular boundary.....	30
4.1 Band structure obtained by using inverse MQ RBF with $N=19$ and $\xi = 0.8$	33
4.2 Band structure obtained by using inverse MQ RBF with $N=19$ and $\xi = 0.9$	34
4.3 Band structure obtained by using inverse MQ RBF with $N=19$ and $\xi = 1.5$	34
4.4 Band structure obtained by using inverse MQ RBF with $N=9$ and $\xi = 1$	35
4.5 Band structure obtained by using inverse MQ RBF with $N=19$ and $\xi = 1$	36
4.6 Band structure obtained by using inverse MQ RBF with $N=29$ and $\xi = 1$	36
4.7 Band structure obtained by using inverse MQ RBF with $N=29$ and $\xi = 2$	37
4.8 Band structure obtained by using Gaussian RBF with $N=19$ and $\xi = 0.2$	38
4.9 Band structure obtained by using Gaussian RBF with $N=19$ and $\xi = 0.3$	38

4.10 Band structure obtained by using Gaussian RBF with $N=19$ and $\xi = 0.4$ 39

4.11 Band structure obtained by using Gaussian RBF with $N=19$ and $\xi = 0.6$ 39

4.12 Band structure obtained by using Gaussian RBF with $N=9$ and $\xi = 0.4$ 40

4.13 Band structure obtained by using Gaussian RBF with $N=19$ and $\xi = 0.4$ 41

4.14 Band structure obtained by using Gaussian RBF with $N=29$ and $\xi = 0.4$ 41

4.15 Band structure obtained by using Gaussian RBF with $N=29$ and $\xi = 0.2$ 42

4.16 Band structure obtained by using MQ RBF with $N=19$ and $\xi = 0.4$ 43

4.17 Band structure obtained by using MQ RBF with $N=19$ and $\xi = 0.5$ 44

4.18 Band structure obtained by using MQ RBF with $N=19$ and $\xi = 1$ 44

4.19 Band structure obtained by using MQ RBF with $N=19$ and $\xi = 1.2$ 45

4.20 Band structure obtained by using MQ RBF with $N=9$ and $\xi = 0.7$ 46

4.21 Band structure obtained by using MQ RBF with $N=19$ and $\xi = 0.7$ 46

4.22 Band structure obtained by using MQ RBF with $N=29$ and $\xi = 0.7$ 47

4.23 Band structure obtained by using MQ RBF with $N=29$ and $\xi = 0.5$ 47

5.1 Matrix and scatterer in a unit-cell of a square lattice.....52

5.2 Matrix and scatterer in a unit-cell of a triangular lattice.....55

5.3 Node distribution of the aurum/epoxy phononic crystal in a square lattice with square scatterers.....59

5.4 Band structure of the aurum/epoxy phononic crystal in a square lattice with square scatterers by the direct method.....59

5.5 Band structure of the aurum/epoxy phononic crystal in a square lattice with square scatterers by the fictitious nodes method.....60

5.6 Convergence rates of the averaged eigenvalues for the aurum/epoxy phononic crystal in a square lattice with square scatterers.....60

5.7 Band structure of the aurum/epoxy phononic crystal in a square lattice with square

scatterers by the fictitious nodes method (right) with strongly disordered node distribution (left).....	61
5.8 Band structure of the aurum/epoxy phononic crystal in a square lattice with square scatterers by the fictitious nodes method (right) with weakly disordered node distribution (left).....	61
5.9 Node distribution of the aurum/epoxy phononic crystal in a square lattice with circular scatterers.....	62
5.10 Band structure of the aurum/epoxy phononic crystal in a square lattice with circular scatterers by the direct and indirect methods.....	63
5.11 Band structure of the aurum/epoxy phononic crystal in a square lattice with circular scatterers by the fictitious nodes method.....	63
5.12 Node distribution of the aluminium/epoxy phononic crystal in a square lattice with triangular scatterers.....	64
5.13 Band structure of the aluminium/epoxy phononic crystal in a square lattice with triangular scatterers by the indirect/direct method.....	64
5.14 Band structure of the aluminium/epoxy phononic crystal in a square lattice with triangular scatterers by the fictitious nodes method.....	64
5.15 Node distribution of the aluminium/epoxy phononic crystal in a triangular lattice with square scatterers.....	65
5.16 Band structure of the aluminium/epoxy phononic crystal in a triangular lattice with square scatterers by the direct/indirect method.....	66
5.17 Band structure of the aluminium/epoxy phononic crystal in a triangular lattice with square scatterers by the fictitious nodes method.....	66
6.1 Node distribution in a square lattice with square scatterers (Green nodes for interface; Blue nodes for matrix; Red nodes for scatterer).....	79
6.2 Band structure of the aurum/epoxy phononic crystal in a square lattice with square scatterers.....	79
6.3 Band structure of the aluminium/epoxy phononic crystal in a square lattice.....	79
6.4 Convergence rate of the aluminium/epoxy phononic crystal in a square lattice with square scatterers.....	80

6.5 Node distribution of the phononic crystal in a triangular lattice.....	80
6.6 Band structure of the aurum/epoxy phononic crystal in a triangular lattice with rectangular scatterers.....	81
6.7 Band structure of the aluminium/epoxy phononic crystal in a triangular lattice with rectangular scatterers.....	81
6.8 Node distribution of a square lattice with circular scatterers.....	82
6.9 Band structure of the aurum/epoxy phononic crystal in a square lattice with circular scatterers.....	83
6.10 Band structure of the aluminium/epoxy phononic crystal in a square lattice with circular scatterers.....	83
6.11 Node distribution of a triangular lattice with circular scatterers.....	84
6.12 Band structure of the aurum/epoxy phononic crystal in a triangular lattice with circular scatterers.....	84
6.13 Band structure of the aluminium/epoxy phononic crystal in a triangular lattice with circular scatterers.....	85
6.14 Node distribution of the phononic crystal in a square lattice with triangular scatterers.....	86
6.15 Band structure of the aurum/epoxy phononic crystal in a square lattice with triangular scatterers.....	86
6.16 Band structure of the aluminium/epoxy phononic crystal in a square lattice with triangular scatterers.....	86
6.17 Node distribution of the phononic crystal in a triangular lattice with triangular scatterers.....	87
6.18 Band structure of the aurum/epoxy phononic crystal in a square lattice with triangular scatterers.....	87
6.19 Band structure of the aluminium/epoxy phononic crystal in a square lattice with triangular scatterers.....	87
7.1 Node distribution in a square lattice with square scatterers.....	106
7.2 Band structure of aluminum embedded in mercury.....	106
7.3 Band structure of iron embedded in air.....	107

7.4 Convergence rate of the averaged eigenvalues for the aluminum embedded in the mercury.....	107
7.5 Node distribution in a square lattice with circular scatterers.....	108
7.6 Band structure of aluminum embedded in mercury.....	108
7.7 Band structure of iron embedded in air.....	108
7.8 Node distribution in a triangular lattice with square scatterers.....	109
7.9 Band structure of iron embedded in water.....	109
7.10 Band structure of iron embedded in air.....	110
7.11 Node distribution in a triangular lattice with circular scatterers.....	110
7.12 Band structure of iron embedded in water.....	111
7.13 Band structure of iron embedded in air.....	111
7.14 Node distribution in a square lattice with square scatterers.....	113
7.15 Band structure of water embedded in iron.....	113
7.16 Band structure of air embedded in iron.....	114
7.17 Node distribution in a square lattice with square scatterers.....	114
7.18 Band structure of water embedded in iron.....	115
7.19 Band structure of air embedded in iron.....	115
7.20 Node distribution in a triangular lattice with square scatterers.....	116
7.21 Band structure of water embedded in iron.....	116
7.22 Band structure of air embedded in iron.....	117
7.23 Node distribution in a triangular lattice with circular scatterers.....	117
7.24 Band structure of water embedded in iron.....	118
7.25 Band structure of air embedded in iron.....	118

LIST OF TABLES

3.1 Radial basis functions of various kinds.....	21
3.2 Special techniques used for computing the normal derivatives of the primary field quantity.....	29
4.1 Relative errors by using inverse MQ RBF with fixed $N=19$	33
4.2 Relative errors by using inverse MQ RBF with fixed $\xi = 1$	35
4.3 Relative errors by using Gaussian RBF with fixed $N=19$	37
4.4 Relative errors by using Gaussian RBF with fixed $\xi = 0.4$	40
4.5 Relative errors by using MQ RBF with fixed $N=19$	43
4.6 Relative errors by using MQ RBF with fixed $\xi = 0.7$	46
4.7 The effects of the shape parameter and total node number.....	48
5.1 Computing time and accuracy comparisons.....	67
6.1 Computing time and accuracy comparisons (Al/epoxy).....	89
6.2 Computing time and accuracy comparisons (Au/epoxy).....	90
6.3 Computing time and accuracy comparisons (Al/epoxy).....	91
6.4 Computing time and accuracy comparisons (Au/epoxy).....	92
7.1 Computing time and accuracy comparisons for the aluminium/mercury phononic crystals.....	120
7.2 Computing time and accuracy comparisons for the iron/air phononic crystals.....	121
7.3 Computing time and accuracy comparisons for the water/iron phononic crystals.....	122
7.4 Computing time and accuracy comparisons for the air/iron phononic crystals.....	123

LIST OF ABBREVIATIONS

- MQ** - Multiquadrics
- PC** - Phononic Crystal
- TPS** - Thin Plate Splines
- PDE** - Partial Differential Equation
- RBF** - Radial Basis Function
- FEM** - Finite Element Method
- BEM** - Boundary Element Method
- PWE** - Plane Wave Expansion Method
- SEM** - Spectral Element Method
- MST** - Multiple Scattering Theory
- SAW** - Surface Acoustic Wave
- FDTD** - Finite Difference Time Domain Method
- DTNM** - Dirichlet to Neumann Map Method
- RBFCM** - RBF Collocation Method
- LRBFCM** - Local RBF Collocation Method
- GRBFCM** - Global RBF Collocation Method

Chapter 1

Introduction

1.1 Current state of research on phononic crystals

Phononic crystals are synthetic composite materials which are formed by a periodic arrangement of different materials, either in one-dimensional (1D), two-dimensional (2D) or three-dimensional (3D) as shown in Fig. 1.1 [1]. The constituent materials could be gas, solid or fluid. The periodic structure of such materials has a great influence on the wave propagation characteristics, and the Bloch waves are usually formed in phononic crystals. One of the main properties of the Bloch waves is the possible existence of phononic bandgaps, which represents the frequency ranges in which the waves are forbidden to propagate through the periodic composite structures [2]. In 1987, the term "Photonic Crystals" (PhCs) has been firstly used to describe the periodic dielectric structures that prevent certain wavelengths of the electromagnetic wave propagation [3, 4]. Later on, Ho and Yablonovitch respectively proved the existence of the bandgaps in the photonic crystals numerically and experimentally [5-7]. Since then, the photonic crystals have been manufactured and applied to many problems in engineering and sciences.

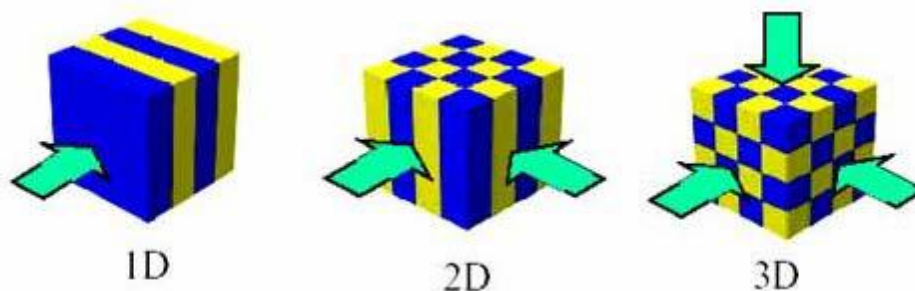


Fig. 1.1 1D, 2D and 3D phononic crystals [1].

(The arrows indicate the wave propagation directions).

The acoustic and elastic analogy of the photonic crystals is termed as phononic crystals, which may possess passbands and bandgaps for the acoustic or elastic wave

propagation in the acoustic/elastic periodic materials. The first known experimental investigation of phononic crystals was in 1979, although they were not referred to as as phononic crystals [8]. As for theoretical works, Kushwaha was the first to calculate the complete band structures for periodic elastic composites in 1993 [9], as shown in Fig. 1.2. In 1995, Martinez-Sala has made a sound attenuation experiment in a sculpture, and firstly reported the bandgaps experimentally [10], as shown in Fig. 1.3. However, the first complete phononic bandgap was only observed in the frequency range between 1000 and 1120 kHz in 1998 by Montero de Espinosa [11]. In recent years, different types of materials (elastic, piezoelectric, piezomagnetic, fluid, soft materials, etc.) and material combinations (solid/solid, fluid/fluid, solid/fluid, and fluid/solid) are used in the fabrication of phononic devices, which allows significant improvements on the reachable frequencies for the bandgaps [12, 13].

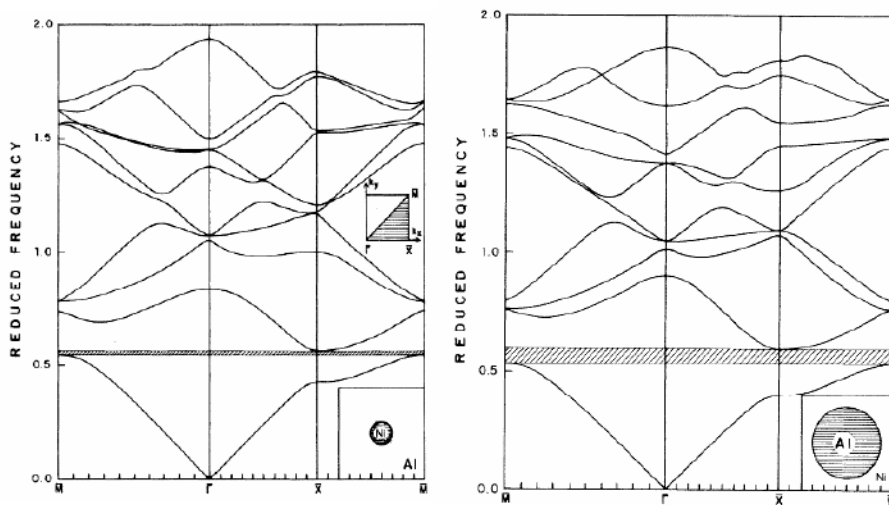


Fig. 1.2 The band structures of Ni-Al composite: Ni/Al system with the filling fraction $f=0.1$ (left), and Al/Ni system with the filling fraction $f=0.75$ (right) for transverse waves. The hatched areas designate bandgaps [14].

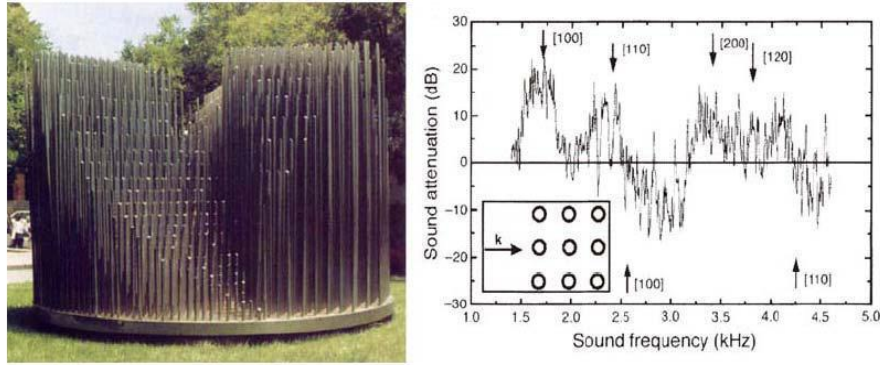


Fig. 1.3 A phononic sculpture consisting of periodic steel cylinders (left), and the sound attenuation results (right) [10].

In phononic crystal structures, complete bandgaps may appear which are independent of the direction of the acoustic or elastic wave propagation. In contrast, when bandgaps are only for certain directions of the wave propagation, they are referred to as directional bandgaps. Within the bandgaps, the phononic crystal behaves as a perfect non-absorbing acoustic mirror of the incident waves at the corresponding frequencies. The central frequency of the bandgap is determined by the size, periodicity, filling and arrangement of the scatterers or inclusions. There are two main physical mechanisms to explain the bandgap phenomena in phononic crystals. One is based on the Bragg-scattering theory, which describes the diffraction of the acoustic or elastic waves by the scatterers or inclusions [15]. However, according to the Bragg-scattering theory, the periodicity of the phononic crystal structures must be strictly preserved, which may limit their practical applications. The second mechanism was introduced later in 2000 by [16], who proposed a new type of periodic phononic structures with three material components, which are often termed as the locally resonant phononic structures. When such periodic structures are excited by the incident acoustic or elastic waves at certain frequencies, the scatterers resonant and interact with the incident waves stops the wave propagation and thus results in the bandgaps. In comparison to the Bragg-scattering mechanism, the locally resonant mechanism has two essential advantages: 1.) The wave-length related to the bandgaps could be much larger than the lattice constant, and 2.) the scatterers could be not

strictly periodically distributed. The band structure of the locally resonant phononic crystals is mainly dependent on the resonant structures of the scatterers rather than the lattice constant [17]. Further works on locally resonant phononic crystals can be found for instance in [18-21].

It is difficult to realize a perfect periodicity in the engineering applications, this difficulty in the real engineering may lead to the defect or disordered states and the localizations of the acoustic or elastic waves in phononic crystals [22-31]. Phononic crystal structures with a quasi-periodicity or random disorders were investigated in [32-35]. Previous works have shown that the acoustic or elastic waves could be trapped inside the point or line defect and therefore cannot propagate through the phononic crystals. Based on this fact, a directional tuning and a localization could be achieved to guide the propagation of the acoustic or elastic waves by introducing certain kinds of defects, such as by replacing or removing some of the scatterers in a phononic crystal, or by changing their periodic arrangement irregular. Control and manipulation of the acoustic and elastic wave propagation by intentionally imposing some kinds of the defects into the periodic structures is an important research topic of phononic crystals.

Besides the wave localization by defects, the surface localization of the acoustic and elastic waves is another important characteristic of the phononic crystals. When the Bloch waves propagate near the surface, the wave energy can be localized near the surface under certain conditions. The amplitude of the surface waves decreases as the distance from an interior observation point to the surface increases. Surface acoustic waves (SAWs) have many important applications in the engineering and sciences [36-41]. Hence, it is still a top research subject of phononic crystals.

According to the aforementioned facts, there are many promising and innovative applications of the phononic crystals in engineering and sciences. The bandgap theory has already been applied to the fish school structure, trees planting distribution, acoustic rectifier and so on [42-45]. The wave tuning and localization by defects can be utilized in the design of acoustic filters, wave guides, wave couplers and wave splitters [46-49]. The band structures of phononic crystals may also lead to negative

refractions, negative effective mass density, negative effective elastic moduli, which can be applied to focusing and directional control of the acoustic and elastic waves, and so on [50-53].

1.2 Numerical methods for band structure computations

Due to the wide-range and promising applications of the phononic crystals, different numerical methods have been developed to calculate the band structures of the phononic crystals, such as the plane wave expansion (PWE) method, the multiple scattering theory (MST), the wavelet method, the finite difference time domain (FDTD) method, the finite element method (FEM) the boundary element method (BEM), the Dirichlet-to-Neumann map (DtN-map) method, the spectral element method (SEM), the radial basis function collocation methods (RBFCM) and so on. However, each of these numerical methods has its advantages and disadvantages, which are briefly reviewed in the following.

The plane wave expansion (PWE) method is one of the most popular methods in phononic band structure calculations [54-58]. It considers the periodic composite structure as an inhomogeneous continuous medium, and takes the displacements, the elastic constants and the mass density as periodic functions in the space. By considering the Bloch-theorem and using Fourier-series, the inhomogeneous wave equations are expanded into an infinite series form in the first Brillouin zone. The PWE method has already been applied to many cases of phononic crystals [59-63]. However, the PWE method is inaccurate in dealing with phononic crystals with large acoustic impedance mismatches between the scatterers and the matrix, especially for the solid/fluid and fluid/solid phononic band structure calculations, which requires some special techniques [64, 65].

The finite element method (FEM) is an important and general-purpose numerical technique in almost every field of engineering and sciences, and it has been indeed applied to the phononic band structure calculations [66-70]. However, the FEM is not quite suitable for handling the imperfect interfaces, because different unit-cell must be adopted according to the interface conditions. When dealing with those phononic

crystals with a high acoustic impedance ratio, such as solid/fluid or fluid/solid phononic crystals [71], a large number of elements must be used, which may reduce the efficiency of the FEM.

The finite difference time domain method (FDTD) is also very common in the band structure analysis of the phononic crystals [72-75]. When evaluating the wave band structures, the FDTD always considers the time- and the space-dependences of the problems together, and then the eigenvalues will be obtained by using the Fast Fourier-transform (FFT) from the time-domain to the frequency-domain. This procedure is quite time consuming, and also a large number of grids are needed when dealing with the solid/fluid or fluid/solid phononic systems by the FDTD method.

The Dirichlet-to-Neumann (DtN) map method uses too many small matrices and is only suitable for simple scatterer shapes such as circular and spherical scatterers [76-81]. The complicated fundamental solutions and the singularity problems in the boundary element method (BEM) could limit its wide applications, especially in 3D cases [82-88].

The meshless methods have been developed and applied to many problems of engineering and sciences in the past two decades, including fluid dynamics, solid mechanics, and so on [89-93]. Due to their wide-range applications, many application examples of various kinds can be found in the literature [94-97]. Among several types of the meshless methods, one of them is based on the radial basis functions (RBFs) and especially useful [98]. In 1990s, Kansa first utilized the RBFs to deal with the multivariate data for the solution of the partial differential equations (PDEs), which is known as the Kansa's method or the RBF collocation method (RBFCM) [99, 100]. The advantages of the RBFCM for solving PDEs lie in its simplicity, broad applicability to various kinds of problems, high accuracy and effectiveness in dealing with complicated geometries. Different from the general idea of the RBFCM, many other variants of the meshless methods have been also proposed and developed, such as the finite point method (FPM) [101], the meshless local Petrov-Galerkin method (MLPGM) [102], the method of fundamental solution (MFS) [103], the boundary knot method (BKM) [104], and so on [105-107]. The existence, uniqueness and

convergence of the RBFCM have been extensively studied [108, 109]. However, in the RBFCM simulation process, an asymmetric and fully populated matrix of a system of the linear equations will be generated, which may cause a high condition number and affect the stability of the method. In order to deal with the asymmetric matrix, some methods have been proposed and developed to avoid the difficulties associated with the asymmetric matrix, such as the RBF Hermite-collocation method [110], the modified Kansa's method (MKM) [111]. However, the matrix generated in both symmetric and asymmetric RBFCM still remains a fully populated matrix, thus the computational cost and the condition number are becoming large as the number of the nodes increases. For the above mentioned reasons, the applications of the conventional global RBFCM (GRBFCM) are limited to small-scale problems. Many techniques have been suggested to reduce the computational cost and the condition number of the system matrix in the RBFCM, such as the domain decomposition method [112, 113], the multi-grid approach [114], the improved truncated singular valued decomposition (SVD) method [115], the compactly supported RBFs [116], the greedy algorithm [117, 118], the extended precision arithmetic [119], and so on [114, 115, 120, 121]. All these techniques bring a substantial complication of the original GRBFCM. However, one of the significant improvements is the local RBF collocation method (LRBFCM) or RBF finite difference method (RBF-FD) [121]. The key feature of the LRBFCM is that the collocation takes place on overlapping local domains, which could reduce the size of the collocation matrix without a remarkable loss of the accuracy. As the efficiency of the LRBFCM becomes improved in comparison with its global version, it has been applied to many complicated problems, including large-scale industrial problems [122-124]. Another numerical trouble in both the GRBFCM and the LRBFCM is the existence of the unbalanced errors between the approximated quantities near or on the boundaries and in the interior domain, which limits the applications of the RBFCM [125]. To overcome this difficulty, the technique of the weighted boundary conditions has been suggested to keep the errors in the interior domain and near or on the boundaries almost on the same level [126]. However, how to weight the boundary conditions and the interface

continuity conditions in multi-domain composite structures and in elastodynamics still remains an unresolved problem, and only few works can be found in the literature[127, 128]. In particular, the formulations and the applications of the GRBFCM and LRBFCM for band structure computations of the acoustic and elastic waves in phononic crystals or periodic structures have been very rarely reported so far.

There are also several other methods, such as the transfer matrix method [32-34], the lumped-mass method [129], the variational method [130] and so on [2, 39, 131-134], but they are rather limited to special geometrical configurations or material combinations. It should be mentioned here that none of the above mentioned methods is perfect for every case of the phononic crystals. Thus, there is still a great demand on developing more efficient and accurate numerical methods to simulate the wave propagation phenomena in phononic crystals.

1.3 Objectives of the thesis

Motivated by the above mentioned facts, the present thesis is devoted to the development and applications of the RBFCMs for band structure computations of the acoustic and elastic waves in one-dimensional (1D) and two-dimensional (2D) phononic crystals or periodic structures. The primary objectives of the thesis are:

- Formulation and numerical implementation of a global RBFCM or GRBFCM for the band structure computations of the elastic waves in 1D solid/solid phononic crystals.
- Formulation and numerical implementation of a local RBFCM or LRBFCM for the band structure computations of the anti-plane elastic waves in 2D solid/solid phonon crystals.
- Formulation and numerical implementation of a LRBFCM for the band structure computations of the in-plane elastic waves in 2D solid/solid phononic crystals.
- Formulation and numerical implementation of a LRBFCM for band structure computations of the elastic/acoustic waves in 2D solid/fluid phononic crystals (solid scatterers embedded in a fluid matrix) and fluid/solid phononic crystals (fluid scatterers embedded in a solid matrix).

- Development of novel techniques for computing the derivatives of the field quantities near or on the boundaries and the interfaces between the scatterer and the matrix, to improve the stability and the accuracy of the RBFCM.
- Verification and applications of the developed RBFCM for band structure computations of elastic/acoustic waves in 1D and 2D phononic crystals for different acoustic impedance ratios (small to large), material combinations (solid/fluid or fluid/solid), scatterers' shapes (rectangular, circular or triangular) and lattice forms (square and triangular).
- Investigation of the wave propagation phenomena, especially the passbands and the bandgaps, in 1D and 2D phononic crystals.

1.4 Outline of the thesis

In this introductory chapter, the concept and the applications of the phononic crystals are described, and the numerical techniques especially the RBFCM for the band structure computations of phononic crystals are briefly reviewed and discussed.

In Chapter 2, the governing equations, the periodic boundary conditions, and the interface continuity conditions for elastic and wave propagation problems in one-dimensional (1D) and two-dimensional (2D) periodic structures are formulated. In particular, the wave propagation problems of 1D elastic waves, 2D anti-plane elastic waves, 2D in-plane elastic waves and 2D mixed elastic/acoustic waves in periodic structures are described and discussed.

In Chapter 3, the key steps of the global RBFCM and local RBFCM (LRBFCM) are presented and discussed in details. Special numerical techniques are proposed to accurately compute the spatial derivatives of the field quantities near or on the boundaries and interfaces, which are required for the treatments of the interface and boundary conditions. The suggested special numerical techniques improve the stability of the RBFCM significantly.

Chapter 4 is devoted to the global RBFCM and its applications to the band structure calculations of 1D solid/solid phononic crystals. The stability of the global RBFCM for 1D solid/solid phononic crystals is tested by using three types of the

RBFs. The numerical results obtained with different node distributions and shape parameters are verified by comparing them with the exact solutions. Some useful relationships between the shape parameter and the node distribution are established and suggested.

In Chapter 5, the LRBFCM is presented and applied to the band structure computations of the 2D anti-plane elastic waves propagating in 2D solid/solid phononic crystals. The LRBFCM formulation to discretize the governing equation of the anti-plane elastic waves, the periodic boundary conditions and the interface continuity conditions in 2D solid/solid phononic crystals is derived, which results in an eigenvalue problem for computing the elastic wave band structures. The direct method, indirect method and fictitious nodes method are applied and compared to deal with the boundary and interface continuity conditions. The numerical efficiency of the developed LRBFCM in comparison with the FEM is investigated and discussed in details.

Chapter 6 presents the LRBFCM and its applications to the band structure calculations of the in-plane elastic waves in 2D solid/solid phononic crystals. The corresponding eigenvalue problem is formulated by using the discretized equations of the elastic wave motion, the periodic boundary conditions of the unit-cell and the interface continuity conditions between the scatterer and the matrix, based on LRBFCM for the in-plane elastic waves propagating in 2D solid/solid phononic crystals. For different acoustic mismatches, scatterer shapes and lattice forms, numerical results are presented and compared with the FEM results. The efficiency of the present LRBFCM is analysed and discussed by comparing the numerical results with those of the FEM.

In Chapter 7, the LRBFCM is developed and applied to the band structure calculations of the mixed elastic/acoustic wave propagation problems in 2D solid/fluid and fluid/solid phononic crystals. Here, both the elastic solid scatterers embedded into a fluid matrix and the fluid scatterers embedded into an elastic solid matrix are considered. The LRBFCM is developed to discretize the governing equations of the wave motion, the periodic boundary conditions of the unit-cell and

the continuity conditions on the interface between the scatterer and the matrix, which results in an eigenvalue problem for computing the band structures of the elastic-acoustic wave propagating in 2D solid/fluid and fluid/solid phononic crystals. The stability, accuracy and efficiency of the developed LRBFCM are verified by comparing the numerical results with those obtained by the FEM. The effects of the materials combination (solid elastic scatterers in a fluid matrix or fluid scatterers in an elastic solid matrix), the scatterer shapes (square and circular) and the lattice forms (square and triangular) on the band structures of the elastic/acoustic waves in 2D solid/fluid and fluid/solid phononic crystals are also revealed and discussed.

In the last chapter, the essential conclusions from this thesis are given and some related future works are pointed out.

Chapter 2

Governing equations of elastic and acoustic wave propagation in phononic crystals

2.1 1D elastic wave propagation

2.1.1 1D elastic wave equation

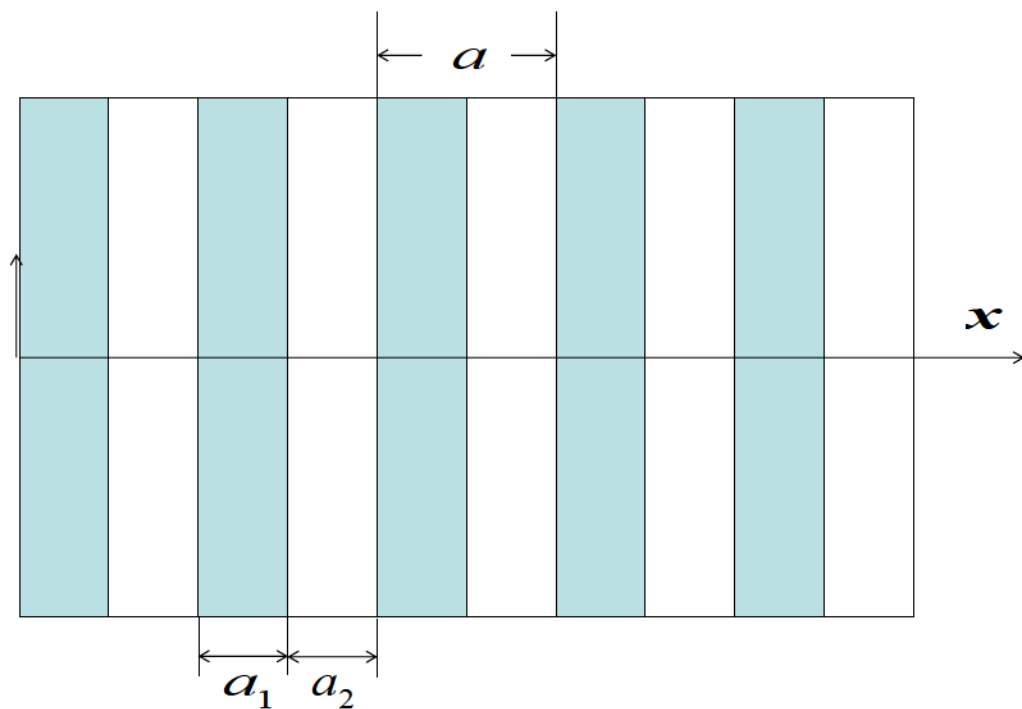


Fig. 2.1 One-dimensional (1D) phononic crystal.

Fig. 2.1 depicts an infinite periodic composite structure or one-dimensional phononic crystal that consists of the material 1 and the material 2. In this case, the time-harmonic elastic wave propagation can be described by

$$\frac{d^2 u^j}{dx^2} = -\frac{\omega^2}{c_j^2} u^j, \quad j=1, 2, \quad (2.1.1)$$

where

$$u^j = \begin{cases} u_x^j, & \text{longitudinal wave,} \\ u_z^j, & \text{anti-plane transverse wave} \end{cases}$$

denotes the longitudinal or the anti-plane displacement of the material j ($j=1,2$), ω is the circular frequency,

$$c_j = \begin{cases} \sqrt{E_j / \rho_j}, & \text{longitudinal wave,} \\ \sqrt{\mu_j / \rho_j}, & \text{anti-plane transverse wave} \end{cases}$$

denotes the longitudinal and the transverse wave speed, $E_j = \frac{\mu_j(3\lambda_j + 2\mu_j)}{\lambda_j + \mu_j}$ is the

Young's modulus with λ_j and μ_j being Lamé's constants, ρ_j is the mass density, and $j=1, 2$ represents the material 1 and 2. For the sake of brevity, the common term $e^{i\omega t}$ in all field quantities is omitted throughout the thesis, where i is the imaginary unit.

2.1.2 Interface continuity conditions

Due to the periodicity of the 1D phononic crystal structure and based on the Bloch-theorem, only a unit-cell has to be considered as shown in Fig. 2.2. Here, Γ_1 and Γ_2 are the boundaries of the unit-cell, Γ_0 is the interface between the two neighbouring sub-layers D_1 and D_2 denote the domains of the two materials, $a = a_1 + a_2$ is the 1D lattice constant or the length of a unit-cell of the 1D phononic crystal.

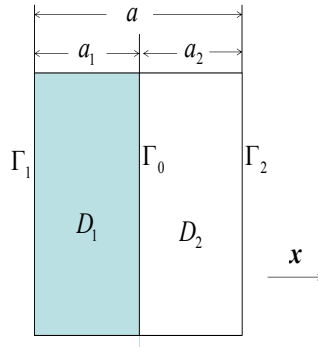


Fig. 2.2 A unit-cell of the 1D phononic crystal.

On the interface $\mathbf{x} \in \Gamma_0$, the displacement and stress continuity conditions are given by

$$u^1(\mathbf{x}_{\Gamma_0}) = u^2(\mathbf{x}_{\Gamma_0}), \quad (2.1.2)$$

$$\sigma^1(\mathbf{x}_{\Gamma_0}) = \sigma^2(\mathbf{x}_{\Gamma_0}), \quad (2.1.3)$$

where

$$\sigma^j = \begin{cases} E_j \frac{du_x^j}{dx}, & \text{longitudinal wave,} \\ \mu_j \frac{du_z^j}{dx}, & \text{anti-plane transverse wave,} \end{cases}$$

represents the stress component in the material j ($j=1,2$).

2.1.3 Periodic boundary conditions

According to the Bloch-theorem, the general displacement solution in the 1D phononic crystal can be written as

$$u(x+a) = u(x)e^{ika}, \quad (2.1.4)$$

where k is the wave vector. With Eq. (2.1.4), the periodic boundary conditions of the unit-cell can be stated as follows

$$u^1(\mathbf{x}_{\Gamma_1}) = e^{-ika} u^2(\mathbf{x}_{\Gamma_2}), \quad (2.1.5)$$

$$\sigma^1(\mathbf{x}_{\Gamma_1}) e^{-ika} = \sigma^2(\mathbf{x}_{\Gamma_2}), \quad (2.1.6)$$

where $u^1(\mathbf{x}_{\Gamma_1})$, $u^2(\mathbf{x}_{\Gamma_2})$, $\sigma^1(\mathbf{x}_{\Gamma_1})$ and $\sigma^2(\mathbf{x}_{\Gamma_2})$ denote the displacement and the stress component located on the boundaries Γ_1 and Γ_2 , respectively.

2.2 2D anti-plane elastic wave propagation

2.2.1 2D anti-plane elastic wave equation

A 2D phononic crystal is composed of straight and infinite cylinders of a square or triangular array with the lattice constant a , as shown in Fig. 2.3. The cross-sections of the inner domains or scatterers might be arbitrary. If the propagation of the elastic

wave is in the transverse plane (x - y plane) normal to the cylinder axis (z -axis), then we have the anti-plane transverse wave mode with the displacement perpendicular to the cylinders. The governing equation describing the anti-plane transverse wave motion can be expressed as

$$\mu_j \Delta u_j(\mathbf{x}) + \rho_j \omega^2 u_j(\mathbf{x}) = 0, \quad (j = 0, 1), \quad (2.2.1)$$

where Δ is the Laplace operator, u is the displacement along the z -direction, ω is the circular frequency, ρ and μ are the mass density and the shear modulus, respectively. The quantities with the subscript “0” are referred to the matrix, while those with the subscript “1” are to the scatterers.

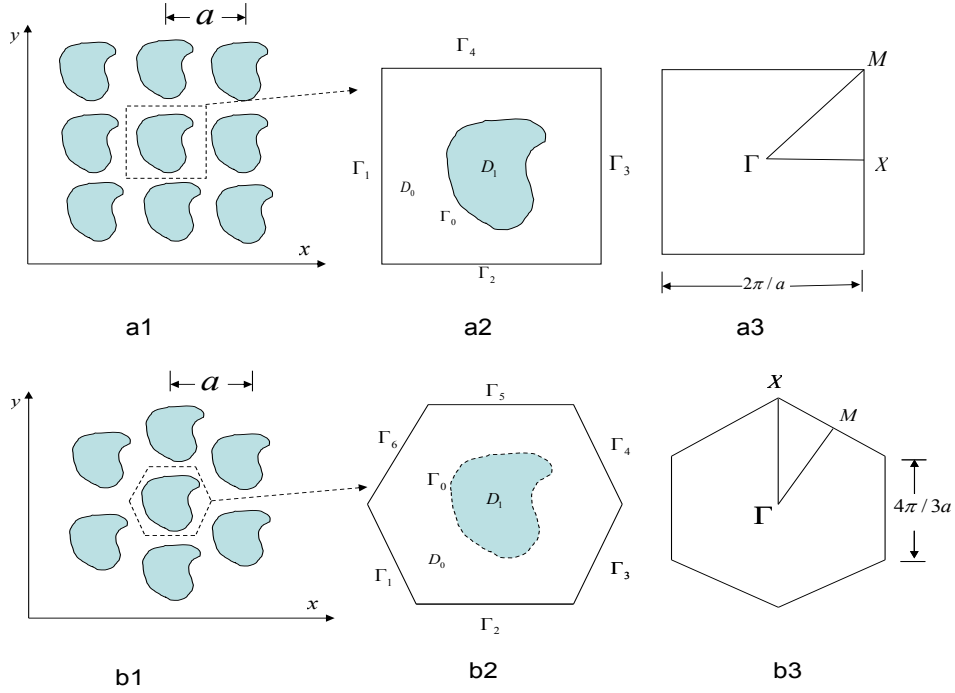


Fig. 2.3 The considered phononic crystal structures: (a1), (a2) and (a3) are the square lattice, its corresponding square unit-cell and the first Brillouin zone; (b1), (b2) and (b3) are the triangular lattice, its corresponding hexagonal unit-cell and the first Brillouin zone.

2.2.2 Interface continuity conditions

According to the Bloch theorem, the elastic wave field are expressed as a periodic function in the phononic crystal structure. In this thesis, the periodic conditions are only applied to the boundaries in a unit-cell. The continuity conditions at the interface

between the matrix and the scatterer are employed as follows

$$u_1(\mathbf{x}_{\Gamma_0}) = u_0(\mathbf{x}_{\Gamma_0}), \quad \mathbf{x}_{\Gamma_0} \in \Gamma_0, \quad (2.2.2)$$

$$T_1(\mathbf{x}_{\Gamma_0}) = T_0(\mathbf{x}_{\Gamma_0}), \quad \mathbf{x}_{\Gamma_0} \in \Gamma_0, \quad (2.2.3)$$

where $T_1(\mathbf{x})$ and $T_0(\mathbf{x})$ are the traction vectors. $T(\mathbf{x})$ in the anti-plane elastic problems can be expressed as

$$T(\mathbf{x}) = \mu \frac{\partial u(\mathbf{x})}{\partial \mathbf{n}}, \quad (2.2.4)$$

where $\mathbf{n} = (n_x, n_y)^T$ is the unit normal vector perpendicular to the interface.

2.2.3 Periodic boundary conditions

By using the Bloch theorem, the displacement of anti-plane elastic wave can be expressed as

$$u(\mathbf{x} + \mathbf{a}) = e^{i\mathbf{k} \cdot \mathbf{a}} u(\mathbf{x}), \quad (2.2.5)$$

$$T(\mathbf{x} + \mathbf{a}) = e^{i\mathbf{k} \cdot \mathbf{a}} T(\mathbf{x}), \quad (2.2.6)$$

where $\mathbf{k} = (k_x, k_y)$ is the Bloch wave vector composed from the reciprocal lattice vectors \mathbf{b}_i ($\mathbf{a}_i \cdot \mathbf{b}_j = 2\pi\delta_{ij}$), $u(\mathbf{x})$ and $T(\mathbf{x})$ are the displacement and the traction satisfying the Bloch periodicity conditions. $i = \sqrt{-1}$, $\mathbf{a} = m_1\mathbf{a}_1 + m_2\mathbf{a}_2$ with $\mathbf{m} = (m_1, m_2) \in Z^2$, \mathbf{a}_1 and \mathbf{a}_2 are the fundamental translation vectors of the lattices. On the boundary of the unit-cell, the Bloch periodic condition (2.2.5) and (2.2.6) apply.

2.3 2D in-plane elastic wave propagation

2.3.1 2D in-plane elastic wave equations

Let us consider time-harmonic in-plane elastic waves propagating in 2D phononic crystals as shown in Fig. 2.3. The elastic waves are propagating in the xy -plane, and the corresponding elastodynamic governing equations in the absence of body forces

are given by

$$(\lambda_j + 2\mu_j) \frac{\partial^2 u_x^j(\mathbf{x})}{\partial x^2} + \mu_j \frac{\partial^2 u_x^j(\mathbf{x})}{\partial y^2} + (\lambda_j + \mu_j) \frac{\partial^2 u_y^j(\mathbf{x})}{\partial x \partial y} = -\rho_j \omega^2 u_x^j(\mathbf{x}) \quad (2.3.1)$$

$$(\lambda_j + 2\mu_j) \frac{\partial^2 u_y^j(\mathbf{x})}{\partial y^2} + \mu_j \frac{\partial^2 u_y^j(\mathbf{x})}{\partial x^2} + (\lambda_j + \mu_j) \frac{\partial^2 u_x^j(\mathbf{x})}{\partial x \partial y} = -\rho_j \omega^2 u_y^j(\mathbf{x}) \quad (2.3.2)$$

where λ_j , ρ_j and μ_j are the Lamé's constant, mass density and shear modulus, u_x^j and u_y^j are the displacements in the x - and y -directions, ω is the circular frequency, and $j = 0, 1$ denotes domain D_j .

2.3.2 Interface continuity conditions

On the interface Γ_0 , the displacement continuity conditions and the traction equilibrium conditions of in-plane elastic problem can be written as

$$u_x^1(\mathbf{x}) = u_x^0(\mathbf{x}), \quad u_y^1(\mathbf{x}) = u_y^0(\mathbf{x}), \quad \mathbf{x} \in \Gamma_0, \quad (2.3.3)$$

$$T_x^1(\mathbf{x}) = T_x^0(\mathbf{x}), \quad T_y^1(\mathbf{x}) = T_y^0(\mathbf{x}), \quad \mathbf{x} \in \Gamma_0, \quad (2.3.4)$$

where $u_x(\mathbf{x})$ and $u_y(\mathbf{x})$ are the displacement components in x - and y -directions, respectively. $T_x(\mathbf{x})$ and $T_y(\mathbf{x})$ are the traction components in x - and y -directions.

2.3.3 Periodic boundary conditions

According to the Bloch theory, the displacements and the tractions of the in-plane elastic wave can be expressed as

$$u_x(\mathbf{x} + \mathbf{a}) = e^{ik \cdot \mathbf{a}} u_x(\mathbf{x}), \quad u_y(\mathbf{x} + \mathbf{a}) = e^{ik \cdot \mathbf{a}} u_y(\mathbf{x}), \quad (2.3.5)$$

$$T_x(\mathbf{x} + \mathbf{a}) = e^{ik \cdot \mathbf{a}} T_x(\mathbf{x}), \quad T_y(\mathbf{x} + \mathbf{a}) = e^{ik \cdot \mathbf{a}} T_y(\mathbf{x}), \quad (2.3.6)$$

where $T_x = \sigma_{xx} n_x + \sigma_{xy} n_y$ and $T_y = \sigma_{xy} n_x + \sigma_{yy} n_y$ are the traction components of the in-plane elastic wave, σ_{xx} , σ_{xy} and σ_{yy} are the stress components, and $\mathbf{n}(\mathbf{x}) = [n_x(\mathbf{x}), n_y(\mathbf{x})]^T$ is the unit normal vector. On the boundaries of the unit-cell, the Bloch periodic conditions (2.3.5) and (2.3.6) can be applied.

2.4 2D mixed elastic and acoustic wave propagation

2.4.1 Elastic wave equations and acoustic wave equation

The governing equation of elastic waves in solid are given the same as (2.3.1) and (2.3.2), which can be written as

$$\begin{aligned}(\lambda + 2\mu) \frac{\partial^2 u_x(\mathbf{x})}{\partial x^2} + \mu \frac{\partial^2 u_x(\mathbf{x})}{\partial y^2} + (\lambda + \mu) \frac{\partial^2 u_y(\mathbf{x})}{\partial x \partial y} &= -\rho_s \omega^2 u_x(\mathbf{x}), \\(\lambda + 2\mu) \frac{\partial^2 u_y(\mathbf{x})}{\partial y^2} + \mu \frac{\partial^2 u_y(\mathbf{x})}{\partial x^2} + (\lambda + \mu) \frac{\partial^2 u_x(\mathbf{x})}{\partial x \partial y} &= -\rho_s \omega^2 u_y(\mathbf{x}),\end{aligned}$$

where λ , ρ_s and μ are the Lamé's constant, mass density and shear modulus of the solid, u_x^j and u_y^j are the displacements in the x - and y -directions in the solid. The governing equation of water pressure waves in the ideal fluid field are expressed as

$$\frac{\partial^2 p}{\partial x^2} + \frac{\partial^2 p}{\partial y^2} = -\frac{\rho_f}{K} \omega^2 p, \quad (2.4.1)$$

where p , ρ_f and K are respectively the pressure, density and the bulk modulus of the fluid.

2.4.2 Interface continuity conditions

The continuity conditions on the interface Γ_0 of the fluid/solid or solid/fluid systems are the same. The acceleration in the normal direction perpendicular to the interface should be continuous, which can be expressed as

$$\frac{\partial p}{\partial \mathbf{n}} + \rho_f \ddot{\mathbf{u}} \mathbf{n} = 0, \quad (2.4.2)$$

where $\ddot{\mathbf{u}} = (\ddot{u}_x, \ddot{u}_y)^T = -\omega^2 (u_x, u_y)^T$ is the acceleration vector of the elastic solid on the interface. The equilibrium conditions of the tractions on the solid/fluid interface in the direction perpendicular to the interface can be expressed as

$$T_x = p n_x, \quad T_y = p n_y, \quad (2.4.3)$$

where the traction $T_x = \sigma_{xx}n_x + \sigma_{xy}n_y$ and $T_y = \sigma_{xy}n_x + \sigma_{yy}n_y$ are the traction components of the in-plane elastic wave in the solid.

2.4.3 Periodic boundary conditions

The periodic boundary conditions of the mixed elastic and acoustic waves for “fluid/solid” and “solid/fluid” systems are different, which are described separately in the following.

2.4.3.1 Fluid scatterers embedded in an elastic matrix

In the fluid/solid system, the periodic boundary conditions are applied to the elastic wave field in the solid matrix. According to the Bloch theorem, the elastic wave field in the phononic crystal is expressed as periodic functions. Hence the displacements and the tractions of the elastic waves can be written as

$$u_x(\mathbf{x} + \mathbf{a}) = e^{ik \cdot \mathbf{a}} u_x(\mathbf{x}), \quad u_y(\mathbf{x} + \mathbf{a}) = e^{ik \cdot \mathbf{a}} u_y(\mathbf{x}), \quad (2.4.4)$$

$$T_x(\mathbf{x} + \mathbf{a}) = e^{ik \cdot \mathbf{a}} T_x(\mathbf{x}), \quad T_y(\mathbf{x} + \mathbf{a}) = e^{ik \cdot \mathbf{a}} T_y(\mathbf{x}). \quad (2.4.5)$$

2.4.3.2 Elastic scatterers embedded in a fluid matrix

In the solid/fluid system, the periodic boundary conditions are only applied to the pressure wave field of fluid scatterers, which can be expressed as

$$p(\mathbf{x} + \mathbf{a}) = e^{ik \cdot \mathbf{a}} p(\mathbf{x}), \quad (2.4.6)$$

$$\frac{\partial p}{\partial \mathbf{n}}(\mathbf{x} + \mathbf{a}) = e^{ik \cdot \mathbf{a}} \frac{\partial p}{\partial \mathbf{n}}(\mathbf{x}), \quad (2.4.7)$$

Chapter 3

Radial basis function collocation methods (RBFCM)

The radial basis function collocation method (RBFCM) or the Kansa's Method is a well-known strong-form meshfree or meshless method. The key features of the RBFCM are the high-order accuracy, and the flexibility with respect to geometry. The RBFCM does not require a mesh or grid and only utilize the distance between distributed nodes in the computational domain. Thus, its extensions to higher dimensions do not increase the difficulty of the method. Due to its simplicity and effectiveness, the RBFCM is becoming more and more popular in different areas of engineering and sciences. In this chapter, the general idea of the RBFCM will be described and discussed for both the global and the local RBFCM. Three special numerical techniques for the spatial derivative calculations, which are required by the treatments of the boundary conditions, are presented.

3.1 Global radial basis function collocation method (GRBFCM)

In the RBFCM, the general solution $u(\mathbf{x})$ is assumed as

$$u(\mathbf{x}) = \sum_{n=1}^N \varphi(\|\mathbf{x} - \mathbf{x}_n\|) \alpha_n, \quad (3.1.1)$$

where N is the total number of all used nodes, φ is the RBF that we choose and α_n are the unknown coefficients that we need to compute, $\|\mathbf{x} - \mathbf{x}_n\|$ is the Euclidean distance between \mathbf{x} and \mathbf{x}_n . In Table 3.1, some frequently used RBFs are summarized, where ξ is the shape parameter and $r = \|\mathbf{x} - \mathbf{x}_n\|$. How to choose the optimal shape parameter is still a top issue in the scientific community. For simplicity, we take the following boundary value problem as an example

$$Lu(\mathbf{x}) = f(\mathbf{x}), \quad \mathbf{x} \in \Omega, \quad (3.1.2)$$

$$Bu(\mathbf{x}) = h(\mathbf{x}), \quad \mathbf{x} \in \Gamma_1, \quad (3.1.3)$$

$$u(\mathbf{x}) = g(\mathbf{x}), \quad \mathbf{x} \in \Gamma_2, \quad (3.1.4)$$

where Ω is the problem domain considered, Γ_1 is the Neumann boundary, Γ_2 is the Dirichlet boundary, L and B are the differential operators in Ω and on Γ_1 , respectively, and $f(\mathbf{x})$, $h(\mathbf{x})$ and $g(\mathbf{x})$ are the given functions. With the RBF approximation in (3.1.1), the boundary value problem defined by Eqs. (3.1.2) to (3.1.4) can be recast into the following discretized form:

$$\sum_{n=1}^N L\varphi(\|\mathbf{x} - \mathbf{x}_n\|)\alpha_n = f(\mathbf{x}), \quad \mathbf{x} \in \Omega, \quad (3.1.5)$$

$$\sum_{n=1}^N B\varphi(\|\mathbf{x} - \mathbf{x}_n\|)\alpha_n = h(\mathbf{x}), \quad \mathbf{x} \in \Gamma_1, \quad (3.1.6)$$

$$\sum_{n=1}^N \varphi(\|\mathbf{x} - \mathbf{x}_n\|)\alpha_n = g(\mathbf{x}), \quad \mathbf{x} \in \Gamma_2, \quad (3.1.7)$$

after the unknown coefficients have been evaluated from Eqs. (3.1.5) to (3.1.7), other information could be obtained by using (3.1.1).

Linear	r
Cubic	r^3
Polyharmonic	$r^{2n-1}, n \in N$
Polyharmonic	$r^{2n} \ln r, n \in N$
Thin-plate spline (TPS)	$r^2 \ln r$
Multiquadric (MQ)	$\varphi = \sqrt{r^2 + \xi^2}$
Inverse multiquadric (inverse MQ)	$\varphi = \frac{1}{\sqrt{r^2 + \xi^2}}$
Gaussian	$\varphi = \exp\left(-\frac{r^2}{\xi^2}\right)$

Table 3.1 Radial basis functions of various kinds [98].

3.2 Local radial basis function collocation method (LRBFCM)

In this section, a brief introduction of the local RBF method (LRBFCM) is given. Unlike the global RBF method as described in section 3.1, the LRBFCM approximates the field quantity with only a small number of local nodes in the neighbourhood of the considered node by using

$$u(\mathbf{x}) = \sum_{n=1}^{N_s} \varphi(\|\mathbf{x} - \mathbf{x}_n\|) \alpha_n, \quad (3.2.1)$$

where N_s is the total number of the involved local nodes, n denotes the n th local node, φ is the RBF, and α_n are the unknown coefficients related to the field quantities $u(\mathbf{x}_n)$, which can be expressed as follows

$$\alpha_n = \boldsymbol{\varphi}^{-1} \bar{\mathbf{u}}. \quad (3.2.2)$$

In Eq. (3.2.2), $\bar{\mathbf{u}} = [u(\mathbf{x}_1), \dots, u(\mathbf{x}_{N_s})]^T$ is the vector of the field quantities with the size of N_s , $\alpha_n = [\alpha_1, \alpha_2, \dots, \alpha_{N_s}]^T$ is the vector of the unknown coefficients with the size of N_s , and $\boldsymbol{\varphi} = [\varphi(\|\mathbf{x}_m - \mathbf{x}_n\|)]_{1 \leq m, n \leq N_s}$ is the RBF interpolation matrix with the size of $N_s \times N_s$. According to Eq. (3.2.2), Eq. (3.2.1) can be expressed as

$$u(\mathbf{x}) = \sum_{n=1}^{N_s} \varphi(\|\mathbf{x} - \mathbf{x}_n\|) \alpha_n = \boldsymbol{\Theta} \boldsymbol{\varphi}^{-1} \bar{\mathbf{u}}, \quad (3.2.3)$$

where

$$\boldsymbol{\Theta} = [\varphi(\|\mathbf{x} - \mathbf{x}_1\|), \dots, \varphi(\|\mathbf{x} - \mathbf{x}_{N_s}\|)]. \quad (3.2.4)$$

In Eq. (3.2.3), $\boldsymbol{\Theta} \boldsymbol{\varphi}^{-1}$ is a vector with the size of N_s related to the local field quantities. For convenience, the following definition is introduced

$$\bar{\boldsymbol{\varphi}}(\mathbf{x}) = \boldsymbol{\Theta}(\mathbf{x}) \boldsymbol{\varphi}^{-1}, \quad (3.2.5)$$

then the field quantity given in Eq. (3.2.3) can be expressed as follows

$$u(\mathbf{x}) = \bar{\boldsymbol{\varphi}}(\mathbf{x}) \bar{\mathbf{u}}. \quad (3.2.6)$$

It is straightforward to reformulate the vector $\bar{\boldsymbol{\varphi}}(\mathbf{x})$ to a global vector by inserting zeros at the proper positions. For simplicity, we define the global vector $\tilde{\boldsymbol{\varphi}}(\mathbf{x})$ with the size of N mapped from the local one with the size of N_s , where N is the total number of the global nodes, and $\tilde{\mathbf{u}}$ is the global field vector. Then we can obtain

$$\begin{aligned} \text{local } \bar{\boldsymbol{\varphi}}(\mathbf{x}) &\Rightarrow \text{global } \tilde{\boldsymbol{\varphi}}(\mathbf{x}), \\ \text{local } \bar{\mathbf{u}} &\Rightarrow \text{global } \tilde{\mathbf{u}}, \end{aligned} \quad (3.2.7)$$

where $\tilde{\mathbf{u}} = [u(\mathbf{x}_1), u(\mathbf{x}_2), \dots, u(\mathbf{x}_N)]^T$ is the vector of the field quantity in the global domain with the size of N . The global vector $\tilde{\boldsymbol{\varphi}}(\mathbf{x}) = [\tilde{\varphi}_1(\mathbf{x}), \tilde{\varphi}_2(\mathbf{x}), \dots, \tilde{\varphi}_N(\mathbf{x})]$ with the size of N is a sparse vector related to the local vector. When \mathbf{x} is not located on the local nodes, then $\tilde{\boldsymbol{\varphi}}(\mathbf{x}) = \mathbf{0}$. By using the relationship of (3.2.7), the Eq. (3.2.6) can be expressed as

$$u(\mathbf{x}) = \bar{\boldsymbol{\varphi}}(\mathbf{x})\bar{\mathbf{u}} = \tilde{\boldsymbol{\varphi}}(\mathbf{x})\tilde{\mathbf{u}}, \quad (3.2.8)$$

where the unknown vector $\tilde{\mathbf{u}}$ in Eq. (3.2.8) can be determined by using the governing partial differential equation and the boundary conditions. It should be noted here that the partial derivative of $\tilde{\boldsymbol{\varphi}}(\mathbf{x})$ is related to the partial differentiation of $\Theta(\mathbf{x})$, while $\boldsymbol{\varphi}^{-1}$ is a constant matrix, i.e.,

$$\text{global } \frac{\partial \tilde{\boldsymbol{\varphi}}(\mathbf{x})}{\partial x_i} \Rightarrow \text{local } \frac{\partial \bar{\boldsymbol{\varphi}}(\mathbf{x})}{\partial x_i} = \frac{\partial \Theta(\mathbf{x})}{\partial x_i} \boldsymbol{\varphi}^{-1}, \quad (3.2.9)$$

while otherwise the partial derivative of $\tilde{\boldsymbol{\varphi}}(\mathbf{x})$ is a Dirac-delta function which results in

$$u(\mathbf{x}) = \tilde{\boldsymbol{\varphi}}(\mathbf{x})\tilde{\mathbf{u}} = \delta_{\mathbf{x}\mathbf{x}_n} \tilde{u}_{x_n} = \begin{cases} \tilde{u}_{x_n}, & \mathbf{x} = \mathbf{x}_n, \\ 0, & \mathbf{x} \neq \mathbf{x}_n, \end{cases} \quad (3.2.10)$$

where the subscript n denotes the n th element of a vector, i.e., the corresponding field quantity at the n th node $\mathbf{x} = \mathbf{x}_n$. By substituting Eq. (3.2.8) back to Eqs. (3.1.2)-(3.1.4) we obtain

$$Lu(\mathbf{x}) = L\tilde{\boldsymbol{\varphi}}\tilde{\mathbf{u}} = f(\mathbf{x}), \quad (3.2.11)$$

$$Bu(\mathbf{x}) = B\tilde{\boldsymbol{\varphi}}\tilde{\mathbf{u}} = h(\mathbf{x}), \quad (3.2.12)$$

$$u(\mathbf{x}) = \tilde{\boldsymbol{\varphi}}\tilde{\mathbf{u}} = g(\mathbf{x}). \quad (3.2.13)$$

By using Eqs. (3.2.11)-(3.2.13), the LRBFCM calculates the unknown field quantity vector $\tilde{\mathbf{u}}$ instead of the unknown coefficient vector $\boldsymbol{\alpha}$.

3.3 Treatments of the boundary and interface continuity conditions

One critical issue of the strong-form LRBFCM is its stability, which is closely related to the numerical approximation of the boundary conditions, especially in the analysis of dynamic problems. In this section, we give some detailed discussions on the numerical treatments of the Dirichlet and Neumann boundary conditions separately. In particular, we present our new special techniques for the treatments of the Neumann boundary conditions. We will show that the new special techniques proposed in this thesis can greatly improve the stability of the RBFCM.

3.3.1 Dirichlet boundary conditions

In the case of the Dirichlet boundary conditions, the quantity u is known on the Dirichlet boundary. Then the governing Eq. (3.1.2) can be expressed as follows

$$Lu(\mathbf{x}) = L\tilde{\boldsymbol{\varphi}}\tilde{\mathbf{u}} = L\tilde{\boldsymbol{\varphi}}_{\Omega \cup \Gamma_1} \cdot \tilde{\mathbf{u}}_{\Omega \cup \Gamma_1} + L\tilde{\boldsymbol{\varphi}}_{\Gamma_2} \cdot \tilde{\mathbf{u}}_{\Gamma_2} = f(\mathbf{x}), \quad (3.3.1)$$

where $\tilde{\mathbf{u}}_{\Gamma_2}$ and $\tilde{\mathbf{u}}_{\Omega \cup \Gamma_1}$ are the vectors on Γ_2 and in $\Omega \cup \Gamma_1$, $L\tilde{\boldsymbol{\varphi}} = [L\tilde{\boldsymbol{\varphi}}_{\Omega \cup \Gamma_1}, L\tilde{\boldsymbol{\varphi}}_{\Gamma_2}]$, and $\tilde{\mathbf{u}} = [\tilde{\mathbf{u}}_{\Omega \cup \Gamma_1}, \tilde{\mathbf{u}}_{\Gamma_2}]^T$. Since $\tilde{\mathbf{u}}_{\Gamma_2}$ is already given, $L\tilde{\boldsymbol{\varphi}}_{\Gamma_2} \cdot \tilde{\mathbf{u}}_{\Gamma_2}$ can be evaluated analytically and moved to the right-hand side. Then Eq. (3.3.1) is converted to

$$L\tilde{\boldsymbol{\varphi}}_{\Omega \cup \Gamma_1} \cdot \tilde{\mathbf{u}}_{\Omega \cup \Gamma_1} = f(\mathbf{x}) - f^b(\mathbf{x}), \quad \mathbf{x} \in \Omega, \quad (3.3.2)$$

where $f^b(\mathbf{x}) = L\tilde{\boldsymbol{\varphi}}_{\Gamma_2} \cdot \tilde{\mathbf{u}}_{\Gamma_2}$. From Eq. (3.3.2), only the nodes in $\Omega \cup \Gamma_1$ are needed for the calculation of the unknown quantities, and in this manner a smaller matrix is formed. We should notice here that the Eq. (3.3.2) has already taken the Dirichlet boundary conditions into account exactly. By giving the same consideration to the Eq. (3.1.3), the unknown field quantity $\tilde{\mathbf{u}}$ can be evaluated, where the Dirichlet boundary conditions are taken into account exactly.

3.3.2 Neumann boundary conditions

In the case of the Neumann boundary conditions, the situation is much more complicated, because it requires the computation of the normal derivatives $\partial u / \partial \mathbf{n}$ of the field quantity. For this purpose, we propose three special methods to compute the normal derivatives.

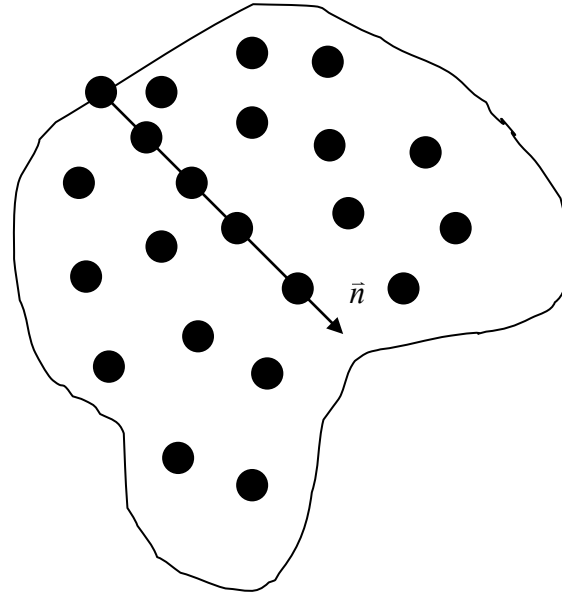


Fig. 3.1 Schematic sketch for the direct method.

Method 1: Direct method

As shown in Fig. 3.1, let us consider a boundary node whose normal derivative should be calculated. Instead of using the information of the nearby nodes, we use the information of some adjacent nodes only in the \mathbf{n} direction. Then $\partial u / \partial \mathbf{n}$ can be easily evaluated. Our own numerical experiences show that this method greatly increases the stability of the RBF-CM, because the calculation of the normal derivatives of the boundary nodes for 2D or 3D case is actually reduced to a 1D case in the \mathbf{n} direction. However, this method needs some interior nodes exactly in the \mathbf{n} direction, which limits the applicability of the method. To overcome this difficulty, we propose two other special methods in the following.

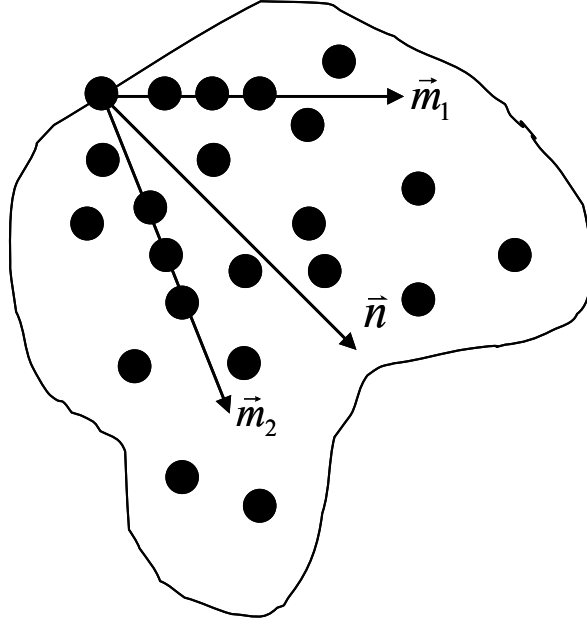


Fig. 3.2 Schematic sketch for the indirect method.

Method 2: Indirect method

Fig. 3.2 shows the schematic sketch for the indirect method. If we need to evaluate the normal derivative $\partial u / \partial \mathbf{n}$ without a sufficient number of available nodes in the \mathbf{n} direction, but with some nodes in other two directions \mathbf{m}_1 and \mathbf{m}_2 , then we can first compute the two directional derivatives $\partial u / \partial \mathbf{m}_1$ and $\partial u / \partial \mathbf{m}_2$. By using the following geometrical relationship, we obtain for the normal derivative $\partial u / \partial \mathbf{n}$ as

$$\frac{\partial u}{\partial \mathbf{m}_l} = \frac{\partial u}{\partial x} \cos(\mathbf{m}_l, x) + \frac{\partial u}{\partial y} \cos(\mathbf{m}_l, y), \quad l=1,2,$$

where (\mathbf{m}_l, x) and (\mathbf{m}_l, y) are the angles between the vector \mathbf{m}_l and the x -axis as well as the vector \mathbf{m}_l and the y -axis. Then the spatial derivatives $\partial u / \partial x$ and $\partial u / \partial y$ can be expressed by using $\partial u / \partial \mathbf{m}_l$ ($l=1,2$) as follows

$$\frac{\partial u}{\partial \mathbf{n}} = \frac{\partial u}{\partial x} \cos(\mathbf{n}, x) + \frac{\partial u}{\partial y} \cos(\mathbf{n}, y),$$

where (\mathbf{n}, x) and (\mathbf{n}, y) are the angles between the vector \mathbf{n} and the x -axis as well as the vector \mathbf{n} and the y -axis. This method can overcome the difficulty in finding

some sufficient nodes in the normal direction and is thus more flexible in the node distribution. However, as shown in Fig. 3.2, the indirect method still needs some nodes that are located on the two lines in the m_1 and m_2 directions. In order to solve this problem, we suggest a third method in the following.

Method 3: Fictitious nodes method

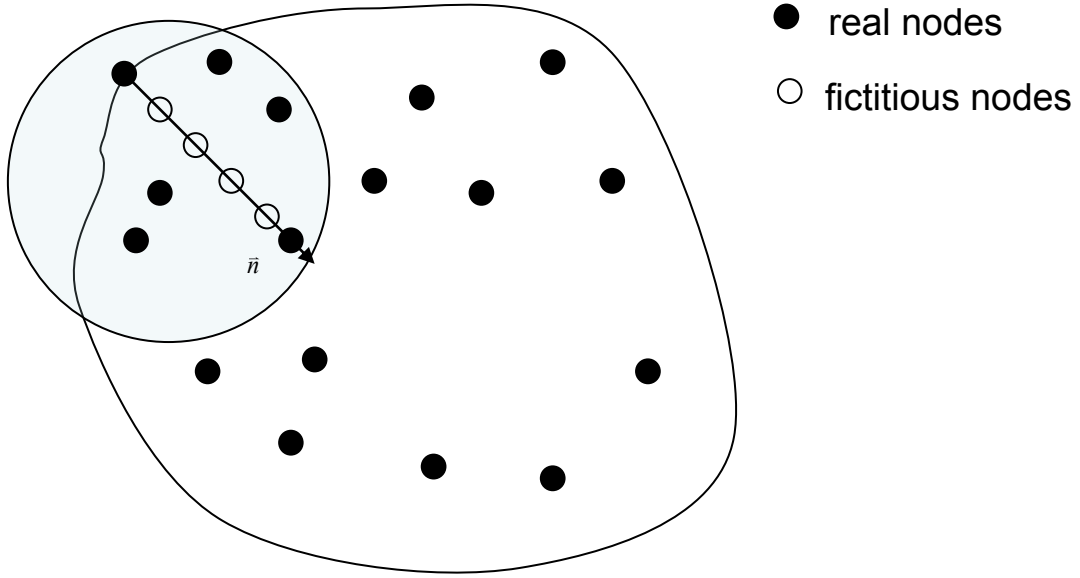


Fig. 3.3 Schematic sketch for the fictitious nodes method.

In the fictitious nodes method as illustrated in the Fig. 3.3, some fictitious nodes or ghost nodes are introduced in the normal direction, which are in reality not exist. Then the normal derivate $\partial u / \partial \mathbf{n}$ is calculated in two steps. First, the field quantity values on the fictitious nodes are expressed by using the information of the real nodes nearby as shown by the circular area in Fig. 3.3. Hence we have

$$u(\tilde{\mathbf{x}}) = \sum_n^{N_s} \varphi(\|\tilde{\mathbf{x}} - \mathbf{x}_n\|) \alpha_n = \tilde{\Theta} \boldsymbol{\varphi}^{-1} \tilde{\mathbf{u}}, \quad (3.3.3)$$

where $\tilde{\mathbf{u}} = [u(\mathbf{x}_1), \dots, u(\mathbf{x}_{N_s})]^T$ contains the values at the real nodes, $\tilde{\mathbf{x}}$ is located on the fictitious node that does not exist in the reality, $\boldsymbol{\varphi} = [\varphi(\|\mathbf{x}_m - \mathbf{x}_n\|)]_{1 \leq m, n \leq N_s}$, $\tilde{\Theta} = [\varphi(\|\tilde{\mathbf{x}} - \mathbf{x}_1\|), \dots, \varphi(\|\tilde{\mathbf{x}} - \mathbf{x}_{N_s}\|)]$, and α_n are the unknown coefficients that are

related to the real nodes. Then the second step is to calculate the normal derivative of the boundary nodes by using the direct method, which results in

$$\frac{\partial u(\mathbf{x})}{\partial \mathbf{n}} = \sum_n^{\tilde{N}_s} \frac{\partial \varphi(\|\mathbf{x} - \tilde{\mathbf{x}}_n\|)}{\partial \mathbf{n}} \tilde{\alpha}_n = \frac{\partial \Phi}{\partial \mathbf{n}} \Psi^{-1} \tilde{\mathbf{u}}, \quad (3.3.4)$$

where \tilde{N}_s is the local node number of the fictitious nodes that we introduced in the \mathbf{n} direction as shown in Fig. 3.3, $\tilde{\alpha}_n$ are the coefficients related to the fictitious nodes, and

$$\begin{aligned} \Psi &= [\varphi(\|\tilde{\mathbf{x}}_m - \tilde{\mathbf{x}}_n\|)]_{1 \leq m, n \leq \tilde{N}_s}, \\ \Phi &= [\varphi(\|\tilde{\mathbf{x}} - \tilde{\mathbf{x}}_1\|), \dots, \varphi(\|\tilde{\mathbf{x}} - \tilde{\mathbf{x}}_{\tilde{N}_s}\|)], \\ \tilde{\mathbf{u}} &= [u(\tilde{\mathbf{x}}_1), \dots, u(\tilde{\mathbf{x}}_{\tilde{N}_s})]^T. \end{aligned}$$

By substituting Eq. (3.3.3) into Eq. (3.3.4) we obtain

$$\frac{\partial u(\mathbf{x})}{\partial \mathbf{n}} = \frac{\partial \Phi}{\partial \mathbf{n}} \Psi \tilde{\Theta} \tilde{\mathbf{u}}. \quad (3.3.5)$$

In the fictitious nodes method, the requirement on the node distribution is much more flexible than the methods 1 and 2. However, the accuracy of the method could be a little lost due to the additional RBF interpolation by using the local nodes nearby, and also the distance of the fictitious nodes should be considered carefully.

3.3.3 Interface continuity conditions

In the multi-domain problems as considered in this thesis, the field quantities must be continuous on the interface. This can be analytically considered by adding or subtracting the corresponding columns in the formulated matrix. The traction or other continuous conditions can be well treated by using our proposed three numerical techniques for dealing with the derivative calculations.

3.4 Summary

The instability of the RBFCM stems from the numerical error of the boundary conditions, especially the Neumann boundary conditions. The three special techniques for the treatments of the Neumann boundary conditions proposed in this chapter are

very important to the stability of the RBFCM. The direct method possesses the highest stability but the lowest flexibility. The indirect method is more flexible in the node distribution but less stable than the direct method. The fictitious nodes method has the greatest flexibility in the node distribution but the lowest stability compared to the direct and indirect methods due to the introduction and intermediate approximation of the fictitious nodes. The essential advantages and disadvantages of the three special techniques are summarized in Table 3.2.

Techniques	Direct method	Indirect method	Fictitious nodes method
Distribution of nodes ● Real nodes. ○ Fictitious nodes			
Advantages	<ul style="list-style-type: none"> • Very accurate • Very stable 	<ul style="list-style-type: none"> • More flexible node distribution • Accurate and stable 	<ul style="list-style-type: none"> • Arbitrary node distribution • Very flexible
Disadvantages	<ul style="list-style-type: none"> • Strict node distribution required • Not flexible 	<ul style="list-style-type: none"> • Special node distribution • Less accurate and stable 	<ul style="list-style-type: none"> • Less accurate • Less stable

Table 3.2 Special techniques used for computing the normal derivatives of the primary field quantity.

From Table 3.2, it can be concluded that the indirect method or the direct method is more stable than the fictitious nodes method. How to generate a node distribution for which the direct method and the indirect method can be directly employed is an interesting topic. Here we propose a new way to apply the indirect method to calculate the spatial derivatives of the field quantity on a circular boundary.

Let us consider the node distribution as shown in Fig. 3. 4. For nodes located on the circular boundary in Fig. 3. 4, one can always find some interior nodes in the x - or y - direction. However, the indirect method can be employed only when sufficient nodes along another direction exist. Fortunately, the radius of the circular boundary is fixed, and the Cartesian coordinates can be transformed into the polar coordinates. Thus, the derivative in the tangential direction can be expressed as

$$\frac{\partial u}{\partial \mathbf{n}_t} = \frac{\partial u}{\partial \theta} r, \quad (3.3.12)$$

where \mathbf{n}_t is the tangential vector, r is the radius of the circular boundary, and θ is the polar angle of the considered node. The derivative $\partial u / \partial \theta$ is first evaluated in the circumferential direction, from which $\partial u / \partial \mathbf{n}_t$ can be subsequently evaluated by using Eq. (3.3.12). Thereafter, the indirect method can be employed for computing the normal derivatives of the field quantity on the boundary nodes.

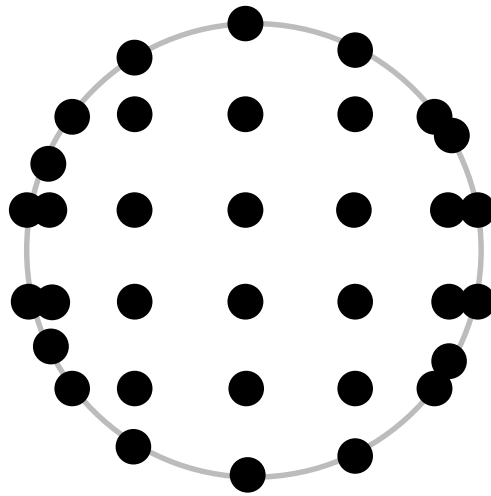


Fig. 3. 4 Special node distribution for a circular boundary.

Chapter 4

Global RBFCM for 1D solid/solid phononic crystals

In this chapter, the GRBFCM is employed to deal with the one-dimensional (1D) phononic crystals. The governing wave equation, the periodic boundary conditions of the unit-cell and the interface continuity conditions as presented in section 2.1 are discretized by the GRBFCM method. The stability of the RBFCM with different types of the RBFs is analyzed and compared in details. The basic discretized equations and the GRBFCM formulation of the eigenvalue problem for 1D phononic crystal are given in section 4.1. The influence of different RBFs on the stability of the RBFCM is discussed by investigating the numerical results in section 4.2. Then, some remarks are given in section 4.3.

4.1 GRBFCM formulation for 1D solid/solid phononic crystals

By applying the RBF formulation from Eqs. (3.1.5) to (3.1.7), we can obtain the general eigenvalue equation of the GRBFCM for the 1D phononic crystal structure as follows

$$\begin{bmatrix} \frac{d^2\varphi(\mathbf{x}_1)}{dx^2} & \mathbf{0} \\ \mathbf{0} & \frac{d^2\varphi(\mathbf{x}_2)}{dx^2} \\ \varphi(\mathbf{x}_{\Gamma_1}) & -\varphi(\mathbf{x}_{\Gamma_2})e^{-ika} \\ \frac{E_1}{E_2} \frac{d\varphi(\mathbf{x}_{\Gamma_1})}{dx} & \frac{d\varphi(\mathbf{x}_{\Gamma_2})}{dx} e^{-ika} \\ \varphi(\mathbf{x}_{\Gamma_0}) & -\varphi(\mathbf{x}_{\Gamma_0}) \\ \frac{E_1}{E_2} \frac{d\varphi(\mathbf{x}_{\Gamma_0})}{dx} & \frac{d\varphi(\mathbf{x}_{\Gamma_0})}{dx} \end{bmatrix} \begin{bmatrix} \alpha_1 \\ \alpha_2 \end{bmatrix} = -\omega^2 \begin{bmatrix} c_1^2\varphi(\mathbf{x}_1) & \mathbf{0} \\ \mathbf{0} & c_2^2\varphi(\mathbf{x}_2) \\ \mathbf{0} & \mathbf{0} \\ \mathbf{0} & \mathbf{0} \\ \mathbf{0} & \mathbf{0} \\ \mathbf{0} & \mathbf{0} \end{bmatrix} \begin{bmatrix} \alpha_1 \\ \alpha_2 \end{bmatrix}, \quad (4.1.1)$$

where $\mathbf{x}_1 \in D_1$, $\mathbf{x}_2 \in D_2$, $\mathbf{x}_{\Gamma_j} \in \Gamma_j$, $j=0, 1, 2$, N_1 and N_2 are the number of the nodes distributed in the domains D_1 and D_2 , respectively. The size of the matrix on both the left- and right-hand sides in Eq. (4.1.1) is the same. The generalised

eigenvalue equation (4.1.1) can be solved by MATLAB directly, and the bandgap structure can be obtained by sweeping the wave vector at the boundary in the first irreducible Brillouin zone.

4.2 Numerical results and discussions

In this section, we present some numerical tests of different RBFs by using an example of a 1D phononic crystal. The numerical results are compared with the exact solution in the work of [135]. The layer thicknesses are taken as $a_1 = a_2 = 0.5m$ as shown in Fig. 2.2. The used material parameters are given as follows:

Epoxy:

$$\rho_2 = 1180 \text{ kg/m}^3, \quad c_2 = 1161 \text{ m/s},$$

Aurum:

$$\rho_1 = 19500 \text{ kg/m}^3, \quad c_1 = 1239 \text{ m/s}.$$

The relative error used in this section is defined as follows

$$\text{Error} = \frac{\sum (E_{\text{exact}} - E_r)}{\sum E_{\text{exact}}},$$

where N is the total number of the used nodes, E_r and E_{exact} represent the numerical result and the exact solution respectively. We compare the numerical results from the first to the fourth band with the exact solution to reveal the effects of the type of the used RBFs, the shape parameter and the total node number or the nodal distance on the accuracy of the GRBFCM.

4.2.1 Numerical results of the inverse MQ RBF

Effects of the shape parameter

In this subsection, only the inverse MQ RBF is considered. The computed band structures for different values of the shape parameter are shown in Fig. 4.1 to Fig. 4.3, and Table 4.1 shows the relative errors of the lowest four bands of the corresponding figures.

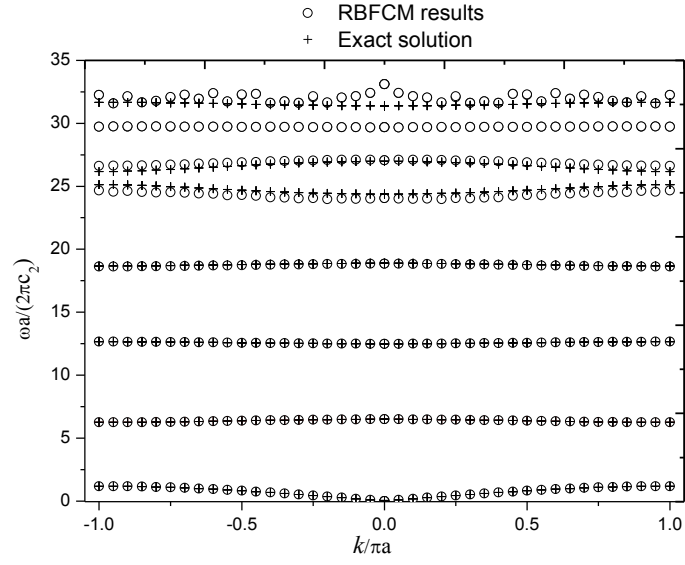


Fig. 4.1 Band structure obtained by using inverse MQ RBF with $N=19$ and $\xi = 0.8$.

$N=19$	$\xi = 0.8$	$\xi = 0.9$	$\xi = 1.5$
1 st	2.36×10^{-4}	1.16×10^{-4}	3.47×10^{-2}
2 nd	9.48×10^{-7}	7.92×10^{-7}	4.58×10^{-2}
3 rd	1.09×10^{-5}	5.94×10^{-5}	2.27×10^{-2}
4 th	2.71×10^{-3}	4.20×10^{-3}	1.48×10^{-2}

Table 4.1 Relative errors by using inverse MQ RBF with fixed $N=19$.

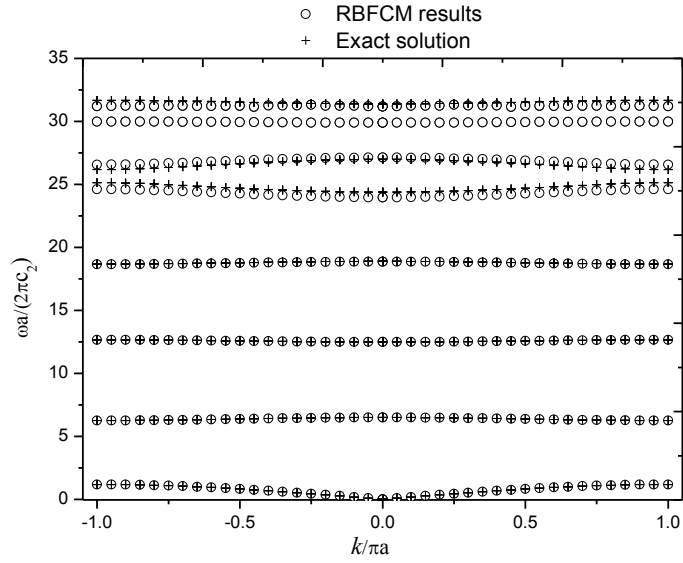


Fig. 4.2 Band structure obtained by using inverse MQ RBF with $N=19$ and $\xi = 0.9$.

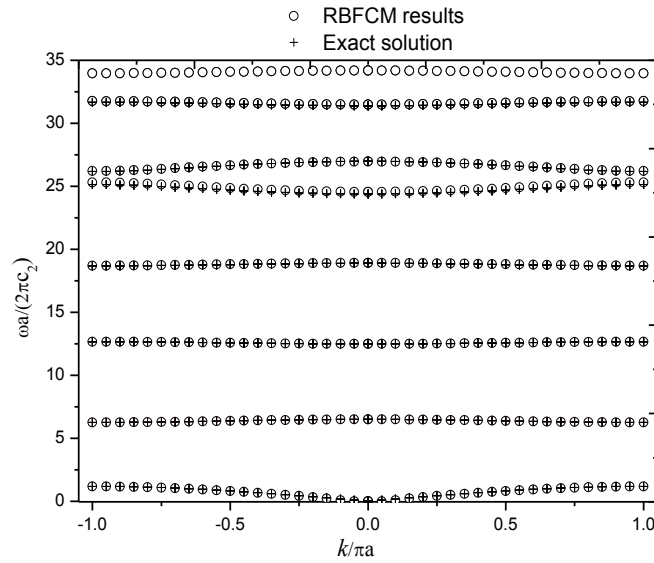


Fig. 4.3 Band structure obtained by using inverse MQ RBF with $N=19$ and $\xi = 1.5$.

Fig. 4.1 to Fig. 4.3 show that, as the shape parameter increases from $\xi = 0.8$ to $\xi = 1.5$, the band structures obtained by the inverse MQ are becoming more stable, but the relative error as given in Table 4.1 is getting worse. It is easy to conclude that with a fixed number of the used nodes, a larger shape parameter ξ leads to a more

stable but less accurate band structure. On the other hand, a smaller shape parameter ξ gives rise to a less stable but more accurate band structure. Our own experiences show that, when $N=19$, the shape parameter of the inverse MQ RBF in the range of $\xi = 0.9$ to $\xi = 1.5$ always works well in the present GRBFCM.

Effects of the total node number

In order to reveal the influences of the total node number or the nodal distance, the shape parameter is fixed now as $\xi=1$, while different total node numbers are employed to obtain the band structures in Fig. 4.4 to Fig. 4.6.

$\xi = 1$	$N=9$	$N=19$	$N=29$
1 st	2.05×10^{-1}	1.33×10^{-3}	4.08×10^{-2}
2 nd	2.33×10^{-3}	7.56×10^{-7}	2.93×10^{-2}
3 rd	6.88×10^{-2}	2.63×10^{-5}	6.75×10^{-7}
4 th	1.79×10^{-1}	1.35×10^{-4}	1.09×10^{-1}

Table 4.2 Relative errors by using inverse MQ RBF with fixed $\xi = 1$.

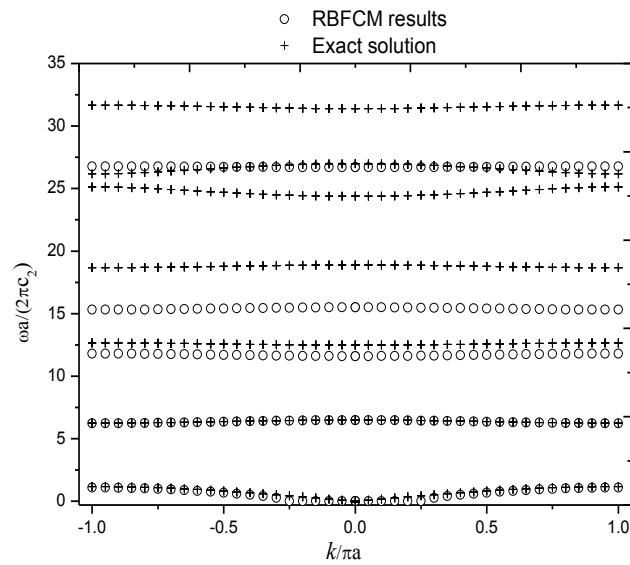


Fig. 4.4 Band structure obtained by using inverse MQ RBF with $N=9$ and $\xi = 1$.

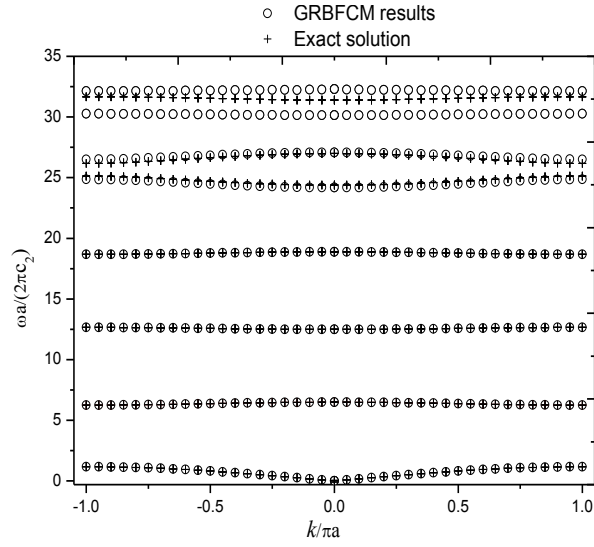


Fig. 4.5 Band structure obtained by using inverse MQ RBF with $N=19$ and $\xi = 1$.

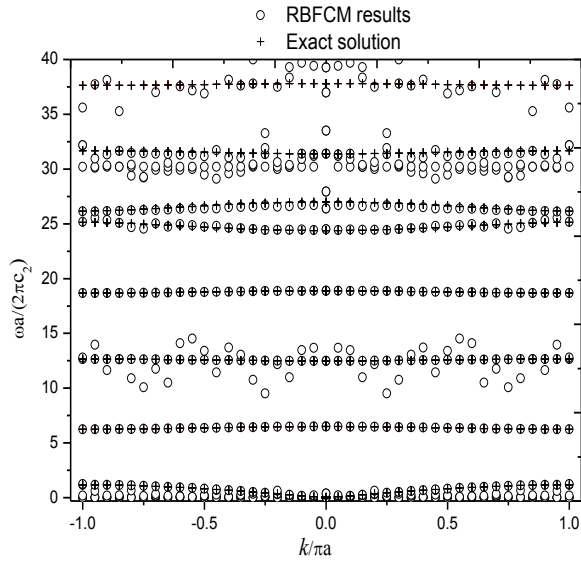


Fig. 4.6 Band structure obtained by using inverse MQ RBF with $N=29$ and $\xi = 1$.

Fig. 4.4 to Fig. 4.6 show the computed band structures obtained by using $N=9$, $N=19$ and $N=29$, while Table 4.2 shows the relative errors of the lowest four bands accordingly. From Fig. 4.4 to Fig. 4.6, we can see that, an increasing total node number may lead to an unstable band structure for a fixed shape parameter. However, if the shape parameter of the inverse MQ also increases with the total node number,

the results become much better as shown in Fig. 4.7.

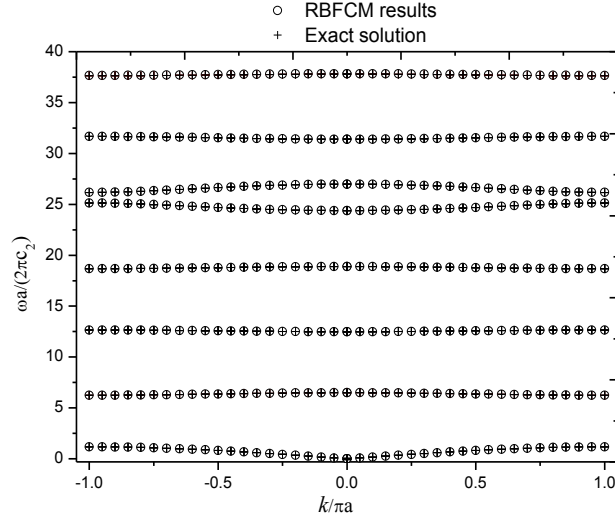


Fig. 4.7 Band structure obtained by using inverse MQ RBF with $N=29$ and $\xi = 2$.

4.2.2 Numerical results of the Gaussian RBF

Effects of the shape parameter

In this subsection, the Gaussian RBF is considered. The computed band structures for different values of the shape parameter are presented in Fig. 4.8 to Fig. 4.10, while Table 4.3 gives the relative errors of the lowest four bands of the corresponding figures.

$N=19$	$\xi = 0.2$	$\xi = 0.3$	$\xi = 0.4$	$\xi = 0.6$
1 st	1	2.26×10^{-1}	2.45×10^{-2}	5.95×10^{-4}
2 nd	9.57×10^{-4}	4.09×10^{-5}	4.06×10^{-6}	2.31×10^{-7}
3 rd	2.19×10^{-4}	4.06×10^{-6}	6.17×10^{-6}	4.25×10^{-7}
4 th	1.54×10^{-3}	6.04×10^{-4}	1.13×10^{-3}	5.56×10^{-3}

Table 4.3 Relative errors by using Gaussian RBF with fixed $N=19$.

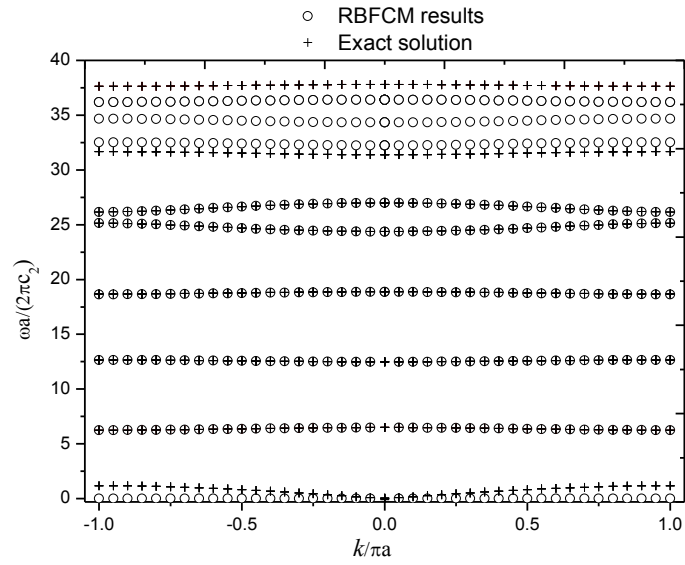


Fig. 4.8 Band structure obtained by using Gaussian RBF with $N=19$ and $\xi = 0.2$.

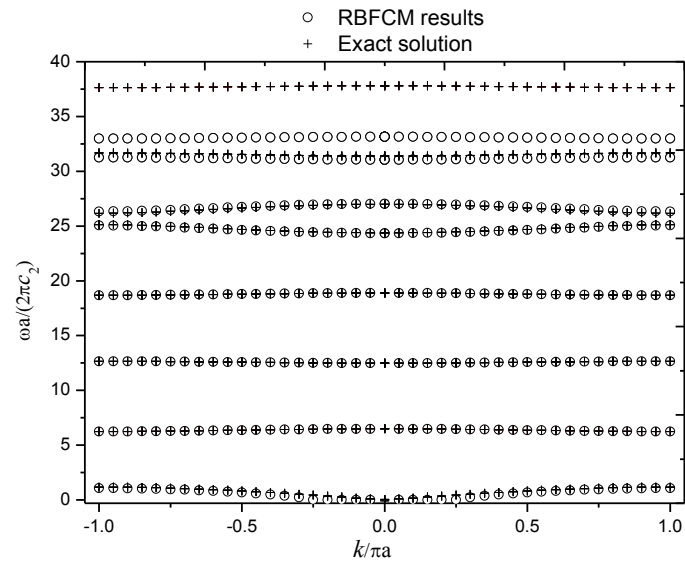


Fig. 4.9 Band structure obtained by using Gaussian RBF with $N=19$ and $\xi = 0.3$.

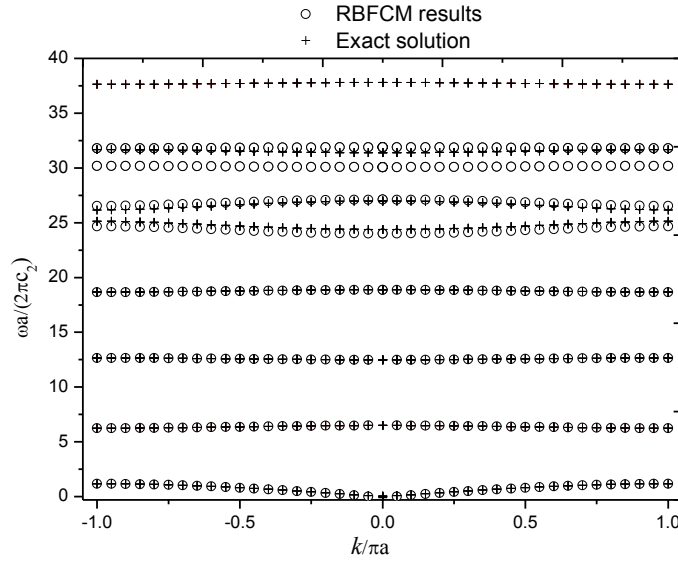


Fig. 4.10 Band structure obtained by using Gaussian RBF with $N=19$ and $\xi = 0.4$.

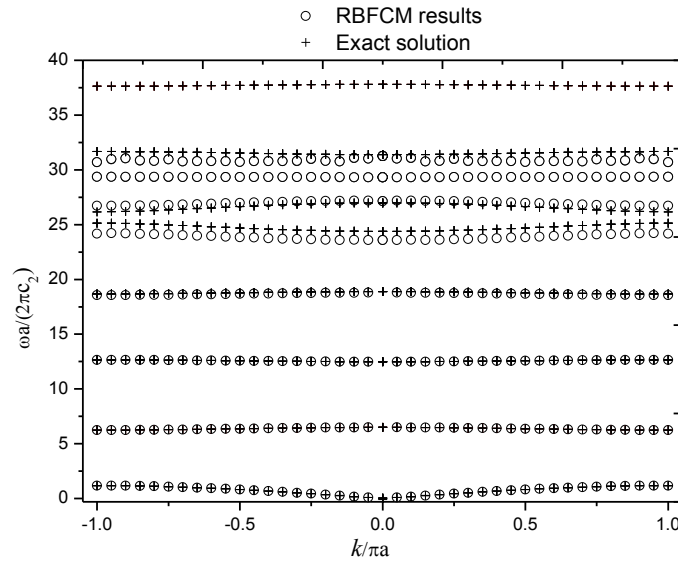


Fig. 4.11 Band structure obtained by using Gaussian RBF with $N=19$ and $\xi = 0.6$.

From Fig. 4.8 to Fig. 4.11, we can observe that with the shape parameter increasing from $\xi = 0.2$ to $\xi = 0.6$, the band structures obtained by the Gaussian RBF become less stable, but the relative error as given in Table 4.3 is getting better. Thus, it can be concluded that with a fixed number of the used nodes, a smaller shape parameter ξ leads to a more stable but less accurate band structure. In contrast, a

larger shape parameter ξ results in a less stable but more accurate band structure. According to our own experiences that for $N=19$ the shape parameter of the Gaussian RBF in the range of $\xi = 0.3$ to $\xi = 0.6$ always works well in the present GRBFCM. This conclusion is just opposite to the inverse MQ RBF.

Effects of the total node number

To investigate the influences of the total node number or the nodal distance, the shape parameter is fixed now as $\xi = 0.4$, while different total node numbers are employed to obtain the band structures given in Fig. 4.12 to Fig. 4.14.

$\xi = 0.4$	$N=9$	$N=19$
1 st	1	2.45×10^{-2}
2 nd	1.34×10^{-3}	4.06×10^{-6}
3 rd	4.19×10^{-2}	6.17×10^{-6}
4 th	1.46×10^{-1}	1.13×10^{-3}

Table 4.4 Relative errors by using Gaussian RBF with fixed $\xi = 0.4$.

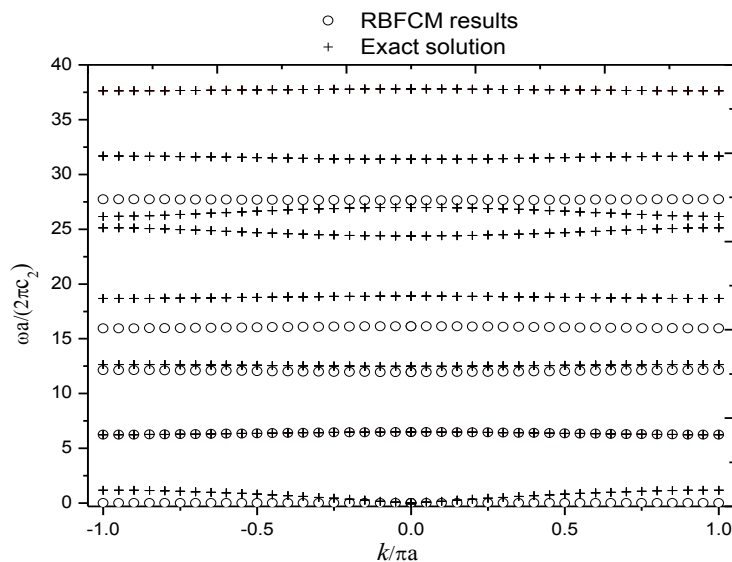


Fig. 4.12 Band structure obtained by using Gaussian RBF with $N=9$ and $\xi = 0.4$.

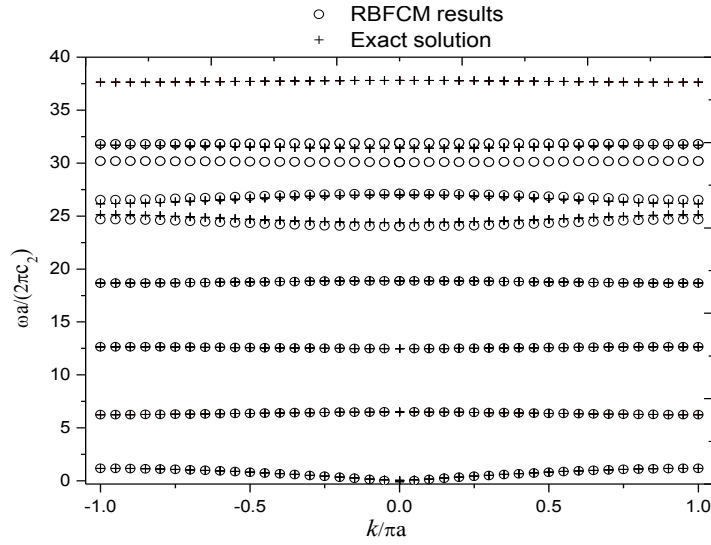


Fig. 4.13 Band structure obtained by using Gaussian RBF with $N=19$ and $\xi = 0.4$.

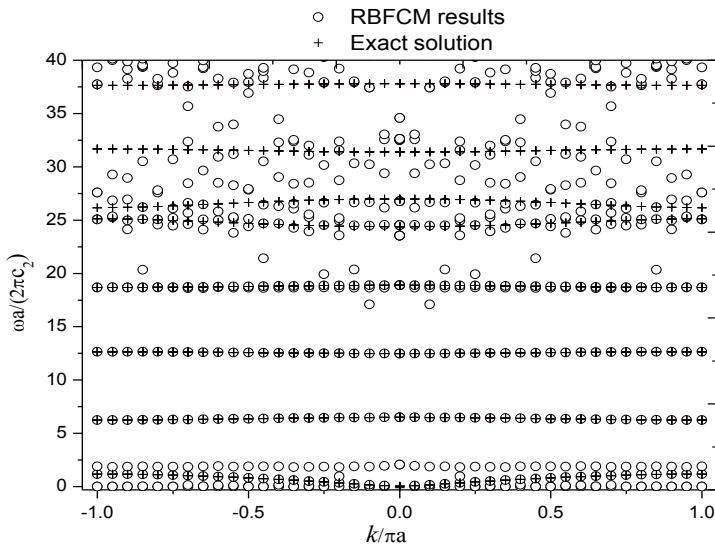


Fig. 4.14 Band structure obtained by using Gaussian RBF with $N=29$ and $\xi = 0.4$.

In Fig. 4.12 to Fig. 4.14, the computed band structures obtained by using $N=9$, $N=19$ and $N=29$ are presented, while the corresponding relative errors of the lowest four bands are given in Table 4.4. Fig. 4.12 to Fig. 4.14 illustrate that an increasing total node number may lead to an unstable band structure for a fixed shape parameter. However, if the shape parameter of the Gaussian RBF decreases with the total node number, the results will become improved as shown in Fig. 4.15. This is also opposite

to the inverse MQ RBF.

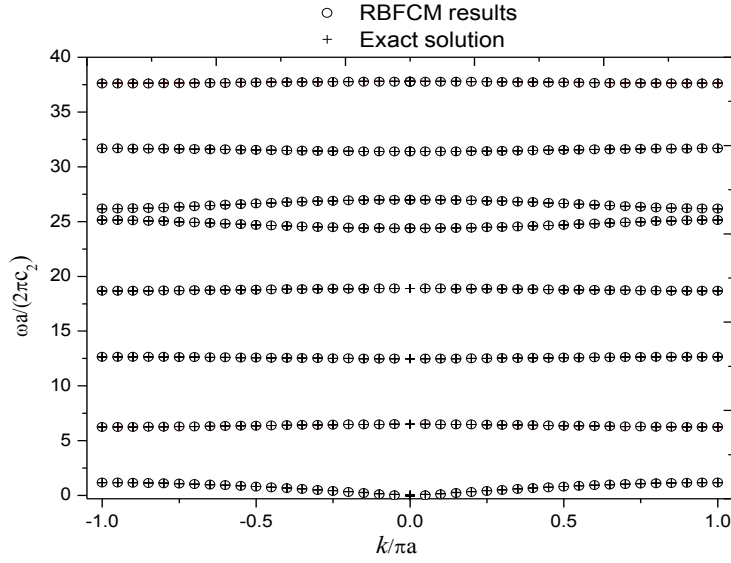


Fig. 4. 15 Band structure obtained by using Gaussian RBF with $N=29$ and $\xi = 0.2$.

By comparing the properties of the Gaussian RBF and the inverse MQ RBF, one can find that the absolute value of the Gaussian RBF $\varphi(\xi)$ monotonically increases with ξ while the absolute value of the inverse MQ RBF $\varphi(\xi)$ monotonically decreases with ξ . When the absolute value of $\varphi(\xi)$ in the GRBFCM monotonically increases with ξ , a larger shape parameter ξ leads to more accurate but less stable results, while a smaller shape parameter ξ in a certain range gives rise to a less accurate but more stable band structure. If the absolute value of $\varphi(\xi)$ in the GRBFCM monotonically decreases with ξ , the situation is just opposite. This conclusion is almost the same as that of our previous work [136]. In order to verify this conclusion, the MQ RBF is tested in the next subsection.

4.2.3 Numerical results of the MQ RBF

Effects of the shape parameter

In this subsection, the MQ RBF is investigated. Figures 4.16 to 4.19 show the computed band structures for different values of the shape parameter, while the corresponding relative errors of the lowest four bands are given in Table 4.5.

$N=19$	$\xi = 0.4$	$\xi = 0.5$	$\xi = 1$	$\xi = 1.2$
1 st	2.56×10^{-1}	8.24×10^{-2}	1.31×10^{-3}	4.51×10^{-4}
2 nd	2.30×10^{-5}	4.49×10^{-5}	1.23×10^{-6}	1.22×10^{-6}
3 rd	7.39×10^{-4}	1.90×10^{-4}	1.42×10^{-5}	1.34×10^{-5}
4 th	2.35×10^{-3}	5.59×10^{-4}	1.11×10^{-3}	3.43×10^{-3}

Table 4.5 Relative errors by using MQ RBF with fixed $N=19$.

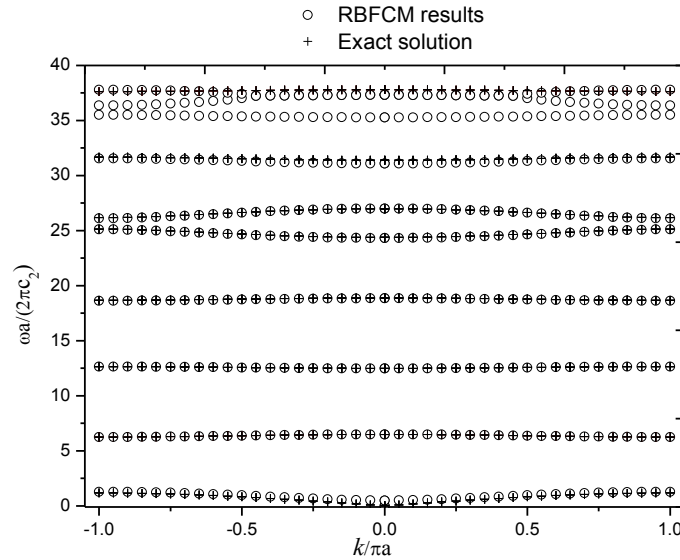


Fig. 4.16 Band structure obtained by using MQ RBF with $N=19$ and $\xi = 0.4$.

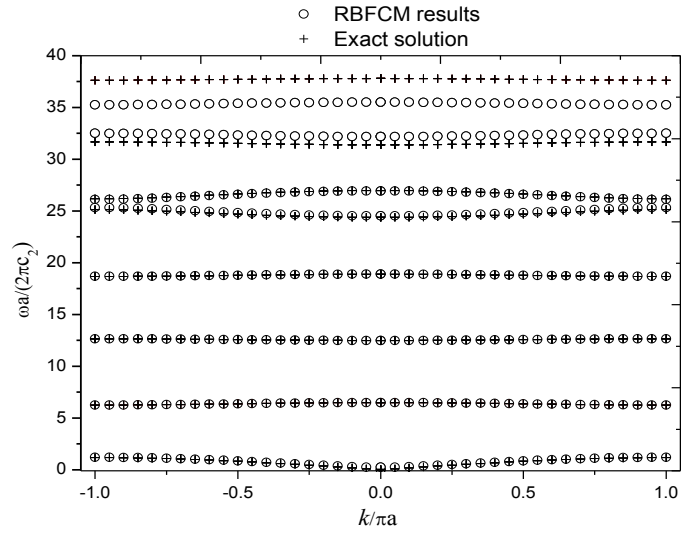


Fig. 4.17 Band structure obtained by using MQ RBF with $N=19$ and $\xi = 0.5$.

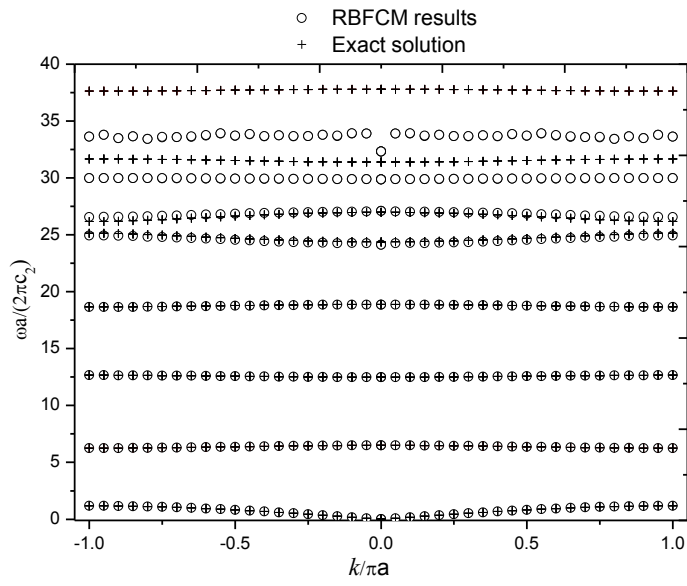


Fig. 4.18 Band structure obtained by using MQ RBF with $N=19$ and $\xi = 1$.

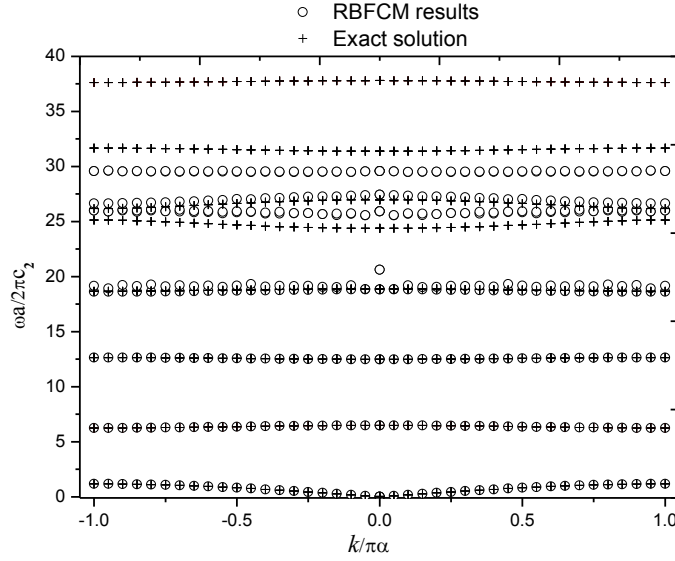


Fig. 4.19 Band structure obtained by using MQ RBF with $N=19$ and $\xi = 1.2$.

In contrast to the inverse MQ RBF but similar to the Gaussian RBF, the absolute value of the MQ RBF $\varphi(\xi)$ monotonically increases with the shape parameter ξ . From Fig. 4.16 to Fig. 4.19 one can find that, as the shape parameter increases from $\xi = 0.4$ to $\xi = 1.2$, the band structures obtained by the MQ RBF are becoming less stable, but the relative error as given in Table 4.5 is getting better. Also here, it can be concluded that for a fixed total node number, a smaller shape parameter ξ leads to a more stable but less accurate band structure. On the contrary, a larger shape parameter ξ yields a less stable but more accurate band structure. Our own numerical experiences show that for $N=19$ the shape parameter of the MQ RBF in the range of $\xi = 0.4$ to $\xi = 1.2$ always works well in the present GRBFCM.

Effects of the total node number

In order to analyse the influences of the total node number or nodal distance, the shape parameter is fixed now as $\xi = 0.7$, while different total node numbers are used to compute the band structures in Fig. 4.20 to Fig. 4.22.

$\xi = 0.7$	$N=9$	$N=19$	$N=29$
1 st	4.32×10^{-1}	1.12×10^{-2}	7.09×10^{-4}
2 nd	3.92×10^{-3}	1.00×10^{-5}	1.09×10^{-7}
3 rd	6.41×10^{-2}	8.20×10^{-5}	2.40×10^{-6}
4 th	1.65×10^{-1}	1.92×10^{-3}	1.29×10^{-1}

Table 4.6 Relative errors by using MQ RBF with fixed $\xi = 0.7$.

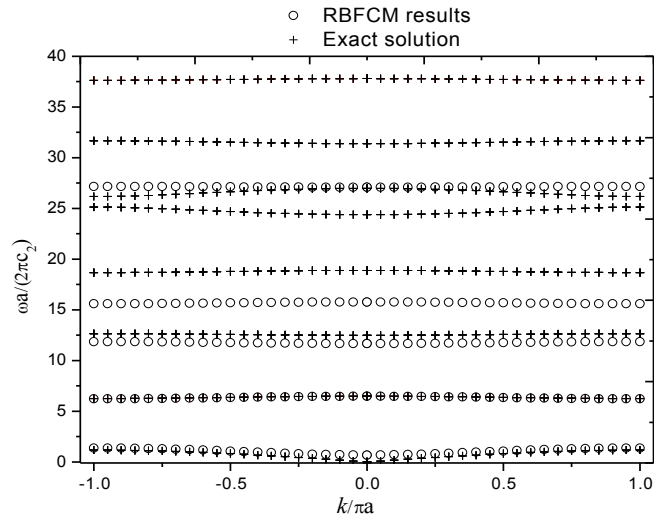


Fig. 4.20 Band structure obtained by using MQ RBF with $N=9$ and $\xi = 0.7$.

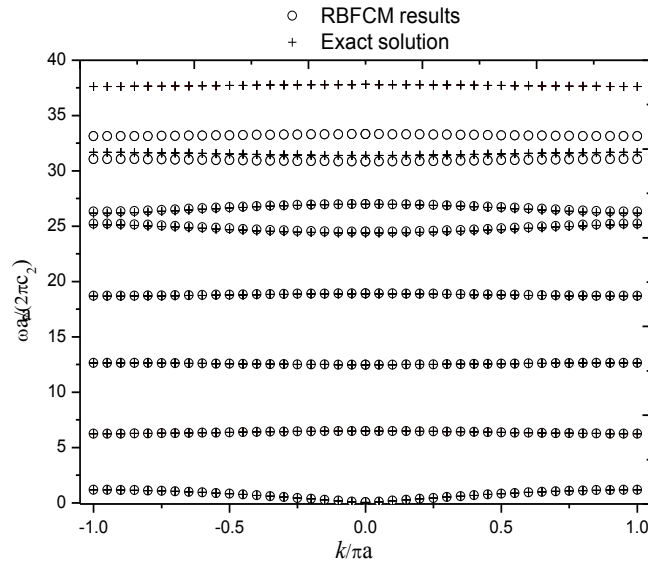


Fig. 4.21 Band structure obtained by using MQ RBF with $N=19$ and $\xi = 0.7$.

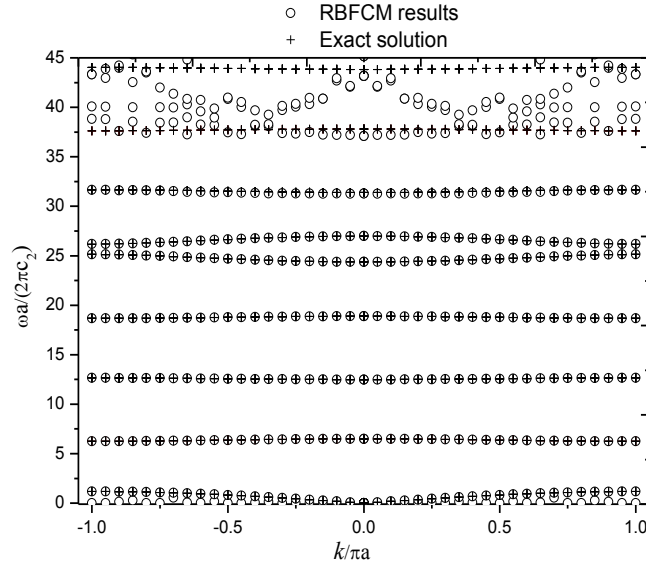


Fig. 4.22 Band structure obtained by using MQ RBF with $N=29$ and $\xi = 0.7$.

Fig. 4.20 to Fig. 4.22 show the computed band structures obtained by using $N=9$, $N=19$ and $N=29$, while Table 4.6 shows the relative errors of the lowest four bands accordingly. From Fig. 4.20 to Fig. 4.22, we can see that, an increasing total node number may lead to an unstable band structure for a fixed shape parameter. However, if the shape parameter of the MQ decreases with the total node number, the results become much better as shown in Fig. 4.23.

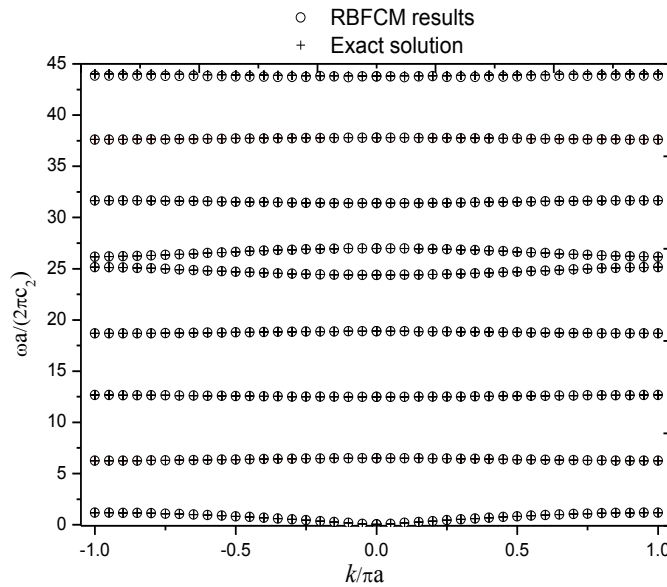


Fig. 4.23 Band structure obtained by using MQ RBF with $N=29$ and $\xi = 0.5$.

4.3 Summary

The numerical results presented in the previous sections show the effects of the shape parameter and the total node number or the nodal distance on the numerical accuracy of the RBFCM for band structure calculations of 1D phononic crystals. One can find that the shape parameter should also be changed accordingly when more nodes are employed because of the decreasing nodal distance. How to change the shape parameter depends on the property of the used RBF. When the absolute value of the RBF $\varphi(\xi)$ monotonically increases with ξ , then with a smaller shape parameter ξ we can obtain more stable band structures. If the absolute value of the RBF $\varphi(\xi)$ monotonically decreases with ξ , then a larger shape parameter ξ is suggested to obtain more stable band structures. The effects of the shape parameter and the total node number are summarized in Table 4.7

RBF $\varphi(\xi)$		
RBF property	$ \varphi(\xi) $ monotonically decreases with ξ	$ \varphi(\xi) $ monotonically increases with ξ
ξ increases	More stable	Less stable
	Less accurate	More accurate
ξ decreases	Less stable	More stable
	More accurate	Less accurate
N increases	ξ should increase	ξ should decrease

Table 4.7: The effects of the shape parameter and total node number.

The relationship between the shape parameter and the total node number or the nodal distance investigated in this chapter is very important for the accurate and efficient computation of the band structures of phononic crystals. From our numerical

tests for 1D phononic crystals, we find that, when $N=19$ is employed, the range of the shape parameter in the MQ RBF is $\xi = 0.4$ to $\xi = 1.2$, which is larger than the ranges of the shape parameter in the Gaussian RBF ($\xi = 0.3$ to $\xi = 0.6$) and the inverse MQ RBF ($\xi = 0.9$ to $\xi = 1.5$). The computed band structures also show that the MQ RBF in the present RBFCM outperforms the Gaussian RBF and the inverse MQ RBF. For this reason, only the MQ RBF is employed in the following chapters for the band structure computations of 2D phononic crystals.

Chapter 5

Local RBFCM for anti-plane wave propagation analysis in 2D solid/solid phononic crystals

In Chapter 4, the global RBFCM has already been applied to the 1D solid/solid phononic crystals, and the influences of the shape parameter and the total anode number have been discussed in details. Due to the high computational costs of the global RBFCM, it is very difficult to apply the global RBFCM to high-dimensional problems. In this chapter, the LRBFCM is developed and applied to calculate the band structures of two-dimensional (2D) anti-plane transverse elastic waves in phononic crystals. The special numerical techniques proposed in Chapter 2 are applied to compute the spatial derivatives of the field quantities, which are needed by the boundary conditions and the interface continuity conditions.

The governing wave equation, the periodic boundary conditions of the unit-cell and the continuity conditions on the interface between the matrix and the scatterer are discretized by the LRBFCM, which forms a matrix eigenvalue equation. The band structures or the dispersion relations can be obtained by solving the generalized eigenvalue problem and sweeping the boundary of the irreducible first Brillouin zone. The developed LRBFCM is verified by using the corresponding results obtained with the FEM. Numerical examples for various scatterer shapes and lattice forms with different acoustic impedance ratios are presented and discussed in this chapter. The FEM results are also used to show the performance and the efficiency of the developed LRBFCM for the anti-plane transverse elastic wave propagation in 2D phononic crystals.

This chapter is organized as follows. The general form of the LRBFCM for anti-plane transverse elastic wave propagation in 2D phononic crystals is given in section 5.1. Numerical results are discussed and compared with the FEM results in section 5.2. The computational efficiency is analysed and discussed in section 5.3. Then some concluding remarks are given in the last section 5.4.

5.1 LRBFCM formulation of the eigenvalue problems

There are two ways to calculate the band structures or dispersion relations of phononic crystals. One way is to employ the Bloch periodic condition (2.2.5) in the whole domain, and then substitute Eq. (2.2.5) into the governing equation to formulate an eigenvalue problem with the wave vector \mathbf{k} . Then the eigenvalues ω are calculated for different \mathbf{k} , and those eigenvalues in the first Brillouin zone are picked out according to some relationships, for more details please refer to [137]. The other way is to employ the periodic conditions only on the boundary of the unit-cell. Then the governing equation and the continuity conditions on the interface are still needed for computing the eigenvalues ω . The band structure or dispersion relation can be directly calculated by sweeping the wave vector \mathbf{k} in the first Brillouin zone. In this thesis, we use the latter one. In this section, the LRBFCM formulation of the governing equations, continuity boundary conditions and the periodic boundary conditions of the anti-plane transverse wave in two dimensional phononic crystals are respectively presented.

5.1.1 Discretized governing equations

By using Eqs. (3.2.11) to (3.2.13), we can write governing equation of anti-plane transverse wave (2.2.1) as

$$\mu_j \Delta \tilde{\varphi}(\mathbf{x}^j) \tilde{\mathbf{u}}^j = \rho_j \omega^2 \Delta \tilde{\varphi}(\mathbf{x}^j) \tilde{\mathbf{u}}^j, \quad (j=0,1), \quad (5.2.1)$$

5.1.2 Discretized interface continuity conditions

The interface continuity conditions of the anti-plane transverse wave equations in (2.2.3) can be expressed as

$$\mu_0 \frac{\partial \tilde{\varphi}(\mathbf{x}_{\Gamma_0}^0)}{\partial \mathbf{n}} \tilde{\mathbf{u}}^0 = \mu_1 \frac{\partial \tilde{\varphi}(\mathbf{x}_{\Gamma_0}^1)}{\partial \mathbf{n}} \tilde{\mathbf{u}}^1,$$

and (2.2.2) considered analytically by rearranging the columns of the RBF matrix,

which will be discussed later.

5.1.3 Discretized periodic boundary conditions of square lattice

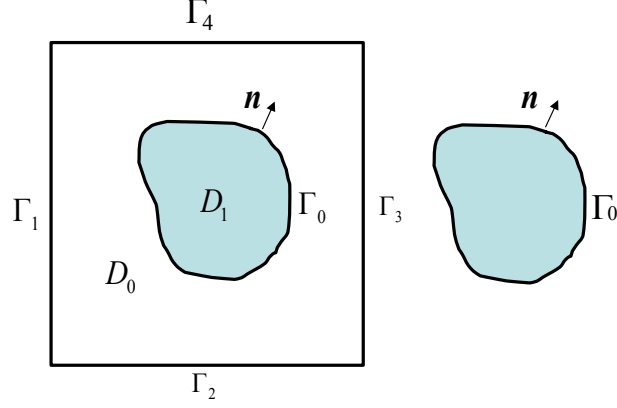


Fig. 5.1 Matrix and scatterer in a unit-cell of a square lattice.

For the square lattice, as shown in Fig. 5.1, we have

$$u(\mathbf{x}_{\Gamma_1}) = u(\mathbf{x}_{\Gamma_3})e^{-ik_x a}, \quad u(\mathbf{x}_{\Gamma_2}) = u(\mathbf{x}_{\Gamma_4})e^{-ik_y a}, \quad (5.2.2)$$

$$T(\mathbf{x}_{\Gamma_1}) = T(\mathbf{x}_{\Gamma_3})e^{-ik_x a}, \quad T(\mathbf{x}_{\Gamma_2}) = T(\mathbf{x}_{\Gamma_4})e^{-ik_y a}, \quad (5.2.3)$$

where $\mathbf{x}_{\Gamma_1} \in \Gamma_1$, $\mathbf{x}_{\Gamma_2} \in \Gamma_2$, $\mathbf{x}_{\Gamma_3} \in \Gamma_3$, $\mathbf{x}_{\Gamma_4} \in \Gamma_4$. $T = \frac{\partial u}{\partial \mathbf{n}}$ is the traction at the interface.

Equations (5.2.3) can be recast into the following matrix form

$$\begin{bmatrix} \Delta u(\mathbf{x}^0) & 0 \\ 0 & \Delta u(\mathbf{x}^1) \\ \frac{\partial u(\mathbf{x}_{\Gamma_1})}{\partial \mathbf{n}} - \frac{\partial u(\mathbf{x}_{\Gamma_3})}{\partial \mathbf{n}} e^{-ik_x a} & 0 \\ \frac{\partial u(\mathbf{x}_{\Gamma_2})}{\partial \mathbf{n}} - \frac{\partial u(\mathbf{x}_{\Gamma_4})}{\partial \mathbf{n}} e^{-ik_y a} & 0 \\ \frac{\partial u(\mathbf{x}_{\Gamma_0}^0)}{\partial \mathbf{n}} & -\frac{\mu_1}{\mu_0} \frac{\partial u(\mathbf{x}_{\Gamma_0}^1)}{\partial \mathbf{n}} \end{bmatrix} = -\omega^2 \begin{bmatrix} \frac{\rho_0}{\mu_0} u(\mathbf{x}^0) & 0 \\ 0 & \frac{\rho_1}{\mu_1} u(\mathbf{x}^1) \\ 0 & 0 \end{bmatrix}, \quad (5.2.4)$$

where $\mathbf{x}^0 \in D_0$, $\mathbf{x}^1 \in D_1$. Eq. (5.2.4) can be rewritten in the following form

$$\mathbf{A}\mathbf{U} = -\omega^2 \mathbf{H}\mathbf{U}, \quad (5.2.5)$$

where \mathbf{A} is the RBF matrix obtained by using the RBFs and \mathbf{H} is the matrix that

related to the mass density ρ and the shear module μ . \mathbf{U} is the displacement unknowns in z direction. \mathbf{A} and \mathbf{H} for square lattice of anti-plane problems are respectively given as

$$\mathbf{A} = \begin{bmatrix} \Delta\tilde{\varphi}(\mathbf{x}_0) & \mathbf{0} \\ \mathbf{0} & \Delta\tilde{\varphi}(\mathbf{x}_1) \\ \frac{\partial\tilde{\varphi}(\mathbf{x}_{\Gamma_1})}{\partial\mathbf{n}} - \frac{\partial\tilde{\varphi}(\mathbf{x}_{\Gamma_3})}{\partial\mathbf{n}} e^{-ik_x a} & \mathbf{0} \\ \frac{\partial\tilde{\varphi}(\mathbf{x}_{\Gamma_2})}{\partial\mathbf{n}} - \frac{\partial\tilde{\varphi}(\mathbf{x}_{\Gamma_4})}{\partial\mathbf{n}} e^{-ik_y a} & \mathbf{0} \\ \frac{\partial\tilde{\varphi}(\mathbf{x}_{\Gamma_0}^0)}{\partial\mathbf{n}} & -\frac{\mu_1}{\mu_0} \frac{\partial\tilde{\varphi}(\mathbf{x}_{\Gamma_0}^1)}{\partial\mathbf{n}} \end{bmatrix}, \quad (5.2.6)$$

$$\mathbf{H} = \begin{bmatrix} \frac{\rho_0}{\mu_0} \delta_{x_0 x} & \mathbf{0} \\ \mathbf{0} & \frac{\rho_1}{\mu_1} \delta_{x_1 x} \\ \mathbf{0} & \mathbf{0} \\ \mathbf{0} & \mathbf{0} \\ \mathbf{0} & \mathbf{0} \end{bmatrix}, \quad (5.2.7)$$

where $\mathbf{x}_0 \in D^0$, $\mathbf{x}_{\Gamma_i} \in \Gamma_i$ ($i=1, \dots, 4$), $\mathbf{x}_0^0 \in \Gamma_0 \cup D^0$, $\mathbf{x}_1 \in D^1$, $\mathbf{x}_0^1 \in \Gamma_0 \cup D^1$. If we order the discrete displacement unknowns at boundary and interior nodes, then we can define

$$\mathbf{U} = [\mathbf{u}(\mathbf{x}^0), \mathbf{u}(\mathbf{x}^1), \mathbf{u}(\mathbf{x}_{\Gamma_1}), \mathbf{u}(\mathbf{x}_{\Gamma_2}), \mathbf{u}(\mathbf{x}_{\Gamma_3}), \mathbf{u}(\mathbf{x}_{\Gamma_4}), \mathbf{u}(\mathbf{x}_{\Gamma_0}^0), \mathbf{u}(\mathbf{x}_{\Gamma_0}^1)]^T, \quad (5.2.8)$$

$$\mathbf{A} = [\mathbf{A}^0, \mathbf{A}^1, \mathbf{A}_{\Gamma_1}, \mathbf{A}_{\Gamma_2}, \mathbf{A}_{\Gamma_3}, \mathbf{A}_{\Gamma_4}, \mathbf{A}_{\Gamma_0}^0, \mathbf{A}_{\Gamma_0}^1], \quad (5.2.9)$$

$$\mathbf{H} = [\mathbf{H}^0, \mathbf{H}^1, \mathbf{H}_{\Gamma_1}, \mathbf{H}_{\Gamma_2}, \mathbf{H}_{\Gamma_3}, \mathbf{H}_{\Gamma_4}, \mathbf{H}_{\Gamma_0}^0, \mathbf{H}_{\Gamma_0}^1], \quad (5.2.10)$$

if we order the node distribution at \mathbf{x}_0 and \mathbf{x}_1 , we can easily obtain Eq. (5.2.9),

where $\mathbf{A}^0, \mathbf{A}_{\Gamma_i}$ ($i=1, \dots, 4$) and $\mathbf{A}_{\Gamma_0}^0$ are respectively the columns that related to the nodes at \mathbf{x} located on D^0 , Γ_i ($i=1, \dots, 4$) and Γ_0 . The left- and right-hand sides of Eq. (5.2.5) can be written explicitly as

$$\begin{aligned}
AU &= A^0 \mathbf{u}(\mathbf{x}^0) + A^1 \mathbf{u}(\mathbf{x}^1) + A_{\Gamma_1} \mathbf{u}(\mathbf{x}_{\Gamma_1}) + A_{\Gamma_2} \mathbf{u}(\mathbf{x}_{\Gamma_2}) \\
&\quad + A_{\Gamma_3} \mathbf{u}(\mathbf{x}_{\Gamma_3}) + A_{\Gamma_4} \mathbf{u}(\mathbf{x}_{\Gamma_4}) + A_{\Gamma_0}^0 \mathbf{u}(\mathbf{x}_{\Gamma_0}^0) + A_{\Gamma_0}^1 \mathbf{u}(\mathbf{x}_{\Gamma_0}^1),
\end{aligned} \tag{5.2.11}$$

$$\begin{aligned}
HU &= H^0 \mathbf{u}(\mathbf{x}^0) + H^1 \mathbf{u}(\mathbf{x}^1) + H_{\Gamma_1} \mathbf{u}(\mathbf{x}_{\Gamma_1}) + H_{\Gamma_2} \mathbf{u}(\mathbf{x}_{\Gamma_2}) \\
&\quad + H_{\Gamma_3} \mathbf{u}(\mathbf{x}_{\Gamma_3}) + H_{\Gamma_4} \mathbf{u}(\mathbf{x}_{\Gamma_4}) + H_{\Gamma_0}^0 \mathbf{u}(\mathbf{x}_{\Gamma_0}^0) + H_{\Gamma_0}^1 \mathbf{u}(\mathbf{x}_{\Gamma_0}^1).
\end{aligned} \tag{5.2.12}$$

Now the displacement periodicity conditions (2.2.5) of the unit-cell and the displacement continuity condition on the matrix-scatterer's interface have to be taken into consideration, which can be rewritten into the following forms

$$\mathbf{u}(\mathbf{x}_{\Gamma_1}) = \mathbf{u}(\mathbf{x}_{\Gamma_3}) e^{-ik_x a}, \quad \mathbf{u}(\mathbf{x}_{\Gamma_2}) = \mathbf{u}(\mathbf{x}_{\Gamma_4}) e^{-ik_y a}, \quad \mathbf{u}(\mathbf{x}_{\Gamma_0}^1) = \mathbf{u}_0(\mathbf{x}_{\Gamma_0}^0). \tag{5.2.13}$$

Substitution of Eq. (5.2.13) into Eqs. (5.2.12) and (5.2.11) results in

$$\begin{aligned}
AU &= A^0 \mathbf{u}(\mathbf{x}^0) + A^1 \mathbf{u}(\mathbf{x}^1) + (A_{\Gamma_1} + A_{\Gamma_3} e^{ik_x a}) \mathbf{u}(\mathbf{x}_{\Gamma_1}) \\
&\quad + (A_{\Gamma_2} + A_{\Gamma_4} e^{ik_y a}) \mathbf{u}(\mathbf{x}_{\Gamma_2}) + (A_{\Gamma_0}^0 + A_{\Gamma_0}^1) \mathbf{u}(\mathbf{x}_{\Gamma_0}^0), \\
HU &= H^0 \mathbf{u}(\mathbf{x}^0) + H^1 \mathbf{u}(\mathbf{x}^1) + (H_{\Gamma_1} + H_{\Gamma_3} e^{ik_x a}) \mathbf{u}(\mathbf{x}_{\Gamma_1}) \\
&\quad + (H_{\Gamma_2} + H_{\Gamma_4} e^{ik_y a}) \mathbf{u}(\mathbf{x}_{\Gamma_2}) + (H_{\Gamma_0}^0 + H_{\Gamma_0}^1) \mathbf{u}(\mathbf{x}_{\Gamma_0}^0),
\end{aligned}$$

then, Eq. (5.2.5) can be rewritten as the following generalized eigenvalue equation

$$\tilde{A} \tilde{U} = -\omega^2 \tilde{H} \tilde{U}, \tag{5.2.14}$$

where

$$\begin{aligned}
\tilde{A} &= \left[A^0, A^1, A_{\Gamma_1} + A_{\Gamma_3} e^{ik_x a}, A_{\Gamma_2} + A_{\Gamma_4} e^{ik_y a}, A_{\Gamma_0}^0 + A_{\Gamma_0}^1 \right], \\
\tilde{H} &= \left[H^0, H^1, H_{\Gamma_1} + H_{\Gamma_3} e^{ik_x a}, H_{\Gamma_2} + H_{\Gamma_4} e^{ik_y a}, H_{\Gamma_0}^0 + H_{\Gamma_0}^1 \right], \\
\tilde{U} &= \left[\mathbf{u}(\mathbf{x}^0), \mathbf{u}(\mathbf{x}^1), \mathbf{u}(\mathbf{x}_{\Gamma_1}), \mathbf{u}(\mathbf{x}_{\Gamma_2}), \mathbf{u}(\mathbf{x}_{\Gamma_0}^0) \right]^T.
\end{aligned}$$

In this manner, smaller matrices \tilde{H} , \tilde{A} and the reduced displacement vector \tilde{U} are obtained. The displacement periodicity conditions on the boundary of the unit-cell and the displacement continuity condition on the matrix-scatterer's interface are automatically satisfied, which significantly improves the stability of the present RBF collocation method.

5.1.4 Discretized periodic boundary conditions of triangular lattice

For the triangular lattice, as show in Fig. 5.2, the governing equation and the

continuity conditions are the same, however we have the following 3 boundary conditions (5.2.15) and (5.2.16), which are different from that for the square lattice.

$$u(\mathbf{x}_{\Gamma_1}) = u(\mathbf{x}_{\Gamma_4})e^{-i(k_x \frac{\sqrt{3}}{2}a + k_y \frac{a}{2})}, \quad u(\mathbf{x}_{\Gamma_2}) = u(\mathbf{x}_{\Gamma_5})e^{-ik_y a}, \quad u(\mathbf{x}_{\Gamma_3}) = u(\mathbf{x}_{\Gamma_6})e^{-i(-k_x \frac{\sqrt{3}}{2}a + k_y \frac{a}{2})}, \quad (5.2.15)$$

$$T(\mathbf{x}_{\Gamma_1}) = T(\mathbf{x}_{\Gamma_4})e^{-i(k_x \frac{\sqrt{3}}{2}a + k_y \frac{a}{2})}, \quad T(\mathbf{x}_{\Gamma_2}) = T(\mathbf{x}_{\Gamma_5})e^{-ik_y a}, \quad T(\mathbf{x}_{\Gamma_3}) = T(\mathbf{x}_{\Gamma_6})e^{-i(-k_x \frac{\sqrt{3}}{2}a + k_y \frac{a}{2})}, \quad (5.2.16)$$

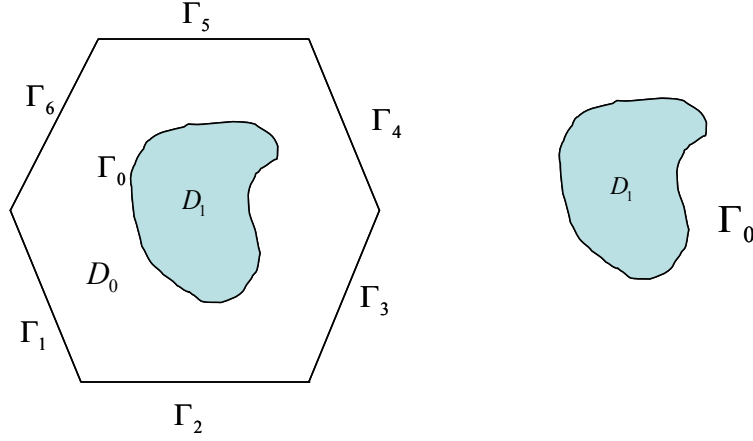


Fig. 5.2 Matrix and scatterer in a unit-cell of a triangular lattice

where $\mathbf{x}_{\Gamma_i} \in \Gamma_i$ ($i=1,2,\dots,6$), and $\mathbf{T}(\mathbf{x})$ is the boundary traction vector of anti-plane elastic wave. The equation of motion, the displacement continuity and the traction equilibrium conditions are the same as for the square lattice. By taking the equation of motion, the traction periodicity conditions (5.2.16) on the boundary of the unit-cell and the traction equilibrium condition (2.2.5) on the matrix-scatterer's interface into account, we obtain the eigenvalue equation in the following matrix form

$$\begin{bmatrix}
\Delta u(\mathbf{x}^0) & 0 \\
0 & \Delta u(\mathbf{x}^1) \\
\frac{\partial u(\mathbf{x}_{\Gamma_1})}{\partial \mathbf{n}} - \frac{\partial u(\mathbf{x}_{\Gamma_4})}{\partial \mathbf{n}} e^{-i(k_x \frac{\sqrt{3}}{2} a + k_y \frac{a}{2})} & 0 \\
\frac{\partial u(\mathbf{x}_{\Gamma_2})}{\partial \mathbf{n}} - \frac{\partial u(\mathbf{x}_{\Gamma_5})}{\partial \mathbf{n}} e^{-ik_y a} & 0 \\
\frac{\partial u(\mathbf{x}_{\Gamma_3})}{\partial \mathbf{n}} - \frac{\partial u(\mathbf{x}_{\Gamma_6})}{\partial \mathbf{n}} e^{-i(-k_x \frac{\sqrt{3}}{2} a + k_y \frac{a}{2})} & 0 \\
\frac{\partial u(\mathbf{x}_{\Gamma_0}^0)}{\partial \mathbf{n}} & -\frac{\mu_1}{\mu_0} \frac{\partial u(\mathbf{x}_{\Gamma_0}^1)}{\partial \mathbf{n}}
\end{bmatrix} = -\omega^2 \begin{bmatrix}
\frac{\rho_0}{\mu_0} u(\mathbf{x}^0) & 0 \\
0 & \frac{\rho_1}{\mu_1} u(\mathbf{x}^1) \\
0 & 0
\end{bmatrix}. \quad (5.2.17)$$

Following the same procedure as for the square lattice and considering the displacement periodicity conditions (5.2.15) as well as the displacement continuity condition (2.2.2) on the matrix-scatterer's interface, we finally obtain the same eigenvalue equation Eq. with

$$\tilde{\mathbf{A}} = \begin{bmatrix}
\mathbf{A}^0, \mathbf{A}^1, \mathbf{A}_{\Gamma_1} + \mathbf{A}_{\Gamma_4} e^{-i(k_x \frac{\sqrt{3}}{2} a + k_y \frac{a}{2})}, \mathbf{A}_{\Gamma_2} + \mathbf{A}_{\Gamma_5} e^{-ik_y a}, \\
\mathbf{A}_{\Gamma_3} + \mathbf{A}_{\Gamma_6} e^{-i(-k_x \frac{\sqrt{3}}{2} a + k_y \frac{a}{2})}, \mathbf{A}_{\Gamma_0}^0 + \mathbf{A}_{\Gamma_0}^1
\end{bmatrix}, \quad (5.2.18)$$

$$\tilde{\mathbf{U}} = [u(\mathbf{x}^0), u(\mathbf{x}^1), u(\mathbf{x}_{\Gamma_1}), u(\mathbf{x}_{\Gamma_2}), u(\mathbf{x}_{\Gamma_3}), u(\mathbf{x}_{\Gamma_0}^0)]^T. \quad (5.2.19)$$

The detailed expressions of the matrices \mathbf{A} and \mathbf{H} are given

$$\mathbf{A} = \begin{bmatrix}
\Delta \tilde{\varphi}(\mathbf{x}_0) & 0 \\
0 & \Delta \tilde{\varphi}(\mathbf{x}_1) \\
\frac{\partial \tilde{\varphi}(\mathbf{x}_{\Gamma_1})}{\partial \mathbf{n}} - \frac{\partial \tilde{\varphi}(\mathbf{x}_{\Gamma_4})}{\partial \mathbf{n}} e^{-i(k_x \frac{\sqrt{3}}{2} a + k_y \frac{a}{2})} & 0 \\
\frac{\partial \tilde{\varphi}(\mathbf{x}_{\Gamma_2})}{\partial \mathbf{n}} - \frac{\partial \tilde{\varphi}(\mathbf{x}_{\Gamma_5})}{\partial \mathbf{n}} e^{-ik_y a} & 0 \\
\frac{\partial \tilde{\varphi}(\mathbf{x}_{\Gamma_3})}{\partial \mathbf{n}} - \frac{\partial \tilde{\varphi}(\mathbf{x}_{\Gamma_6})}{\partial \mathbf{n}} e^{-i(-k_x \frac{\sqrt{3}}{2} a + k_y \frac{a}{2})} & 0 \\
\frac{\partial \tilde{\varphi}(\mathbf{x}_{\Gamma_0}^0)}{\partial \mathbf{n}} & -\frac{\mu_1}{\mu_0} \frac{\partial \tilde{\varphi}(\mathbf{x}_{\Gamma_0}^1)}{\partial \mathbf{n}}
\end{bmatrix}, \quad (5.2.20)$$

$$\mathbf{B} = \begin{bmatrix} \frac{\rho_0}{\mu_0} \delta_{x_0 x} & \mathbf{0} \\ \mathbf{0} & \frac{\rho_1}{\mu_1} \delta_{x_1 x} \\ \mathbf{0} & \mathbf{0} \\ \mathbf{0} & \mathbf{0} \\ \mathbf{0} & \mathbf{0} \end{bmatrix}. \quad (5.2.21)$$

The generalized eigenvalue equation (5.2.14) can be solved numerically by using the eigensolver in MATLAB.

5.2 Numerical results and discussions

5.2.1 Effects of the shape parameter

The LRBFCM combined with the special techniques proposed in Chapter 2 are validated by comparison of the numerical results with that obtained by the finite element method of the acoustics module in COMSOL Multiphysics. The multi-quadratic (MQ) RBF is adopted in the present meshfree LRBFCM in the whole thesis. A uniform node distribution is used for all numerical calculations in this chapter. It was found in a previous study that a uniform node distribution has a slightly better convergence rate than a random distribution of equal size 88, and our test results of the random node distribution also verifies this finding.

Another important factor in the RBF is the shape parameter ξ in the RBF, which could affect the results of the RBF collocation methods. According to many pervious works [138, 139], the shape parameter is related to the distance of the nodes nearby. There are several ways to find an optimal shape parameter, such as the golden search method, and so on [140, 141]. One key point to determine the optimal shape parameter is to calculate the errors at the boundary or the residuals of the governing equations. Here we use a simple way to determine the shape parameter, which aer described in the following. We select a simple function, such as $u=x+y$ or $u=\sin(x)\cos(y)$, then Lu can be evaluated analytically, where L is the Laplace operator.

Then, we compare the analytical result of Lu and the result of the RBFCM from Eq. and define an error indicator

$$\text{Error}(c_s) = |Lu - L\tilde{u}|, \quad (5.3.1)$$

where $L\tilde{u}$ is the numerical result of a node, and Lu is the exact solution that we employed. A pre-calculation is done to find out the shape parameter that has the smallest error. We give the node distribution and the shape parameter in our numerical examples in following.

5.2.2 Aurum scatterers embedded in epoxy matrix

In this subsection, aurum (Au) cylinders embedded in the epoxy matrix are considered. The densities and the wave velocities of the component materials are given by: $\rho_0 = 1180 \text{ kg/m}^3$, $c_0 = 1161 \text{ m/s}$, $\rho_1 = 19500 \text{ kg/m}^3$, and $c_1 = 1239 \text{ m/s}$. Thus, the acoustic impedance ratio of the considered phononic crystal is $Z = \rho_1 c_1 / \rho_0 c_0 = 17.64$, which is large.

The first example considers both square and circular scatterers in a square lattice. The filling fraction of the aurum/epoxy phononic crystal with square scatterers is 0.138, the area of the square scatterer is 0.4×0.4 and the unit-cell area is 1×1 . Fig. 5.3 shows the node distribution of the aurum/epoxy phononic crystal in a square lattice with square scatterers. Here, 31×31 nodes are uniformly distributed in the domain. In this case the direct method for computing the normal derivative of the displacement could be easily applied to all the boundary nodes, and the results of the direct method are shown in Fig. 5.4. However, in order to show the stability of the fictitious nodes method the corresponding results by using the fictitious nodes method for all boundary nodes are also shown in Fig. 5.5. The shape parameter is chosen as $\xi = 3$ and 9 local nodes are employed for both fictitious nodes method and direct method. From Fig. 5.4 and Fig. 5.5, we can find that both methods could lead to a stable LRBFEM, and the results are fitting quite well with the FEM results.

However, our numerical results indicate that the direct method keeps stable in the

range of $\xi = 0.1$ to $\xi = 50$, while the shape parameter is limited to the range of $\xi = 0.2$ to $\xi = 8$ when the fictitious nodes method is employed. This means that the direct method for computing the normal derivative of the displacement is much better than the fictitious nodes method with respect to the stability of the LRBFCM.

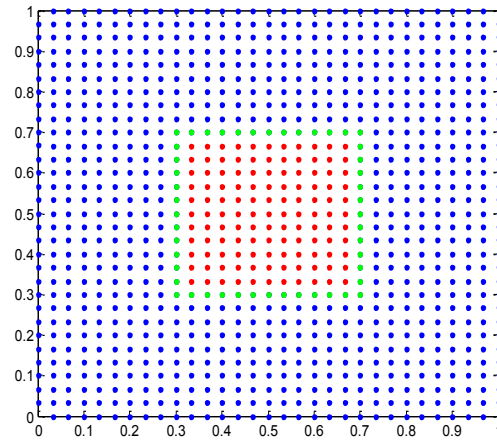


Fig. 5.3 Node distribution of the arium/epoxy phononic crystal in a square lattice with square scatterers.

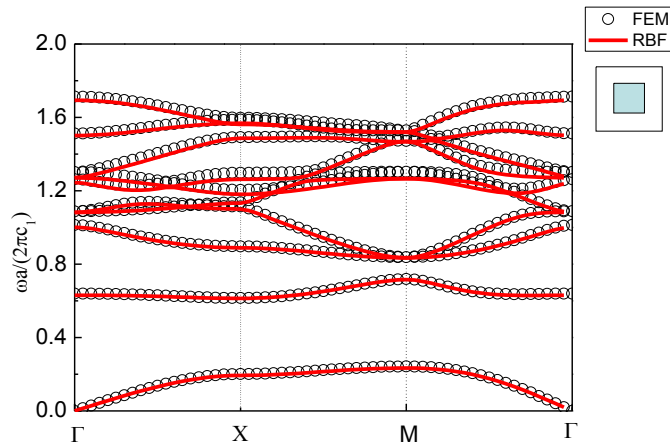


Fig. 5.4 Band structure of the arium/epoxy phononic crystal in a square lattice with square scatterers by the direct method (Γ , X and M are the characteristic points in the first Brillouin zone as shown in Fig. 2.3).

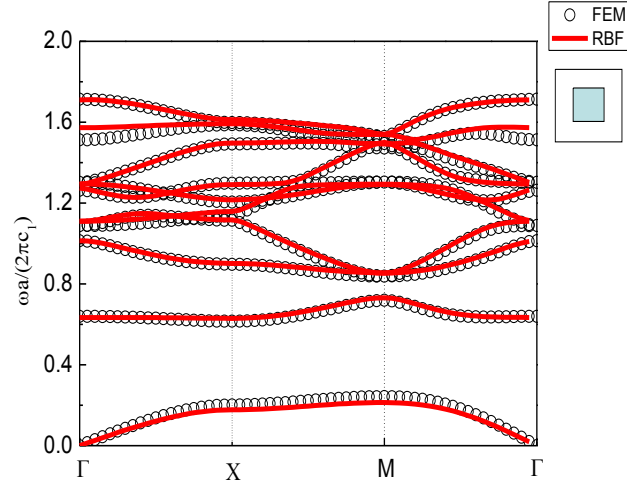


Fig. 5.5 Band structure of the aurum/epoxy phononic crystal in a square lattice with square scatterers by the fictitious nodes method.

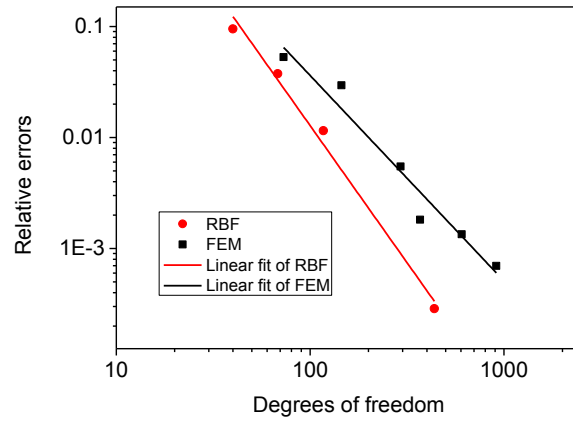


Fig. 5.6 Convergence rates of the averaged eigenvalues for the aurum/epoxy phononic crystal in a square lattice with square scatterers.

In Fig. 5.6, the convergence rate of the direct method for the average of all eigenvalues is given in terms of the relative error $(E_r - E_m)/E_r$, where E_r is the result of the present LRBF method by using 1681 nodes or degrees of freedom, and E_m is the result of the LRBF method or the FEM with the actual degrees of freedom. In Fig. 5.6, $\log_{10}(\cdot)$ scale is used for convenience, and different FE meshes including coarse, fine and very fine meshes are tested. From Fig. 5.6 we can see that a number of more than 100 nodes should be guaranteed to keep an acceptable accuracy, and the order of the accuracy can easily reach 10^{-3} with more than about 120 nodes. From the results

in Fig. 5.6, it can be easily seen that with the same degrees of freedom, the present LRBFCM can generally lead to more accurate results than the FEM. Fig. 5.6 also shows that in the $\log_{10}(\cdot)$ scale the relative error decreases more or less linearly with increasing degrees of freedom in both methods, but the linearly fitted error curve of the LRBFCM has a larger slope than that of the FEM, which implies that the convergence rate of the present LRBFCM is higher than that of the FEM. In the following analysis, more than 1000 degrees of freedom are employed in the FEM for the comparison purposes.

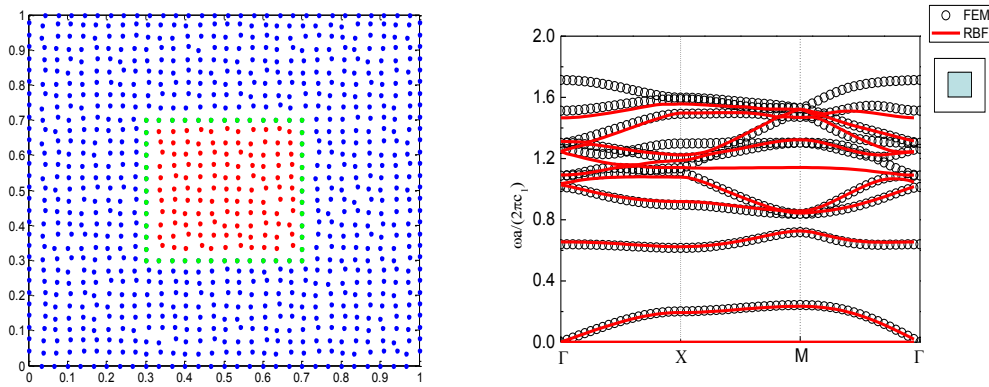


Fig. 5.7 Band structure of the aurum/epoxy phononic crystal in a square lattice with square scatterers by the fictitious nodes method (right) with strongly disordered node distribution (left).

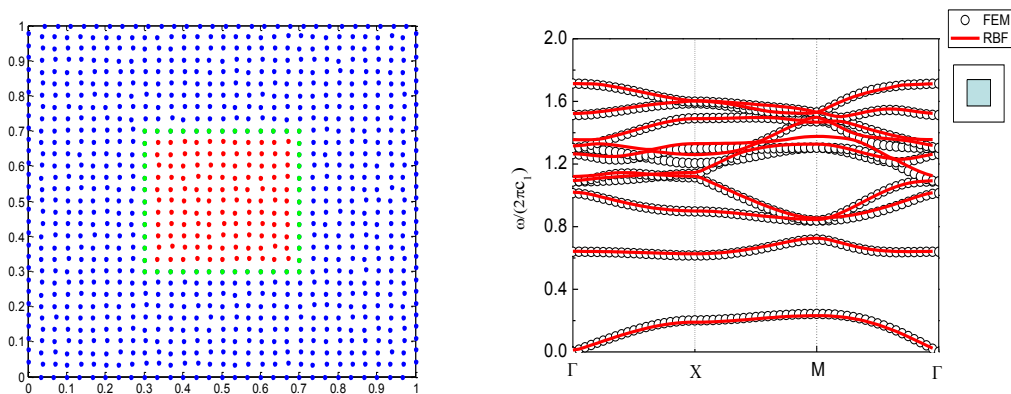


Fig. 5.8 Band structure of the aurum/epoxy phononic crystal in a square lattice with square scatterers by the fictitious nodes method (right) with weakly disordered node distribution (left).

Fig. 5.7 and Fig. 5.8 show the effects of the random node distribution on the

numerical results. Here, we add a certain disorder in the node distribution, where the node distribution in Fig. 5.7 is more disordered than in Fig. 5.8. As disordered nodes are applied, only fictitious nodes method can be employed for the treatment at the boundaries and the interface. The results show that if the node distribution is more disordered, the results become much worse, which confirms the same conclusion drawn in the previous work [142].

In the second example as shown Fig. 5.9, a square lattice with circular scatterers is considered. A uniform distribution of total 948 nodes is used. The filling fraction is 0.196, the radius of the circular scatterers is 0.25, and some line nodes are added in order to easily get more nodes on the interface boundary. Fig. 5.10 shows the results by using the direct method on the boundary of the scatterer and the indirect method on the interface boundary belonging to the matrix. Fig. 5.11 shows the results by using the fictitious nodes method for all the boundary nodes. As we can see that in the low frequency range, the results of the LRFBCM and the FEM agree very well, while in the high frequency range both results show a little difference but they are still in a good agreement in general. The shape parameter used in both Fig. 5.10 and Fig. 5.11 is $c_s = 3$ and the local nodes number is 9.

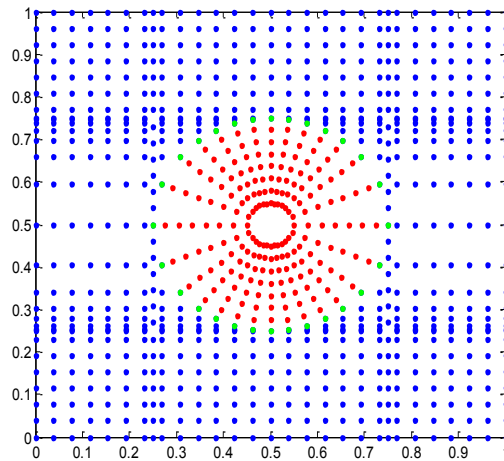


Fig. 5.9 Node distribution of the aurum/epoxy phononic crystal in a square lattice with circular scatterers.

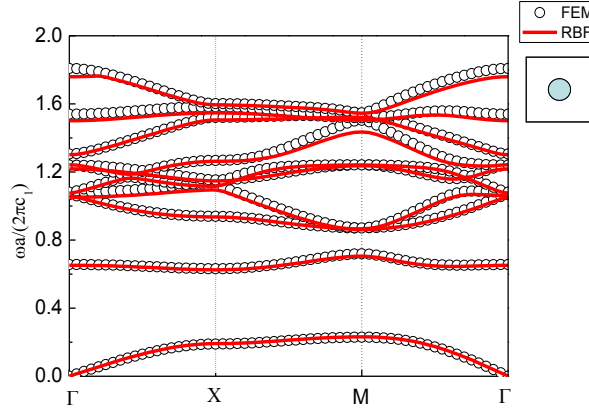


Fig. 5.10 Band structure of the aurnum/epoxy phononic crystal in a square lattice with circular scatterers by the direct and indirect methods.

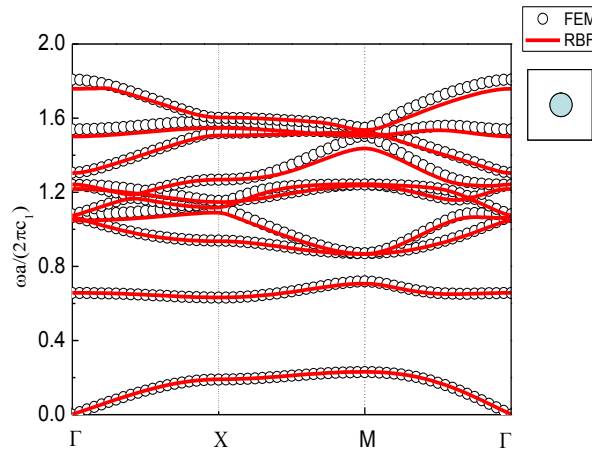


Fig. 5.11 Band structure of the aurnum/epoxy phononic crystal in a square lattice with circular scatterers by the fictitious nodes method.

5.2.3 Aluminum scatterers embedded in epoxy matrix

In this subsection, we consider the aluminium (Al) scatterers embedded in the epoxy matrix. The material parameters are given by $\rho_0 = 1180 \text{ kg/m}^3$, $c_0 = 1161 \text{ km/s}$, $\rho_1 = 2730 \text{ kg/m}^3$ and $c_1 = 3242 \text{ km/s}$. The corresponding acoustic impedance ratio of the phononic crystal is $Z = \rho_1 c_1 / \rho_0 c_0 = 6.46$, which is smaller than that of the previous example.

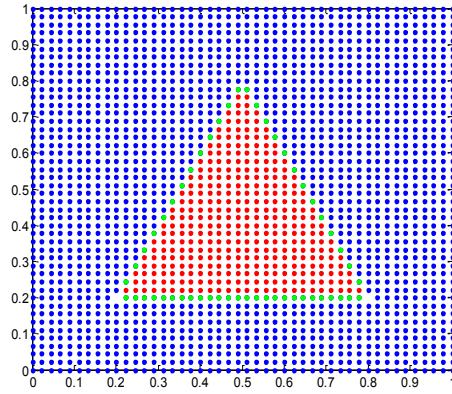


Fig. 5.12 Node distribution of the aluminium/epoxy phononic crystal in a square lattice with triangular scatterers

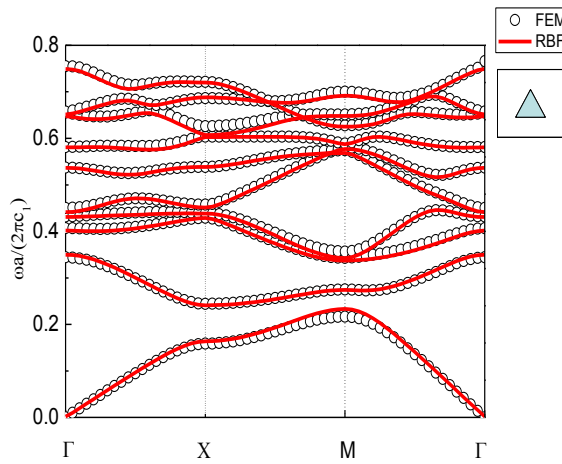


Fig. 5.13 Band structure of the aluminium/epoxy phononic crystal in a square lattice with triangular scatterers by the indirect/direct method.

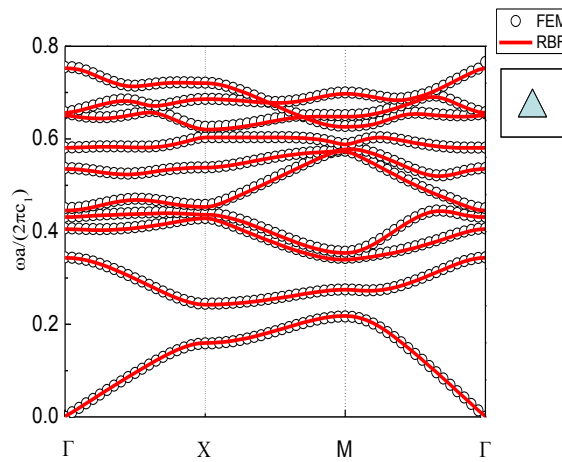


Fig. 5.14 Band structure of the aluminium/epoxy phononic crystal in a square lattice with triangular scatterers by the fictitious nodes method.

In the first case as shown in Fig. 5.12, the triangular scatterers in a square lattice are considered. Here, totally 2114 nodes are uniformly distributed. In order to match the local geometry and the node distribution near the boundary of the triangular lattice. The local nodes number is taken as 11, and the shape parameter in the RBF is selected as $\xi = 1$. The filling fraction is 0.18. For the node distribution as shown in Fig. 5.12, the indirect method could be applied to the interface and the direct method is employed at the boundary of the unit-cell. Fig. 5.13 shows the results by using the indirect method for the interface boundary and the direct method for the matrix boundaries, while Fig. 5.14 shows the results by using the fictitious nodes method for all the boundaries. Both figures show a good agreement with the FEM results.

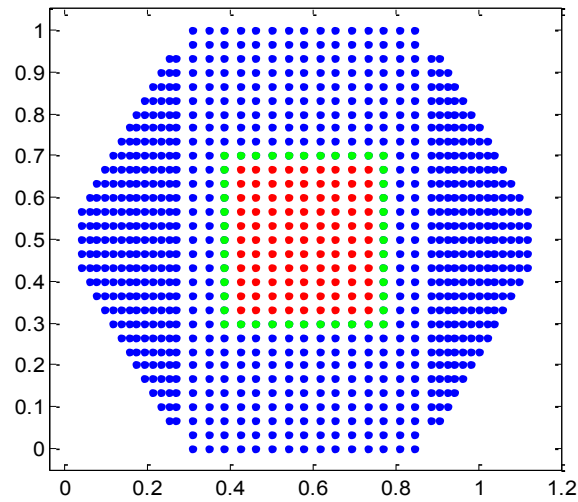


Fig. 5.15 Node distribution of the aluminium/epoxy phononic crystal in a triangular lattice with square scatterers.

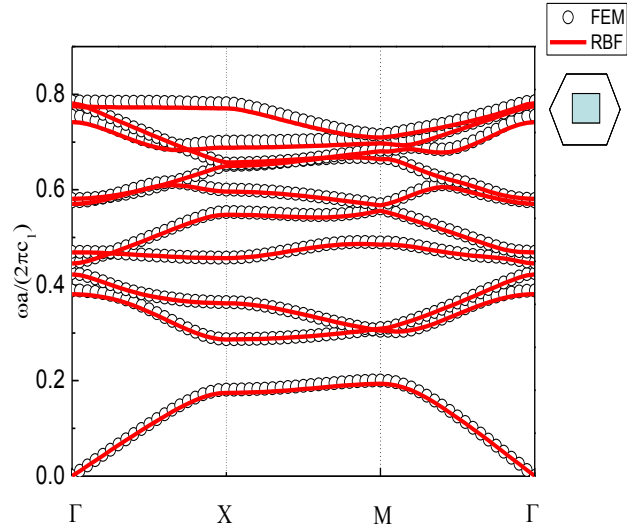


Fig. 5.16 Band structure of the aluminium/epoxy phononic crystal in a triangular lattice with square scatterers by the direct/indirect method.

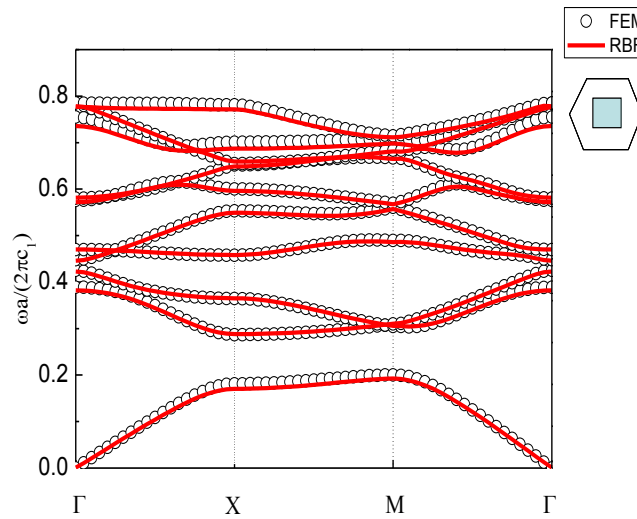


Fig. 5.17 Band structure of the aluminium/epoxy phononic crystal in a triangular lattice with square scatterers by the fictitious nodes method.

Finally, we consider a triangular lattice with square scatterers as shown in Fig. 5.15. In this case, a uniform node distribution with total 903 nodes is used, the filling fraction is chosen as 0.138, the local nodes number is 11, and the shape parameter is $\xi = 3$. Fig. 5.16 shows the results by using the indirect method for the boundary of the unit-cell and the direct method for the boundary of the square scatterer. Fig. 5.17

shows the corresponding results by using the fictitious nodes method for all boundaries of the unit-cell and the scatterer. Here again, both results show a quite good agreement with the FEM results. All the numerical results demonstrate that the present LRBFCM is suitable and efficient for the band structure calculation of the phononic crystals. The stability of the LRBFCM can be greatly improved by using our proposed special techniques for computing the normal derivative of the displacement needed for the treatment of the boundary conditions.

5.3 Analysis of the computational efficiency

The computational efficiency of the LRBFCM is analysed and discussed in this subsection. The computational costs of the present LRBFCM for the numerical examples considered previously are given in Table 1 and they are compared with that of the FEM. The error in Table 1 is defined as $|E_f - E_r|/E_f$, in which E_f is the result of the FEM by using COMSOL Multiphysics and E_r is the result of the present LRBFCM. All the programs are run on the same laptop with Intel(R) Core(TM) i7-4510U, 2.00 GHz CPU and 8 GB RAM.

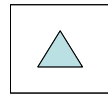
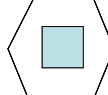
Lattice form		Square			Triangular
Scatterer form		Square	Circular	Triangular	Square
					
RBF	Number of nodes	441	948	1294	903
	Time cost [s]	8.124	40.49	66.096	39.19
FEM	Degrees of freedom	1401	1533	1265	837
	Time cost [s]	139	135	137	129
Comparison	Errors	0.0097	0.0126	0.0098	0.0081
	Time saving	94%	70%	51%	69%

Table 5.1 Computing time and accuracy comparisons.

From Table 5.1, we can easily find that for the square lattice with square scatterers, 441 nodes could already lead to a high accuracy with a saving of 96%

computing time compared with the FEM. We also mention that the degrees of freedom (DF) are 1401 in the FEM, which could be reduced to keep the same accuracy. However, it is rather cumbersome to reduce or change the meshes as we want in the COMSOL Multiphysics.

When 948 nodes are employed for the square lattice with circular scatterers, the computing time saving is still 70% in comparison to the FEM. The error of the present LRBFCM compared with the FEM is 0.0126. This reduced accuracy might come from the difference of the circular interface approximated by the triangular meshes in the FEM and the LRBFCM. In the present meshfree method, the circular interface can be exactly approximated while in the FEM the circular interface is only approximately replaced by using piecewise straight lines of the triangular meshes.

For the square lattice with triangular scatterers, more nodes are used to take the complex geometry near the tips of the triangular scatterer into account. In this case, the computing time saving of the present LRBFCM is 51% compared with the FEM. Here, 1294 nodes are used in the LRBFCM, while 1265 degrees of freedom are employed in the FEM. In this example, the number of the unknowns in the present LRBFCM is almost the same as that in the FEM. Thus, it could be concluded that the efficiency of the LRBFCM is generally higher than the FEM for the same number of unknowns or degrees of freedom.

For the triangular lattice with square scatterers, the computing time saving is 69% compared with the FEM, and the accuracy is still pretty high. In this example, 903 nodes are employed in the LRBFCM compared with 837 degrees of freedom in the FEM. Even with some more unknowns, the efficiency of the present LRBFCM is still higher than the FEM in this case.

From the above discussions, we can conclude that the efficiency and the stability of the present meshfree LRBFCM are very high for band structure calculations of 2D phononic crystals. In addition, the present LRBFCM is a truly meshfree method, which has certain advantages compared to other domain-type computational methods such as the FEM and the finite difference method. For instance, the node creation in the present method is easier than the mesh generation in the FEM, which is beneficial

for the pre- and post-processing of the computational data. With respect to the adaptivity of the computational methods and the moving boundary-value problems (crack propagation, free or moving boundary problems like ice melting or phase change problems, etc.), the present meshfree method is also advantageous because the insertion of additional nodes is much simpler than the remeshing in the domain-type methods. Nevertheless, the computational code of the present LRBFCM is self-developed in-house, while the FEM used for the verification purpose is a commercial and optimized software package. In this sense, the present computational code can be further improved and optimized to increase its efficiency and accuracy.

5.4 Summary

In this chapter the LRBFCM is presented for the band structure calculations of the anti-plane transverse elastic wave propagation in 2D phononic crystals. The numerical results show that the three different techniques for computing the normal derivatives of the displacement at the boundary conditions in the LRBFCM greatly enhance the stability of the present LRBFCM. The results also prove that the performances of the indirect method and the direct method are much better than the fictitious nodes method. The developed LRBFCM is verified by using the results obtained with the FEM. The effects of the shape parameter of the RBF, the number of the used nodes and the node distribution on the numerical results are investigated. Numerical results for square, circular and triangular scatterers in square and triangular lattices with different acoustic impedance ratios and material properties are presented and discussed. The performance and the efficiency of the present LRBFCM in comparison to the FEM are analysed and revealed. The results show that the present meshfree LRBFCM is a promising alternative numerical tool for computing phononic band structures.

Chapter 6

Local RBF-CM for in-plane elastic wave propagation analysis in 2D solid/solid phononic crystals

In this chapter, the LRBFCM combined with indirect method is employed to calculate the in-plane elastic waves of the phononic crystals. The general form of LRBFCM for the in-plane elastic waves is given in section 6.1. The numerical results are discussed in section 6.2. The the computational efficiency are fully compared with FEM in 6.3. Then some remarks are given in the last section 6.4.

6.1 LRBFCM formulation of the eigenvalue problems

In this section, the LRBFCM discretization form for the governing equation, and continuity conditions, and the periodic boundary conditions of different lattice are going to be discussed separately. The boundary value problem of in-plane elastic wave propagation in 2D phononic crystals determined by the elastodynamic wave equations (2.3.1) and (2.3.2), the periodic boundary conditions (2.3.5) and (2.3.6) on the boundaries of the unit-cell, and the displacement continuity conditions (2.3.3) as well as the traction equilibrium conditions (2.3.4) can be solved by the LRBFCM.

6.1.1 Discretized governing equations

In order to solve the governing equation (2.3.1) and (2.3.2), the displacements in the x - and y -direction are approximated in the LRBFCM as followings by using (3.2.11) to (3.2.13),

$$u_x(\mathbf{x}) = \tilde{\boldsymbol{\varphi}}(\mathbf{x})\tilde{\mathbf{u}}_x, \quad u_y(\mathbf{x}) = \tilde{\boldsymbol{\varphi}}(\mathbf{x})\tilde{\mathbf{u}}_y, \quad (6.1.1)$$

where $\tilde{\mathbf{u}}_x = [u_x(\mathbf{x}_1), u_x(\mathbf{x}_2), \dots, u_x(\mathbf{x}_n)]^T$ and $\tilde{\mathbf{u}}_y = [u_y(\mathbf{x}_1), u_y(\mathbf{x}_2), \dots, u_y(\mathbf{x}_n)]^T$. Then the governing equation (2.3.1) and (2.3.2) are expressed as

$$\left((\lambda_j + 2\mu_j) \frac{\partial^2 \tilde{\boldsymbol{\varphi}}(\mathbf{x})}{\partial x^2} + \mu_j \frac{\partial^2 \tilde{\boldsymbol{\varphi}}(\mathbf{x})}{\partial y^2} \right) \tilde{\mathbf{u}}_x^j + (\lambda_j + \mu_j) \frac{\partial^2 \tilde{\boldsymbol{\varphi}}(\mathbf{x})}{\partial x \partial y} \tilde{\mathbf{u}}_y^j = -\rho_j \omega^2 \tilde{\boldsymbol{\varphi}}(\mathbf{x}) \tilde{\mathbf{u}}_x^j, \quad (6.1.2)$$

$$\left((\lambda_j + 2\mu_j) \frac{\partial^2 \tilde{\varphi}(\mathbf{x})}{\partial y^2} + \mu_j \frac{\partial^2 \tilde{\varphi}(\mathbf{x})}{\partial x^2} \right) \tilde{\mathbf{u}}_y^j + (\lambda_j + \mu_j) \frac{\partial^2 \tilde{\varphi}(\mathbf{x})}{\partial x \partial y} \tilde{\mathbf{u}}_x^j = -\rho_j \omega^2 \tilde{\varphi}(\mathbf{x}) \tilde{\mathbf{u}}_y^j. \quad (6.1.3)$$

For simplicity we define

$$\mathbf{G}^j(\mathbf{x}) = \left((\lambda_j + 2\mu_j) \frac{\partial^2}{\partial x^2} + \mu_j \frac{\partial^2}{\partial y^2} \right) \tilde{\varphi}(\mathbf{x}), \quad \mathbf{x} \in D_j,$$

$$\mathbf{\Phi}^j(\mathbf{x}) = \left((\lambda_j + 2\mu_j) \frac{\partial^2}{\partial y^2} + \mu_j \frac{\partial^2}{\partial x^2} \right) \tilde{\varphi}(\mathbf{x}), \quad \mathbf{x} \in D_j,$$

$$\mathbf{\Psi}^j(\mathbf{x}) = (\lambda_j + \mu_j) \frac{\partial^2 \tilde{\varphi}(\mathbf{x})}{\partial x \partial y}, \quad \mathbf{x} \in D_j.$$

Then the governing equation (6.1.2) and (6.1.3) can be expressed as

$$\mathbf{G}^j(\mathbf{x}) \mathbf{u}_x^j + \mathbf{\Psi}^j(\mathbf{x}) \mathbf{u}_y^j = -\rho_j \omega^2 \tilde{\varphi}(\mathbf{x}) \tilde{\mathbf{u}}_x^j, \quad (6.1.4)$$

$$\mathbf{\Psi}^j(\mathbf{x}) \mathbf{u}_x^j + \mathbf{\Phi}^j(\mathbf{x}) \mathbf{u}_y^j = -\rho_j \omega^2 \tilde{\varphi}(\mathbf{x}) \tilde{\mathbf{u}}_y^j. \quad (6.1.5)$$

6.1.2 Discretized interface continuity boundary conditions

The continuity boundary conditions are given as Eqs. (2.3.3) and (2.3.4). The Eq. (2.3.3) can be taken as

$$\tilde{\mathbf{u}}_x^0|_{\Gamma_0} = \tilde{\mathbf{u}}_x^1|_{\Gamma_0}, \quad \tilde{\mathbf{u}}_y^0|_{\Gamma_0} = \tilde{\mathbf{u}}_y^1|_{\Gamma_0}, \quad (6.1.6)$$

where $\tilde{\mathbf{u}}_x|_{\Gamma_0}$ and $\tilde{\mathbf{u}}_y|_{\Gamma_0}$ denote the elements of the vectors $\tilde{\mathbf{u}}_x$ and $\tilde{\mathbf{u}}_y$ corresponding to the unit-cell interface $\mathbf{x} \in \Gamma_0$, the Eq. (6.1.6) can be analytically satisfied by adding or subtracting the corresponding columns of the formulated matrix.

By using the definition in Eq. (6.1.1), we can obtain the stress components as

$$\sigma_{xx}^j = (\lambda_j + 2\mu_j) \frac{\partial \tilde{\varphi}}{\partial x} \tilde{\mathbf{u}}_x + \lambda_j \frac{\partial \tilde{\varphi}}{\partial y} \tilde{\mathbf{u}}_y, \quad (6.1.7)$$

$$\sigma_{yy}^j = \lambda_j \frac{\partial \tilde{\varphi}}{\partial x} \tilde{\mathbf{u}}_x + (\lambda_j + 2\mu_j) \frac{\partial \tilde{\varphi}}{\partial y} \tilde{\mathbf{u}}_y, \quad (6.1.8)$$

$$\sigma_{xy}^j = \mu_j \left(\frac{\partial \tilde{\varphi}}{\partial y} \tilde{\mathbf{u}}_x + \frac{\partial \tilde{\varphi}}{\partial x} \tilde{\mathbf{u}}_y \right). \quad (6.1.9)$$

Then the traction components could be expressed as

$$T_x^j(\mathbf{x}) = \sigma_{xx}^j n_x(\mathbf{x}) + \sigma_{xy}^j n_y(\mathbf{x}), \quad \mathbf{x} \in D_j, \quad (6.1.10)$$

$$T_y^j(\mathbf{x}) = \sigma_{yy}^j n_y(\mathbf{x}) + \sigma_{yx}^j n_x(\mathbf{x}), \quad \mathbf{x} \in D_j, \quad (6.1.11)$$

where $\mathbf{n}(\mathbf{x}) = [n_x(\mathbf{x}), n_y(\mathbf{x})]^T$ denotes as the unit normal vector at \mathbf{x} , and

$\mathbf{T}^j = [T_x^j, T_y^j]^T$ as the traction vector. Then we obtain from Eqs. (6.1.7) to (6.1.11),

$$\begin{aligned} T_x^j(\mathbf{x}) = & \left((\lambda^j + 2\mu^j) \frac{\partial \tilde{\varphi}(\mathbf{x})}{\partial x} n_x(\mathbf{x}) + \mu^j \frac{\partial \tilde{\varphi}(\mathbf{x})}{\partial y} n_y(\mathbf{x}) \right) \tilde{\mathbf{u}}_x \\ & + \left(\lambda^j \frac{\partial \tilde{\varphi}(\mathbf{x})}{\partial y} n_x(\mathbf{x}) + \mu^j \frac{\partial \tilde{\varphi}(\mathbf{x})}{\partial x} n_y(\mathbf{x}) \right) \tilde{\mathbf{u}}_y, \end{aligned} \quad (6.1.12)$$

$$\begin{aligned} T_y^j(\mathbf{x}) = & \left(\lambda^j \frac{\partial \tilde{\varphi}(\mathbf{x})}{\partial x} n_y(\mathbf{x}) + \mu^j \frac{\partial \tilde{\varphi}(\mathbf{x})}{\partial y} n_x(\mathbf{x}) \right) \tilde{\mathbf{u}}_x \\ & + \left((\lambda^j + 2\mu^j) \frac{\partial \tilde{\varphi}(\mathbf{x})}{\partial y} n_y(\mathbf{x}) + \mu^j \frac{\partial \tilde{\varphi}(\mathbf{x})}{\partial x} n_x(\mathbf{x}) \right) \tilde{\mathbf{u}}_y, \end{aligned} \quad (6.1.13)$$

For the simplicity further we define

$$\mathbf{O}^j(\mathbf{x}) = (\lambda_j + 2\mu_j) \frac{\partial \tilde{\varphi}(\mathbf{x})}{\partial x} n_x(\mathbf{x}) + \mu_j \frac{\partial \tilde{\varphi}(\mathbf{x})}{\partial y} n_y(\mathbf{x}), \quad (6.1.14)$$

$$\mathbf{Q}^j(\mathbf{x}) = \lambda_j \frac{\partial \tilde{\varphi}(\mathbf{x})}{\partial y} n_x(\mathbf{x}) + \mu_j \frac{\partial \tilde{\varphi}(\mathbf{x})}{\partial x} n_y(\mathbf{x}), \quad (6.1.15)$$

$$\mathbf{S}^j(\mathbf{x}) = \lambda_j \frac{\partial \tilde{\varphi}(\mathbf{x})}{\partial x} n_y(\mathbf{x}) + \mu_j \frac{\partial \tilde{\varphi}(\mathbf{x})}{\partial y} n_x(\mathbf{x}), \quad (6.1.16)$$

$$\mathbf{R}^j(\mathbf{x}) = (\lambda_j + 2\mu_j) \frac{\partial \tilde{\varphi}(\mathbf{x})}{\partial y} n_y(\mathbf{x}) + \mu_j \frac{\partial \tilde{\varphi}(\mathbf{x})}{\partial x} n_x(\mathbf{x}). \quad (6.1.17)$$

Then Eqs. (6.1.10) and (6.1.11) can be expressed as

$$T_x^j(\mathbf{x}) = \mathbf{O}^j(\mathbf{x}) \tilde{\mathbf{u}}_x^j + \mathbf{Q}^j(\mathbf{x}) \tilde{\mathbf{u}}_y^j, \quad \mathbf{x} \in D_j, \quad (6.1.18)$$

$$T_y^j(\mathbf{x}) = \mathbf{S}^j(\mathbf{x}) \tilde{\mathbf{u}}_x^j + \mathbf{R}^j(\mathbf{x}) \tilde{\mathbf{u}}_y^j, \quad \mathbf{x} \in D_j. \quad (6.1.19)$$

Thus, Eq. (2.3.4) can be written as

$$\mathbf{O}^1(\mathbf{x}) \tilde{\mathbf{u}}_x^1 + \mathbf{Q}^1(\mathbf{x}) \tilde{\mathbf{u}}_y^1 = \mathbf{O}^0(\mathbf{x}) \tilde{\mathbf{u}}_x^0 + \mathbf{Q}^0(\mathbf{x}) \tilde{\mathbf{u}}_y^0, \quad (6.1.20)$$

$$\mathbf{S}^1(\mathbf{x}) \tilde{\mathbf{u}}_x^1 + \mathbf{R}^1(\mathbf{x}) \tilde{\mathbf{u}}_y^1 = \mathbf{S}^0(\mathbf{x}) \tilde{\mathbf{u}}_x^0 + \mathbf{R}^0(\mathbf{x}) \tilde{\mathbf{u}}_y^0. \quad (6.1.21)$$

6.1.3 Discretized periodic boundary conditions of square lattice

For the square lattice, as shown in Fig. 5.1, the periodical boundary conditions (2.3.5) and (2.3.6) can be expressed as

$$\begin{aligned} u_x(\mathbf{x}_{\Gamma_1}) &= u_x(\mathbf{x}_{\Gamma_3})e^{-ik_x a}, & u_y(\mathbf{x}_{\Gamma_1}) &= u_y(\mathbf{x}_{\Gamma_3})e^{-ik_x a}, \\ u_x(\mathbf{x}_{\Gamma_2}) &= u_x(\mathbf{x}_{\Gamma_4})e^{-ik_y a}, & u_y(\mathbf{x}_{\Gamma_2}) &= u_y(\mathbf{x}_{\Gamma_4})e^{-ik_y a}, \end{aligned} \quad (6.1.22)$$

$$\begin{aligned} T_x(\mathbf{x}_{\Gamma_1}) &= T_x(\mathbf{x}_{\Gamma_3})e^{-ik_x a}, & T_y(\mathbf{x}_{\Gamma_1}) &= T_y(\mathbf{x}_{\Gamma_3})e^{-ik_x a}, \\ T_x(\mathbf{x}_{\Gamma_2}) &= T_x(\mathbf{x}_{\Gamma_4})e^{-ik_y a}, & T_y(\mathbf{x}_{\Gamma_2}) &= T_y(\mathbf{x}_{\Gamma_4})e^{-ik_y a}, \end{aligned} \quad (6.1.23)$$

where $\mathbf{x}_{\Gamma_i} \in \Gamma_i$ ($i=1,2,3,4$), $T_x(\mathbf{x})$ and $T_y(\mathbf{x})$ are the tractions. Eq. (6.1.22) can be changed to

$$\begin{aligned} \tilde{\mathbf{u}}_x|_{\Gamma_1} &= \tilde{\mathbf{u}}_x|_{\Gamma_3} e^{-ik_x a}, & \tilde{\mathbf{u}}_y|_{\Gamma_1} &= \tilde{\mathbf{u}}_y|_{\Gamma_3} e^{-ik_x a}, \\ \tilde{\mathbf{u}}_x|_{\Gamma_2} &= \tilde{\mathbf{u}}_x|_{\Gamma_4} e^{-ik_y a}, & \tilde{\mathbf{u}}_y|_{\Gamma_2} &= \tilde{\mathbf{u}}_y|_{\Gamma_4} e^{-ik_y a}, \end{aligned} \quad (6.1.24)$$

$\tilde{\mathbf{u}}_x|_{\Gamma_i}$ and $\tilde{\mathbf{u}}_y|_{\Gamma_i}$ denote the elements of the vectors $\tilde{\mathbf{u}}_x$ and $\tilde{\mathbf{u}}_y$ corresponding to the unit-cell boundary $\mathbf{x} \in \Gamma_i$, and are analytically considered by modifying the RBF matrix which will be discussed later. The traction vector in Eq. (6.1.23) can be expressed as

$$\left(\mathbf{O}(\mathbf{x}_{\Gamma_1}) - \mathbf{O}(\mathbf{x}_{\Gamma_3})e^{-ik_x a}\right)\tilde{\mathbf{u}}_x^0 + \left(\mathbf{Q}(\mathbf{x}_{\Gamma_1}) - \mathbf{Q}(\mathbf{x}_{\Gamma_3})e^{-ik_x a}\right)\tilde{\mathbf{u}}_y^0 = 0, \quad (6.1.25)$$

$$\left(\mathbf{S}(\mathbf{x}_{\Gamma_1}) - \mathbf{S}(\mathbf{x}_{\Gamma_3})e^{-ik_x a}\right)\tilde{\mathbf{u}}_x^0 + \left(\mathbf{R}(\mathbf{x}_{\Gamma_1}) - \mathbf{R}(\mathbf{x}_{\Gamma_3})e^{-ik_x a}\right)\tilde{\mathbf{u}}_y^0 = 0, \quad (6.1.26)$$

$$\left(\mathbf{O}(\mathbf{x}_{\Gamma_2}) - \mathbf{O}(\mathbf{x}_{\Gamma_4})e^{-ik_y a}\right)\tilde{\mathbf{u}}_x^0 + \left(\mathbf{Q}(\mathbf{x}_{\Gamma_2}) - \mathbf{Q}(\mathbf{x}_{\Gamma_4})e^{-ik_y a}\right)\tilde{\mathbf{u}}_y^0 = 0, \quad (6.1.27)$$

$$\left(\mathbf{S}(\mathbf{x}_{\Gamma_2}) - \mathbf{S}(\mathbf{x}_{\Gamma_4})e^{-ik_y a}\right)\tilde{\mathbf{u}}_x^0 + \left(\mathbf{R}(\mathbf{x}_{\Gamma_2}) - \mathbf{R}(\mathbf{x}_{\Gamma_4})e^{-ik_y a}\right)\tilde{\mathbf{u}}_y^0 = 0. \quad (6.1.28)$$

By considering the governing equations (6.1.4) and (6.1.5), the traction equilibrium condition (2.3.4) on the matrix-scatterer's interface, and the traction periodicity conditions (6.1.25)-(6.1.28), a generalized eigenvalue equation is formed as

$$\mathbf{A}\mathbf{U} = -\omega^2 \mathbf{H}\mathbf{U}, \quad (6.1.29)$$

where \mathbf{A} is the RBF matrix, \mathbf{H} is the matrix related to the property of the constituent materials, and \mathbf{U} is the vector of the displacements. The displacement periodicity conditions (6.1.24) and the displacement continuity conditions (6.1.6) on the matrix-scatterer's interface are considered by modifying the RBF matrix \mathbf{A} and \mathbf{H} . The details of the matrices \mathbf{A} and \mathbf{H} for different lattice forms are given in the following

$$\mathbf{U} = [\tilde{\mathbf{u}}_x^0, \tilde{\mathbf{u}}_y^0, \tilde{\mathbf{u}}_x^1, \tilde{\mathbf{u}}_y^1]^T, \quad (6.1.30)$$

$$\mathbf{A} = \begin{bmatrix} \mathbf{G}^0(\mathbf{x}_0) & \mathbf{\Psi}^0(\mathbf{x}_0) & \mathbf{0} & \mathbf{0} \\ \mathbf{\Psi}^0(\mathbf{x}_0) & \mathbf{\Phi}^0(\mathbf{x}_0) & \mathbf{0} & \mathbf{0} \\ \mathbf{0} & \mathbf{0} & \mathbf{G}^1(\mathbf{x}_1) & \mathbf{\Psi}^1(\mathbf{x}_1) \\ \mathbf{0} & \mathbf{0} & \mathbf{\Psi}^1(\mathbf{x}_1) & \mathbf{\Phi}^1(\mathbf{x}_1) \\ \mathbf{S}^0(\mathbf{x}_{\Gamma_0}) & \mathbf{R}^0(\mathbf{x}_{\Gamma_0}) & \mathbf{S}^1(\mathbf{x}_{\Gamma_0}) & \mathbf{R}^1(\mathbf{x}_{\Gamma_0}) \\ \mathbf{O}^0(\mathbf{x}_{\Gamma_0}) & \mathbf{Q}^0(\mathbf{x}_{\Gamma_0}) & \mathbf{O}^1(\mathbf{x}_{\Gamma_0}) & \mathbf{Q}^1(\mathbf{x}_{\Gamma_0}) \\ \mathbf{S}^0(\mathbf{x}_{\Gamma_1}) + \mathbf{S}^0(\mathbf{x}_{\Gamma_3})e^{-ik_x a} & \mathbf{R}^0(\mathbf{x}_{\Gamma_1}) + \mathbf{R}^0(\mathbf{x}_{\Gamma_3})e^{-ik_x a} & \mathbf{0} & \mathbf{0} \\ \mathbf{O}^0(\mathbf{x}_{\Gamma_1}) + \mathbf{O}^0(\mathbf{x}_{\Gamma_3})e^{-ik_x a} & \mathbf{Q}^0(\mathbf{x}_{\Gamma_1}) + \mathbf{Q}^0(\mathbf{x}_{\Gamma_3})e^{-ik_x a} & \mathbf{0} & \mathbf{0} \\ \mathbf{S}^0(\mathbf{x}_{\Gamma_2}) + \mathbf{S}^0(\mathbf{x}_{\Gamma_4})e^{-ik_y a} & \mathbf{R}^0(\mathbf{x}_{\Gamma_2}) + \mathbf{R}^0(\mathbf{x}_{\Gamma_4})e^{-ik_y a} & \mathbf{0} & \mathbf{0} \\ \mathbf{O}^0(\mathbf{x}_{\Gamma_2}) + \mathbf{O}^0(\mathbf{x}_{\Gamma_4})e^{-ik_y a} & \mathbf{Q}^0(\mathbf{x}_{\Gamma_2}) + \mathbf{Q}^0(\mathbf{x}_{\Gamma_4})e^{-ik_y a} & \mathbf{0} & \mathbf{0} \end{bmatrix}, \quad (6.1.31)$$

$$\mathbf{H} = \begin{bmatrix} \boldsymbol{\rho}^0(\mathbf{x}_0) & \mathbf{0} & \mathbf{0} & \mathbf{0} \\ \mathbf{0} & \boldsymbol{\rho}^0(\mathbf{x}_0) & \mathbf{0} & \mathbf{0} \\ \mathbf{0} & \mathbf{0} & \boldsymbol{\rho}^1(\mathbf{x}_1) & \mathbf{0} \\ \mathbf{0} & \mathbf{0} & \mathbf{0} & \boldsymbol{\rho}^1(\mathbf{x}_1) \\ \mathbf{0} & \mathbf{0} & \mathbf{0} & \mathbf{0} \end{bmatrix}, \quad (6.1.32)$$

where, $\mathbf{x}_0 \in D_0$, $\mathbf{x}_1 \in D_1$, \mathbf{H} is a sparse matrix which has the same size as \mathbf{A} , and $\boldsymbol{\rho}^j(\mathbf{x}) = [\delta_{xx_n} \rho^j(\mathbf{x})]$ is a sparse matrix related to the mass density, where δ_{xx_n} is the Dirac delta. Also, \mathbf{A} is a sparse RBF matrix related to \mathbf{x} and \mathbf{x}_n , which can also be written as

$$\mathbf{A} = \mathbf{A}_x, \quad (6.1.33)$$

where \mathbf{x} indicates the columns inside the matrix \mathbf{A} . After the displacement periodicity boundary conditions (6.1.24) and the displacement continuity conditions

(6.1.6) are employed, the displacement vectors $\mathbf{u}^1(\mathbf{x}_{\Gamma_0})$, $\mathbf{u}(\mathbf{x}_{\Gamma_3})$ and $\mathbf{u}(\mathbf{x}_{\Gamma_4})$ can be eliminated by using $\mathbf{u}^0(\mathbf{x}_{\Gamma_0})$, $\mathbf{u}(\mathbf{x}_{\Gamma_1})$ and $\mathbf{u}(\mathbf{x}_{\Gamma_2})$ in Eq. (6.1.29), which results in the following reduced matrix

$$\tilde{\mathbf{A}} = \left[\mathbf{A}^0, \mathbf{A}^1, \mathbf{A}_{\Gamma_1} + \mathbf{A}_{\Gamma_3} e^{ik_x a}, \mathbf{A}_{\Gamma_2} + \mathbf{A}_{\Gamma_4} e^{ik_y a}, \mathbf{A}_{\Gamma_0}^0 + \mathbf{A}_{\Gamma_0}^1 \right]. \quad (6.1.34)$$

In Eq. (6.1.34), the columns inside the matrix \mathbf{A} related to $\Gamma_0 \cup D_1$, Γ_3 and Γ_4 are rearranged by adding them to the columns related to $\Gamma_0 \cup D_0$, Γ_1 and Γ_2 . The size of the matrix \mathbf{A} is reduced, the elements in the columns related to $\Gamma_0 \cup D_1$, Γ_3 and Γ_4 are no longer necessary, and thus a reduced generalized eigenvalue equation is obtained as

$$\tilde{\mathbf{A}}\tilde{\mathbf{U}} = -\omega^2 \tilde{\mathbf{H}}\tilde{\mathbf{U}}, \quad (6.1.35)$$

where $\tilde{\mathbf{H}}$ is a sparse matrix with the same size as $\tilde{\mathbf{A}}$, the matrix size of $\tilde{\mathbf{A}}$ is $2N_1 \times 2N_1$ compared with $2N_1 \times 2N_a$ of \mathbf{A} , N_1 is number of the nodes on D_0 , D_1 , Γ_0 , Γ_1 and Γ_2 , N_a is total node number on D_0 , D_1 , Γ_0 , and Γ_i ($i=1,2,3,4$), and $\tilde{\mathbf{U}}$ is the displacement vector with nodes only located in $D_0 \cup D_1 \cup \Gamma_0 \cup \Gamma_1 \cup \Gamma_2$. Since the columns related to $\mathbf{x}_{\Gamma_0}^0$, $\mathbf{x}_{\Gamma_0}^1$ and \mathbf{x}_{Γ_i} ($i=1,2,3,4$) inside \mathbf{H} are all zero, $\tilde{\mathbf{H}}$ and $\tilde{\mathbf{U}}$ can be written as

$$\tilde{\mathbf{H}} = \left[\mathbf{H}^0, \mathbf{H}^1, \mathbf{H}_{\Gamma_1}, \mathbf{H}_{\Gamma_2}, \mathbf{H}_{\Gamma_0}^0 \right], \quad (6.1.36)$$

$$\tilde{\mathbf{U}} = \left[\mathbf{U}(\mathbf{x}_0), \mathbf{U}(\mathbf{x}_1), \mathbf{U}(\mathbf{x}_{\Gamma_1}), \mathbf{U}(\mathbf{x}_{\Gamma_2}), \mathbf{U}(\mathbf{x}_{\Gamma_0}) \right]^T, \quad (6.1.37)$$

where $\mathbf{U}(\mathbf{x}) = [\tilde{\mathbf{u}}_x(\mathbf{x}), \tilde{\mathbf{u}}_y(\mathbf{x})]^T$, \mathbf{H}_x indicates the columns inside the matrix \mathbf{H} related to \mathbf{x} , the matrix size of $\tilde{\mathbf{H}}$ is $2N_1 \times 2N_1$ while the size of \mathbf{H} is $2N_1 \times 2N_a$.

6.1.4 Discretized periodic boundary conditions of triangular lattice

For the triangular lattice, as shown in Fig. 5.2, the periodical boundary conditions (2.3.5) and (2.3.6) can be expressed as

$$\begin{aligned}
u_x(\mathbf{x}_{\Gamma_1}) &= u_x(\mathbf{x}_{\Gamma_4}) e^{-i\left(k_x \frac{\sqrt{3}}{2} a + k_y \frac{a}{2}\right)}, & u_y(\mathbf{x}_{\Gamma_1}) &= u_y(\mathbf{x}_{\Gamma_4}) e^{-i\left(k_x \frac{\sqrt{3}}{2} a + k_y \frac{a}{2}\right)}, \\
u_x(\mathbf{x}_{\Gamma_2}) &= u_x(\mathbf{x}_{\Gamma_5}) e^{-ik_y a}, & u_y(\mathbf{x}_{\Gamma_2}) &= u_y(\mathbf{x}_{\Gamma_5}) e^{-ik_y a}, \\
u_x(\mathbf{x}_{\Gamma_3}) &= u_x(\mathbf{x}_{\Gamma_6}) e^{-i\left(-k_x \frac{\sqrt{3}}{2} a + k_y \frac{a}{2}\right)}, & u_y(\mathbf{x}_{\Gamma_3}) &= u_y(\mathbf{x}_{\Gamma_6}) e^{-i\left(-k_x \frac{\sqrt{3}}{2} a + k_y \frac{a}{2}\right)},
\end{aligned} \tag{6.1.38}$$

$$\begin{aligned}
T_x(\mathbf{x}_{\Gamma_1}) &= T_x(\mathbf{x}_{\Gamma_4}) e^{-i\left(k_x \frac{\sqrt{3}}{2} a + k_y \frac{a}{2}\right)}, & T_y(\mathbf{x}_{\Gamma_1}) &= T_y(\mathbf{x}_{\Gamma_4}) e^{-i\left(k_x \frac{\sqrt{3}}{2} a + k_y \frac{a}{2}\right)}, \\
T_x(\mathbf{x}_{\Gamma_2}) &= T_x(\mathbf{x}_{\Gamma_5}) e^{-ik_y a}, & T_y(\mathbf{x}_{\Gamma_2}) &= T_y(\mathbf{x}_{\Gamma_5}) e^{-ik_y a}, \\
T_x(\mathbf{x}_{\Gamma_3}) &= T_x(\mathbf{x}_{\Gamma_6}) e^{-i\left(-k_x \frac{\sqrt{3}}{2} a + k_y \frac{a}{2}\right)}, & T_y(\mathbf{x}_{\Gamma_3}) &= T_y(\mathbf{x}_{\Gamma_6}) e^{-i\left(-k_x \frac{\sqrt{3}}{2} a + k_y \frac{a}{2}\right)}.
\end{aligned} \tag{6.1.39}$$

The matrices \mathbf{A} and \mathbf{H} as well as the vector \mathbf{U} in Eq. (6.1.29) are given by

$$\mathbf{A} = \begin{pmatrix} \mathbf{G}^0(\mathbf{x}_0) & \mathbf{\Psi}^0(\mathbf{x}_0) & \mathbf{0} & \mathbf{0} \\ \mathbf{\Psi}^0(\mathbf{x}_0) & \mathbf{\Phi}^0(\mathbf{x}_0) & \mathbf{0} & \mathbf{0} \\ \mathbf{0} & \mathbf{0} & \mathbf{G}^1(\mathbf{x}_1) & \mathbf{\Psi}^1(\mathbf{x}_1) \\ \mathbf{0} & \mathbf{0} & \mathbf{\Psi}^1(\mathbf{x}_1) & \mathbf{\Phi}^1(\mathbf{x}_1) \\ \mathbf{S}^0(\mathbf{x}_{\Gamma_0}) & \mathbf{R}^0(\mathbf{x}_{\Gamma_0}) & \mathbf{S}^1(\mathbf{x}_{\Gamma_0}) & \mathbf{R}^1(\mathbf{x}_{\Gamma_0}) \\ \mathbf{O}^0(\mathbf{x}_{\Gamma_0}) & \mathbf{Q}^0(\mathbf{x}_{\Gamma_0}) & \mathbf{O}^1(\mathbf{x}_{\Gamma_0}) & \mathbf{Q}^1(\mathbf{x}_{\Gamma_0}) \\ \mathbf{S}^0(\mathbf{x}_{\Gamma_1}) + \mathbf{S}^0(\mathbf{x}_{\Gamma_4}) e_{1-4} & \mathbf{R}^0(\mathbf{x}_{\Gamma_1}) + \mathbf{R}^0(\mathbf{x}_{\Gamma_4}) e_{1-4} & \mathbf{0} & \mathbf{0} \\ \mathbf{O}^0(\mathbf{x}_{\Gamma_1}) + \mathbf{O}^0(\mathbf{x}_{\Gamma_4}) e_{1-4} & \mathbf{Q}^0(\mathbf{x}_{\Gamma_1}) + \mathbf{Q}^0(\mathbf{x}_{\Gamma_4}) e_{1-4} & \mathbf{0} & \mathbf{0} \\ \mathbf{S}^0(\mathbf{x}_{\Gamma_2}) + \mathbf{S}^0(\mathbf{x}_{\Gamma_5}) e^{-ik_y a} & \mathbf{R}^0(\mathbf{x}_{\Gamma_2}) + \mathbf{R}^0(\mathbf{x}_{\Gamma_5}) e^{-ik_y a} & \mathbf{0} & \mathbf{0} \\ \mathbf{O}^0(\mathbf{x}_{\Gamma_2}) + \mathbf{O}^0(\mathbf{x}_{\Gamma_5}) e^{-ik_y a} & \mathbf{Q}^0(\mathbf{x}_{\Gamma_2}) + \mathbf{Q}^0(\mathbf{x}_{\Gamma_5}) e^{-ik_y a} & \mathbf{0} & \mathbf{0} \\ \mathbf{S}^0(\mathbf{x}_{\Gamma_3}) + \mathbf{S}^0(\mathbf{x}_{\Gamma_6}) e_{3-6} & \mathbf{R}^0(\mathbf{x}_{\Gamma_3}) + \mathbf{R}^0(\mathbf{x}_{\Gamma_6}) e_{3-6} & \mathbf{0} & \mathbf{0} \\ \mathbf{O}^0(\mathbf{x}_{\Gamma_3}) + \mathbf{O}^0(\mathbf{x}_{\Gamma_6}) e_{3-6} & \mathbf{Q}^0(\mathbf{x}_{\Gamma_3}) + \mathbf{Q}^0(\mathbf{x}_{\Gamma_6}) e_{3-6} & \mathbf{0} & \mathbf{0} \end{pmatrix}, \tag{6.1.40}$$

$$\mathbf{H} = \begin{pmatrix} \boldsymbol{\rho}^0(\mathbf{x}_0) & \mathbf{0} & \mathbf{0} & \mathbf{0} \\ \mathbf{0} & \boldsymbol{\rho}^0(\mathbf{x}_0) & \mathbf{0} & \mathbf{0} \\ \mathbf{0} & \mathbf{0} & \boldsymbol{\rho}^1(\mathbf{x}_1) & \mathbf{0} \\ \mathbf{0} & \mathbf{0} & \mathbf{0} & \boldsymbol{\rho}^1(\mathbf{x}_1) \\ \mathbf{0} & \mathbf{0} & \mathbf{0} & \mathbf{0} \end{pmatrix}, \tag{6.1.41}$$

$$\mathbf{U} = [\tilde{\mathbf{u}}_x^0, \tilde{\mathbf{u}}_y^0, \tilde{\mathbf{u}}_x^1, \tilde{\mathbf{u}}_y^1]^T, \tag{6.1.42}$$

where the sparse matrix \mathbf{H} has the same size as \mathbf{A} , and

$$e_{1-4} = e^{-i\left(k_x \frac{\sqrt{3}}{2} a + k_y \frac{a}{2}\right)}, \quad e_{3-6} = e^{-i\left(-k_x \frac{\sqrt{3}}{2} a + k_y \frac{a}{2}\right)}.$$

As for the square lattice, the displacement periodicity boundary conditions (2.3.5)

and the displacement continuity conditions (2.3.3) are employed to obtain a reduced matrix $\tilde{\mathbf{A}}$ for the triangular lattice as

$$\tilde{\mathbf{A}} = \left[\mathbf{A}_0, \mathbf{A}_1, \mathbf{A}_{\Gamma_1} + \mathbf{A}_{\Gamma_4} e_{1-4}, \mathbf{A}_{\Gamma_2} + \mathbf{A}_{\Gamma_5} e^{ik_y a}, \mathbf{A}_{\Gamma_3} + \mathbf{A}_{\Gamma_6} e_{3-6}, \mathbf{A}_{\Gamma_0}^0 + \mathbf{A}_{\Gamma_0}^1 \right]. \quad (6.1.43)$$

Then a reduced eigenvalue equation as (6.1.35) is formed. Here, the matrix size of $\tilde{\mathbf{A}}$ is $2N_1 \times 2N_1$ compared with $2N_1 \times 2N_a$ of \mathbf{A} , N_1 is number of the nodes located on D_0 , D_1 , Γ_0 , and Γ_i , ($i=1, 2, 3$), N_a is total nodes number in D_0 , D_1 , Γ_0 , and Γ_i , $i=1, 2, \dots, 6$. Since the columns related to Γ_0 and Γ_i ($i=1, 2, \dots, 6$) inside \mathbf{H} are all zero, $\tilde{\mathbf{H}}$ and $\tilde{\mathbf{U}}$ can be written as

$$\tilde{\mathbf{H}} = \left[\mathbf{H}_0, \mathbf{H}_1, \mathbf{H}_{\Gamma_1}, \mathbf{H}_{\Gamma_2}, \mathbf{H}_{\Gamma_3}, \mathbf{H}_{\Gamma_0}^0 \right], \quad (6.1.44)$$

$$\tilde{\mathbf{U}} = \left[\mathbf{U}(\mathbf{x}_0), \mathbf{U}(\mathbf{x}_1), \mathbf{U}(\mathbf{x}_{\Gamma_1}), \mathbf{U}(\mathbf{x}_{\Gamma_2}), \mathbf{U}(\mathbf{x}_{\Gamma_3}), \mathbf{U}(\mathbf{x}_{\Gamma_0}) \right]^T, \quad (6.1.45)$$

where $\mathbf{U}(\mathbf{x}) = [\tilde{\mathbf{u}}_x(\mathbf{x}), \tilde{\mathbf{u}}_y(\mathbf{x})]^T$, \mathbf{H}_x represents the columns related to x inside \mathbf{H} , the matrix size of \mathbf{H} is the same as $\tilde{\mathbf{A}}$ here. To solve the generalized eigenvalue equation (6.1.35) numerically for both the square and the triangular lattices, the eigenvalue solver implemented in MATLAB is applied.

6.2 Numerical results and discussions

In this section, numerical results obtained by the LRBFCM are presented and discussed. As it was found in last chapter that a uniform node distribution has a better convergence rate than a random distribution of equal size, a uniform node distribution is used for all numerical calculations.

Two different lattice forms and three different shapes of the scatterers are considered. For the aurum (Au) scatterers embedded in the epoxy matrix, the parameters of the component materials are given by:

$$\rho^1 = 19500 \text{ kg} / \text{m}^3, \quad \lambda^1 = 4.23 \times 10^{10} \text{ N} / \text{m}^2, \quad \mu^1 = 2.99 \times 10^{10} \text{ N} / \text{m}^2,$$

$$\rho^0 = 1180 \text{ kg} / \text{m}^3, \quad \lambda^0 = 4.43 \times 10^9 \text{ N} / \text{m}^2, \quad \mu^1 = 1.59 \times 10^9 \text{ N} / \text{m}^2.$$

In this case, the acoustic impedance ratio of the considered phononic crystal is $Z = \rho^1 c_1 / \rho^0 c_0 = 17.64$, where $c_j = \sqrt{\mu^j / \rho^j}$ is the transverse wave speed. For the aluminium (Al) scatterers embedded in the epoxy matrix, the parameters of the component materials are:

$$\rho^1 = 2730 \text{ kg} / \text{m}^3, \quad \lambda^1 = 4.59 \times 10^{10} \text{ N} / \text{m}^2, \quad \mu^1 = 2.7 \times 10^{10} \text{ N} / \text{m}^2,$$

$$\rho^0 = 1180 \text{ kg} / \text{m}^3, \quad \lambda^0 = 4.43 \times 10^9 \text{ N} / \text{m}^2, \quad \mu^0 = 1.59 \times 10^9 \text{ N} / \text{m}^2.$$

Here, the acoustic impedance ratio of the considered phononic crystal is $Z = \rho^1 c_1 / \rho^0 c_0 = 6.46$.

6.2.1 Square and rectangular scatterers in square and triangular lattices

Fig. 6.1 shows the node distribution of the phononic crystal in a square lattice with the square scatterers. The filling fraction of the square lattice with the square scatterers is 0.138, the area of the square scatterer is 0.4×0.4 and the unit-cell area is 1×1 . Totally, 21×21 nodes are uniformly distributed in the unit-cell. By using this node distribution, there are always nodes in the x - or y -direction, so we can apply the direct method to treat the traction boundary conditions on the boundary of the unit-cell and the common matrix/scatterer's interface, the shape parameter is chosen as $\xi = 1$ and the number of the local nodes is taken as 9.

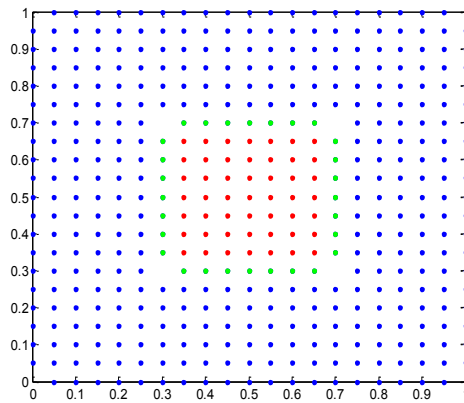


Fig. 6.1 Node distribution in a square lattice with square scatterers.

(Green nodes for interface; Blue nodes for matrix; Red nodes for scatterer)

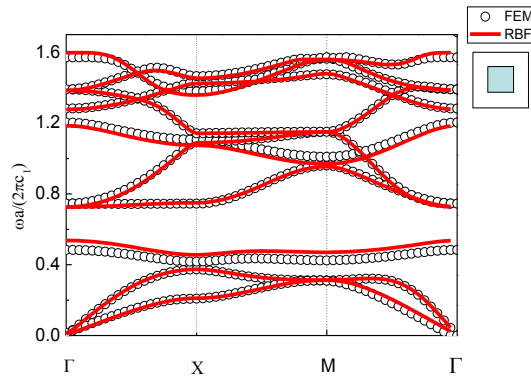


Fig. 6.2 Band structure of the aurum/epoxy phononic crystal in a square lattice with square scatterers.

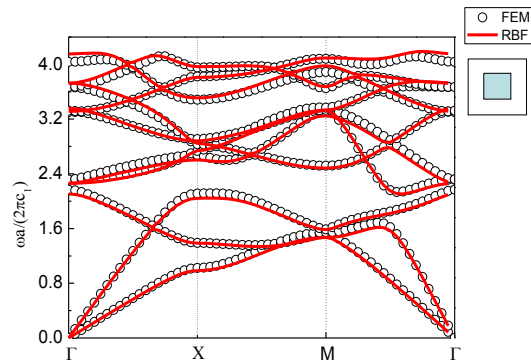


Fig. 6.3 Band structure of the aluminium/epoxy phononic crystal in a square lattice.

Fig. 6.2 and Fig. 6.3 show the band structures of the aurum/epoxy and aluminium/epoxy phononic crystals in a square lattice with square scatterers, where the normalized frequency $\omega a / (2\pi c_1)$ is introduced and $c_1 = \sqrt{\mu^1 / \rho^1}$ is the transverse wave velocity of the scatterer. The results of the LRBFCM represented by the red line are compared with the results of the FEM. Both figures show that the results are fitting quite well, and the change of the materials combination or the acoustic impedance ratio does not affect the results remarkably in the LRBFCM.

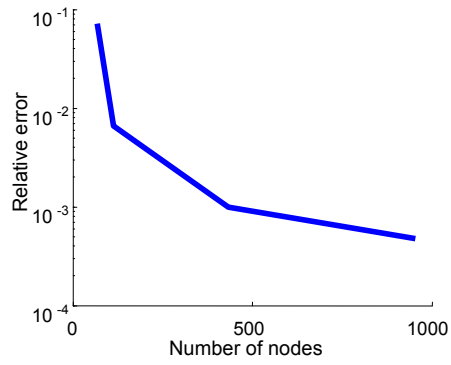


Fig. 6.4 Convergence rate of the aluminium/epoxy phononic crystal in a square lattice with square scatterers.

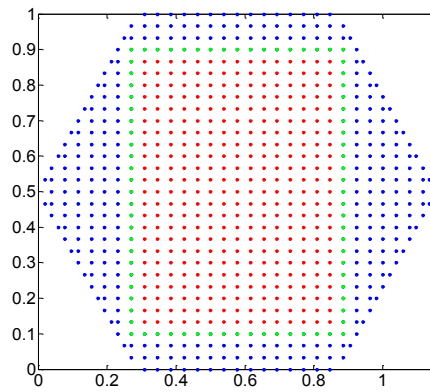


Fig. 6.5 Node distribution of the phononic crystal in a triangular lattice with rectangular scatterers.

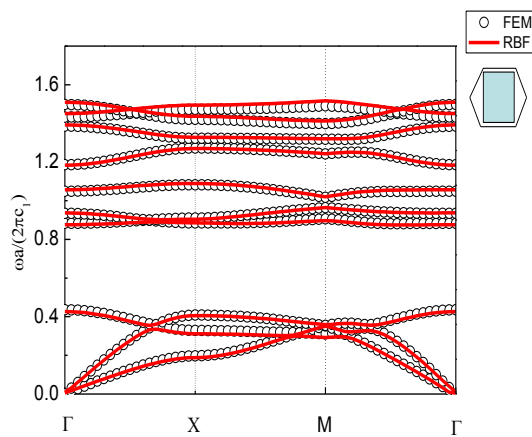


Fig. 6.6 Band structure of the aurum/epoxy phononic crystal in

a triangular lattice with rectangular scatterers.

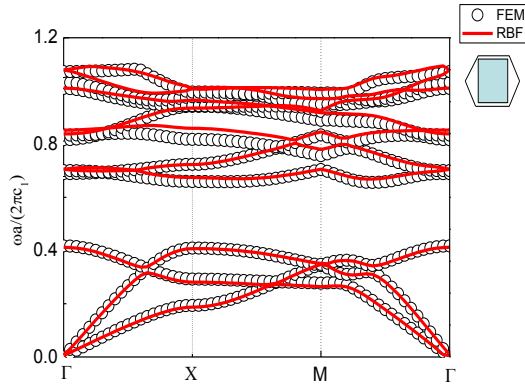


Fig. 6.7 Band structure of the aluminium/epoxy phononic crystal in a triangular lattice with rectangular scatterers.

Fig. 6.4 shows the convergence rate of the average of all eigenvalues which is given in terms of the relative error $(E_r - E_m)/E_r$, where E_r is the result by using 41×41 nodes and E_m is the result by using the current nodes number. From Fig. 6.4, we can see that a number of more than 200 nodes should be used to ensure an acceptable accuracy.

In order to test the present LRBFCM for other lattice forms and filling fractions, a triangular lattice with rectangular scatterers is considered next, as shown in Fig. 6.5. The filling fraction is chosen as 0.5689, totally 731 uniformly distributed nodes are used, $\xi = 1$ is selected and the number of the local nodes is taken as 9. From Fig. 6.5, it is difficult to find sufficient nodes in the direction of the y -axis in some parts of the boundaries of the unit-cell. In this case, the indirect method is hence employed to deal with those nodes for which no sufficient nodes can be found in the y -direction on the boundaries of the unit-cell, and the direct method is employed on the matrix/scatterer's interface. Fig. 6.6 and Fig. 6.7 show the band structures of the aurum/epoxy and aluminium/epoxy phononic crystals with a triangular lattice and rectangular scatterers. In both cases, the present numerical results agree quite well with that obtained by the FEM. This means that the LRBFCM is also suitable for

complicated lattice forms and quite large filling fraction.

6.2.2 Circular scatterers in square and triangular lattices

In the next example, a square lattice with circular scatterers is considered. The filling fraction is 0.196, the radius of the circular scatterers is 0.25, and totally 952 nodes are used as shown in Fig. 6.8. In this work, the indirect method is thus used for nodes on the circular interface.

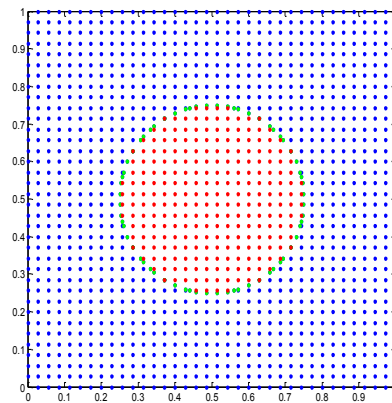


Fig. 6.8 Node distribution of a square lattice with circular scatterers.

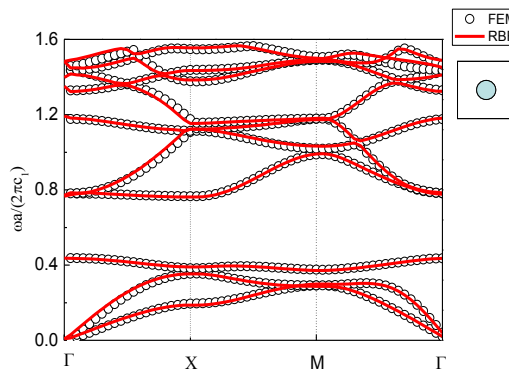


Fig. 6.9 Band structure of the aurum/epoxy phononic crystal in a square lattice with circular scatterers.

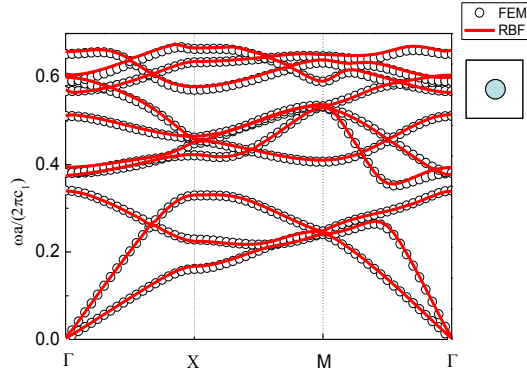


Fig. 6.10 Band structure of the aluminium/epoxy phononic crystal in a square lattice with circular scatterers.

The computed band structures of the aurum/epoxy and aluminium/epoxy phononic crystals are compared with that of the FEM in Fig. 6.9 and Fig. 6.10. Here, the shape parameter is taken as $\xi = 1$ and the number of the local nodes is chosen as 11 due to the node distribution at the circular interface is too close or random distributed. The present numerical results and the FEM results are fitting quite well in general.

In the next case, a triangular lattice with circular scatterers is investigated. The filling fraction of the scatterers is 0.226, the radius of the circular scatterers is 0.25, and totally 785 nodes are used as shown in Fig. 6.11. Here, the indirect method is employed on the boundaries of the unit-cell. The stability of the present LRBFCM is a little reduced compared with that for the square lattice, and more nodes must be employed when the fictitious nodes method for the treatment of the traction equilibrium conditions on the interface is applied. In order to solve this problem the indirect method is employed in this case as described previously for the square lattice with circular scatterers.

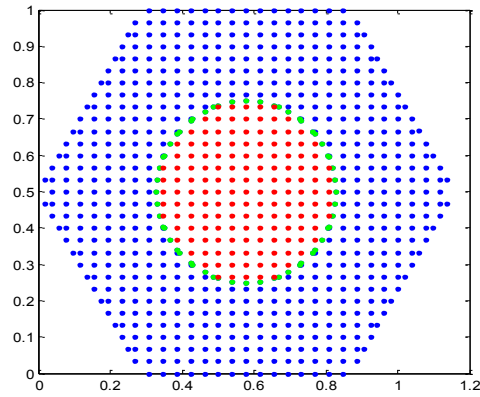


Fig. 6.11 Node distribution of a triangular lattice with circular scatterers.

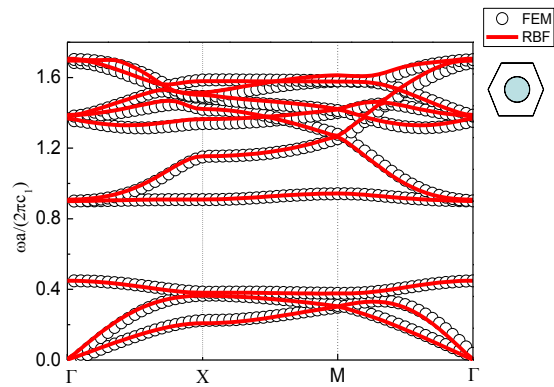


Fig. 6.12 Band structure of the aurum/epoxy phononic crystal in a triangular lattice with circular scatterers.

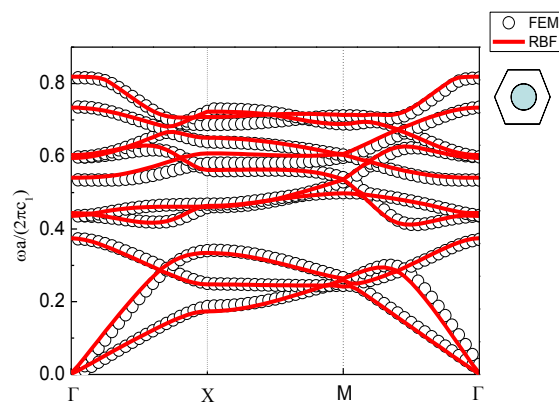


Fig. 6.13 Band structure of the aluminium/epoxy phononic crystal in a triangular lattice with circular scatterers.

The band structures of the aluminium/epoxy and aurum/epoxy phononic crystals

are compared with that obtained by the FEM in Fig. 6.12 and Fig. 6.13. Here, the shape parameter is taken as $\xi = 1$ and the number of the local nodes is chosen as 11. Here again, the present results are fitting quite well with the FEM results in general.

6.2.3 Triangular scatterers in square and triangular lattices

Here, a square lattice with triangular scatterers is analysed. The filling fraction of the scatterers is 0.08, and totally 968 nodes are applied as shown in Fig. 6.14. The shape parameter is chosen as $\xi = 1$, and the number of the local nodes is taken as 9. The indirect method is employed on the interface and the direct method is used on the boundaries of the unit-cell to obtain the results in Fig. 6.15 and Fig. 6.16. Due to the complex form of the triangular scatterer, the numerical results obtained by the present LRBFCM show a little difference from that of the FEM. However, they are still in a good agreement in general.

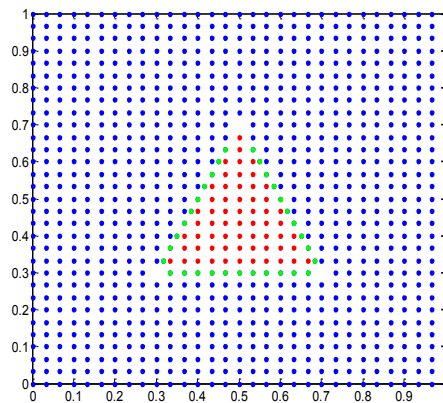


Fig. 6.14 Node distribution of the phononic crystal in a square lattice with triangular scatterers.

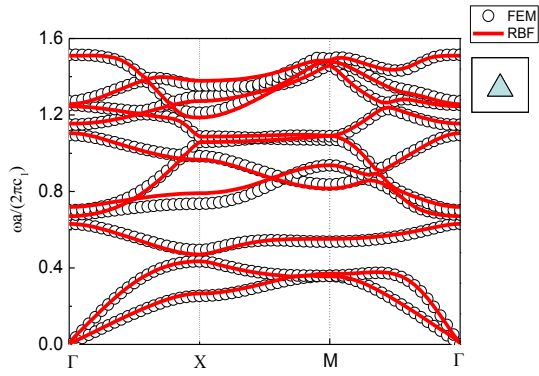


Fig. 6.15 Band structure of the aurum/epoxy phononic crystal in a square lattice with triangular scatterers.

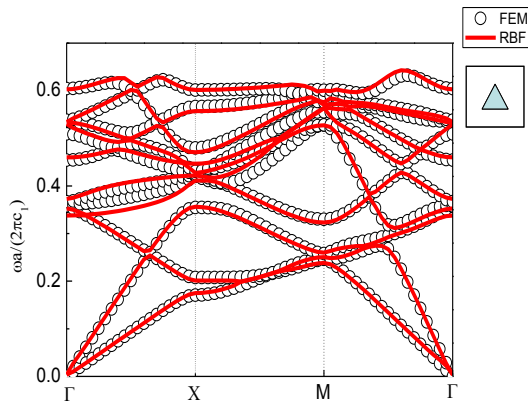


Fig. 6.16 Band structure of the aluminium/epoxy phononic crystal in a square lattice with triangular scatterers.

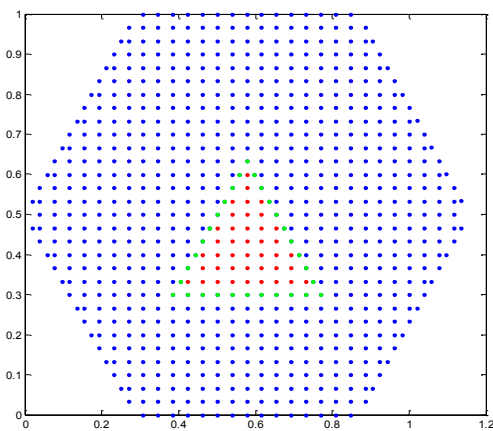


Fig. 6.17 Node distribution of the phononic crystal in a triangular lattice with triangular scatterers.

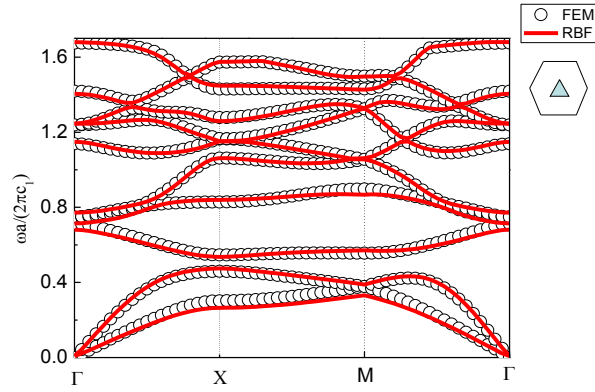


Fig. 6.18 Band structure of the aurum/epoxy phononic crystal in a square lattice with triangular scatterers.

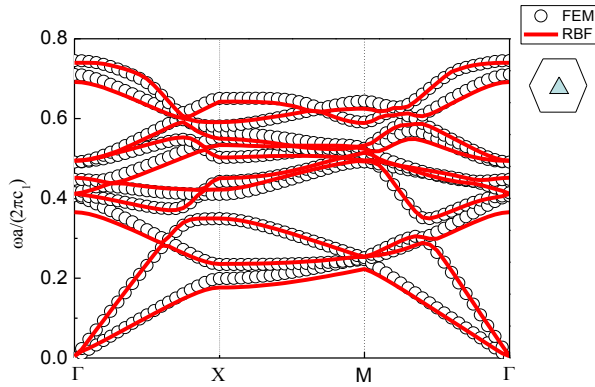


Fig. 6.19 Band structure of the aluminium/epoxy phononic crystal in a square lattice with triangular scatterers.

Finally, we consider a triangular lattice with triangular scatterers as shown in Fig. 6.17. In this case, the filling fraction of the scatterers is 0.0741, and totally 741 nodes are applied as shown in Fig. 20. The shape parameter is chosen as $\xi=1$ and the number of the local nodes is selected as 9. The indirect method is employed on the matrix/scatterer's interface and the direct method is used on the boundaries of the unit-cell to obtain the band structures given in Fig. 6.18 and Fig. 6.19. Here again, the numerical results of the present LRBF-CM are in good agreement with the results of the FEM.

6.3 Analysis of the computational efficiency

In order to show the computational efficiency and accuracy of the present LRBFCM, the required computing time and the accuracy for the previously presented numerical examples are summarized in Tables 6.1-6.4 and compared with that of the FEM. Here, the numerical error is defined as

$$\text{Error} = \frac{\sum (E_f - E_r)}{\sum E_f},$$

where E_f is the result of the FEM by using COMSOL Multiphysics and E_r is the result of the present LRBFCM. All the computations are carried out on the same laptop with Intel(R) Core(TM) i7-4510U, 2.00 GHz CPU and 8 GB RAM.

For the aluminium/epoxy and aurum/epoxy phononic crystals with a square lattice, the results are respectively listed in the Table 6.1 and Table 6.2. In general, we can find that the computational errors in the case of a square lattice do not vary remarkably with the change of the material combinations or acoustic impedance ratios. Even with a smaller number of the degrees of freedom, the present LRBFCM can still lead to sufficiently accurate results compared to the FEM. For the square lattice with square scatterers, we can easily find that 433 nodes can already lead to a high accuracy with a saving of the computing time around 87% compared with the FEM. Even though the degrees of freedom in the FEM could also be reduced, however, the meshes in the FEM are rather cumbersome to change as we wish in the COMSOL Multiphysics. For the square lattice with circular scatterers, the computing time saving of the LRBFCM is still more than 33% in comparison to the FEM. For the square lattice with triangular scatterers, the computing time saving of the present LRBFCM is more than 40% compared with the FEM.

Table 6.3 and Table 6.4 show the corresponding results for the Al/epoxy and Au/epoxy phononic crystals with a triangular lattice, respectively. For the triangular lattice with triangular scatterers, the degrees of freedom of the LRBFCM are 1462 and not significantly lower than 1674 in the FEM, but the computing time saving is 60%. The other two cases for circular and triangular scatterers also show that the efficiency

of the LRBFCM is very high in comparison with the FEM.

Lattice form		Square		
Scatterer shape		Square	Circular	Triangular
				
RBF	Number of nodes	433	952	968
	Degrees of freedom	866	1904	1936
	Time needed [s]	21.62	104.86	102.34
FEM	Degrees of freedom	2802	3066	2618
	Time needed [s]	173	177	172
Comparison	Errors	0.0042	0.0054	3.6702x10 ⁻⁴
	Time saving	87.78%	40.75%	40.50%

Table 6.1 Computing time and accuracy comparisons (Al/epoxy).

From Table 6.1 to Table 6.4 in the above discussions we can conclude that the present meshfree LRBFCM is very efficient and quite accurate and exhibits a high convergence rate for band structure calculations of in-plane elastic waves in 2D phononic crystals, which is validated by the corresponding numerical results obtained by the FEM. It is worth to mention here that the used FEM for the purpose of comparison is a commercial and optimized software package, while the present LRBFCM is self-developed. In this sense, the efficiency and the accuracy of the present LRBFCM can be further improved and enhanced.

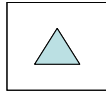
Lattice form		Square		
Scatterer shape		Square	Circular	Triangular
				
RBF	Number of nodes	433	952	968
	Degrees of freedom	866	1904	1936
	Time needed [s]	23.40	111.26	98.14
FEM	Degrees of freedom	2802	3066	2618
	Time needed [s]	173	174	171
Comparison	Errors	0.0014	0.0054	0.0011
	Time saving	86.7%	33.18%	42.69%

Table 6.2 Computing time and accuracy comparisons (Au/epoxy).

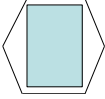
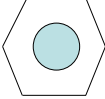
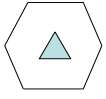
Lattice form		Triangular		
Scatterer shape		Rectangular	Circular	Triangular
				
RBF	Number of nodes	731	785	741
	Degrees of freedom	1462	1570	1482
	Time needed [s]	68.25	75.44	60.26
FEM	Degrees of freedom	1674	2226	1634
	Time needed [s]	172	175	169
Comparison	Errors	0.0025	0.0025	0.0050
	Time saving	60.3%	56.89%	64.34%

Table 6.3 Computing time and accuracy comparisons (Al/epoxy).

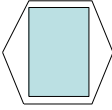
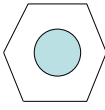
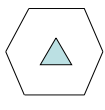
Lattice form		Triangular		
Scatterer shape		Rectangular	Circular	Triangular
				
RBF	Number of nodes	731	785	741
	Degrees of freedom	1462	1570	1482
	Time needed [s]	73.4300	74.06	59.17
FEM	Degrees of freedom	1674	2226	1634
	Time needed [s]	173	175	168
Comparison	Errors	0.0146	0.0021	0.0028
	Time saving	57.5%	57.68%	64.47%

Table 6.4 Computing time and accuracy comparisons (Au/epoxy).

6.4 Summary

In this chapter, the LRBFCEM is extended to the band structure calculations of the in-plane elastic waves in 2D solid/solid phononic crystals. By a proper choice of the shape parameter and the number of the local nodes of the RBFs, the node distributions and the application of the special techniques for the treatments of the boundary conditions proposed in Chapter 3, the LRBFCEM is applied to the band structure computation of the in-plane elastic waves in 2D phononic crystals. For different material combinations or acoustic impedance ratios (small to large), different filling fractions (small to large), different lattice forms (square or triangular) and several scatterer shapes (square, circular and triangular), the accuracy and the efficiency of the present method are validated by comparing the numerical results with that obtained by the FEM. By keeping a comparable numerical accuracy, the present

meshfree RBF collocation method is more efficient than the used FEM. It requires only distributed nodes instead of meshes in contrast to the domain-type discretization methods such as the FEM, which makes the method very attractive. For moving boundary value problems (e.g., propagating cracks, time-dependent phase change or Stefan problem, etc.) and adaptive numerical schemes, this feature could be significantly advantages because the insertion of nodes is much easier than the remeshing procedure required by the conventional FEM. Indeed, the present method has also certain disadvantages. In particular, the method is still relatively sensitive to the choice of the shape parameter, the number of the local nodes involved and the node distributions under complex geometrical circumstances, and it suffers from the stability problem when the normal derivatives of the primary field quantities near the boundaries of the analyzed domain are not handled properly.

Chapter 7

Local RBF-CM for wave propagation analysis in 2D solid/fluid and fluid/solid phononic crystals

In this chapter, the LRBFCM is presented for computing the band structures of the two-dimensional (2D) solid/fluid and fluid/solid phononic crystals. Both systems of solid scatterers embedded in a fluid matrix (solid/fluid phononic crystals) and fluid scatterers embedded in a solid matrix (fluid/solid phononic crystals) are investigated. The general form of LRBFCM for the in-plane elastic waves is given in section 7.1. The numerical results are discussed in section 7.2. Analysis of the computational efficiency are presented in 7.3. Then some remarks are given in the last section 7.4.

7.1 LRBFCM formulation of the eigenvalue problems

In order to solve the governing equations, the displacements along the x - and y -direction in the solid and the pressure of the acoustic wave are given separately in the LRBFCM as follows by using (3.2.11) to (3.2.13),

$$u_y(\mathbf{x}) = \tilde{\boldsymbol{\varphi}}(\mathbf{x})\tilde{\mathbf{u}}_y, \quad u_x(\mathbf{x}) = \tilde{\boldsymbol{\varphi}}(\mathbf{x})\tilde{\mathbf{u}}_x, \quad (7.1.1)$$

$$p(\mathbf{x}) = \tilde{\boldsymbol{\varphi}}(\mathbf{x})\tilde{\mathbf{p}}, \quad (7.1.2)$$

where $\tilde{\mathbf{u}}_y = [u_y(\mathbf{x}_1), u_y(\mathbf{x}_2) \dots u_y(\mathbf{x}_n)]^T$, $\tilde{\mathbf{u}}_x = [u_x(\mathbf{x}_1), u_x(\mathbf{x}_2) \dots u_x(\mathbf{x}_n)]^T$ are the displacements vectors in the solid, $\tilde{\mathbf{p}} = [p(\mathbf{x}_1), p(\mathbf{x}_2) \dots p(\mathbf{x}_n)]^T$ are the pressure vectors of the fluid.

7.1.1 Discretized governing equations

By substituting Eqs. (7.1.1) and (7.1.2) into Eq. (2.4.1), the governing equations of the elastic waves in the solid can be expressed as

$$\begin{aligned} & \left((\lambda + 2\mu) \frac{\partial^2 \tilde{\boldsymbol{\varphi}}(\mathbf{x})}{\partial x^2} + \mu \frac{\partial^2 \tilde{\boldsymbol{\varphi}}(\mathbf{x})}{\partial y^2} \right) \tilde{\mathbf{u}}_x + (\lambda + \mu) \frac{\partial^2 \tilde{\boldsymbol{\varphi}}(\mathbf{x})}{\partial x \partial y} \tilde{\mathbf{u}}_y \\ & = -\rho_s \omega^2 \tilde{\boldsymbol{\varphi}}(\mathbf{x}) \tilde{\mathbf{u}}_x, \end{aligned}$$

$$\begin{aligned} & \left((\lambda + 2\mu) \frac{\partial^2 \tilde{\varphi}(\mathbf{x})}{\partial y^2} + \mu \frac{\partial^2 \tilde{\varphi}(\mathbf{x})}{\partial x^2} \right) \tilde{\mathbf{u}}_y + (\lambda + \mu) \frac{\partial^2 \tilde{\varphi}(\mathbf{x})}{\partial x \partial y} \tilde{\mathbf{u}}_x \\ & = -\rho_s \omega^2 \tilde{\varphi}(\mathbf{x}) \tilde{\mathbf{u}}_y. \end{aligned}$$

For convenience we define

$$\mathbf{G}(\mathbf{x}) = \left((\lambda + 2\mu) \frac{\partial^2}{\partial x^2} + \mu \frac{\partial^2}{\partial y^2} \right) \tilde{\varphi}(\mathbf{x}),$$

$$\Psi(\mathbf{x}) = (\lambda + \mu) \frac{\partial^2 \tilde{\varphi}(\mathbf{x})}{\partial x \partial y},$$

$$\Phi(\mathbf{x}) = \left((\lambda + 2\mu) \frac{\partial^2}{\partial y^2} + \mu \frac{\partial^2}{\partial x^2} \right) \tilde{\varphi}(\mathbf{x}),$$

then the governing equations of the elastic wave in the solid can be expressed as

$$\mathbf{G}(\mathbf{x}) \tilde{\mathbf{u}}_x + \Psi(\mathbf{x}) \tilde{\mathbf{u}}_y = -\rho_s \omega^2 \tilde{\varphi}(\mathbf{x}) \tilde{\mathbf{u}}_x, \quad (7.1.3)$$

$$\Psi(\mathbf{x}) \tilde{\mathbf{u}}_x + \Phi(\mathbf{x}) \tilde{\mathbf{u}}_y = -\rho_s \omega^2 \tilde{\varphi}(\mathbf{x}) \tilde{\mathbf{u}}_y. \quad (7.1.4)$$

The governing equation of pressure waves in the fluid can be expressed as

$$\left(\frac{\partial^2 \tilde{\varphi}(\mathbf{x})}{\partial x^2} + \frac{\partial^2 \tilde{\varphi}(\mathbf{x})}{\partial y^2} \right) \tilde{\mathbf{p}} = -\frac{\rho_f}{K} \omega^2 \tilde{\varphi}(\mathbf{x}) \tilde{\mathbf{p}},$$

for convenience we define

$$\mathbf{M}(\mathbf{x}) = K \left(\frac{\partial^2}{\partial x^2} + \frac{\partial^2}{\partial y^2} \right) \tilde{\varphi}(\mathbf{x}),$$

then the governing equations of the pressure wave in the fluid can be expressed as

$$\mathbf{M}(\mathbf{x}) \tilde{\mathbf{p}} = -\rho_f \omega^2 \tilde{\varphi}(\mathbf{x}) \tilde{\mathbf{p}}. \quad (7.1.5)$$

7.1.2 Discretized interface continuity conditions

The interface continuity conditions (2.4.2) can be expressed as

$$\left(\frac{\partial \tilde{\varphi}(\mathbf{x})}{\partial x} n_x + \frac{\partial \tilde{\varphi}(\mathbf{x})}{\partial y} n_y \right) \tilde{\mathbf{p}} = -\rho_f \omega^2 \left(\tilde{\varphi}(\mathbf{x}) \tilde{\mathbf{u}}_x n_x + \tilde{\varphi}(\mathbf{x}) \tilde{\mathbf{u}}_y n_y \right), \quad \mathbf{x} \in \Gamma_0, \quad (7.1.6)$$

And Eq. (2.4.3) can be expressed as

$$\begin{aligned} & \left((\lambda + 2\mu) \frac{\partial \tilde{\varphi}(\mathbf{x})}{\partial x} \tilde{\mathbf{u}}_x + \lambda \frac{\partial \tilde{\varphi}(\mathbf{x})}{\partial y} \tilde{\mathbf{u}}_y \right) n_x + \mu \left(\frac{\partial \tilde{\varphi}(\mathbf{x})}{\partial y} \tilde{\mathbf{u}}_x + \frac{\partial \tilde{\varphi}(\mathbf{x})}{\partial x} \tilde{\mathbf{u}}_y \right) n_y \\ & = \tilde{\varphi}(\mathbf{x}) \tilde{\mathbf{p}} n_x, \quad \mathbf{x} \in \Gamma_0, \end{aligned} \quad (7.1.7)$$

$$\begin{aligned} & \left((\lambda + 2\mu) \frac{\partial \tilde{\varphi}(\mathbf{x})}{\partial y} \tilde{\mathbf{u}}_y + \lambda \frac{\partial \tilde{\varphi}(\mathbf{x})}{\partial x} \tilde{\mathbf{u}}_x \right) n_y + \mu \left(\frac{\partial \tilde{\varphi}(\mathbf{x})}{\partial y} \tilde{\mathbf{u}}_x + \frac{\partial \tilde{\varphi}(\mathbf{x})}{\partial x} \tilde{\mathbf{u}}_y \right) n_x \\ & = \tilde{\varphi}(\mathbf{x}) \tilde{\mathbf{p}} n_y, \quad \mathbf{x} \in \Gamma_0. \end{aligned} \quad (7.1.8)$$

For simplicity we further define

$$\mathbf{O}(\mathbf{x}) = (\lambda + 2\mu) \frac{\partial \tilde{\varphi}(\mathbf{x})}{\partial x} n_x + \mu \frac{\partial \tilde{\varphi}(\mathbf{x})}{\partial y} n_y,$$

$$\mathbf{Q}(\mathbf{x}) = \lambda \frac{\partial \tilde{\varphi}(\mathbf{x})}{\partial y} n_x + \mu \frac{\partial \tilde{\varphi}(\mathbf{x})}{\partial x} n_y,$$

$$\mathbf{S}(\mathbf{x}) = \lambda \frac{\partial \tilde{\varphi}(\mathbf{x})}{\partial x} n_y + \mu \frac{\partial \tilde{\varphi}(\mathbf{x})}{\partial y} n_x,$$

$$\mathbf{R}(\mathbf{x}) = (\lambda + 2\mu) \frac{\partial \tilde{\varphi}(\mathbf{x})}{\partial y} n_y + \mu \frac{\partial \tilde{\varphi}(\mathbf{x})}{\partial x} n_x.$$

Then, we can rewrite Eqs. (7.1.7) and (7.1.8) as

$$\mathbf{O}(\mathbf{x}) \tilde{\mathbf{u}}_x + \mathbf{Q}(\mathbf{x}) \tilde{\mathbf{u}}_y = \tilde{\varphi}(\mathbf{x}) \tilde{\mathbf{p}} n_x, \quad \mathbf{x} \in \Gamma_0, \quad (7.1.9)$$

$$\mathbf{S}(\mathbf{x}) \tilde{\mathbf{u}}_x + \mathbf{R}(\mathbf{x}) \tilde{\mathbf{u}}_y = \tilde{\varphi}(\mathbf{x}) \tilde{\mathbf{p}} n_y, \quad \mathbf{x} \in \Gamma_0. \quad (7.1.10)$$

7.1.3 Discretized periodic boundary conditions

7.1.3.1 Solid/fluid phononic crystals

In the square lattice, the RBF discretization of fluid/solid and solid/fluid system is different. The periodic boundary conditions of these two systems are going to be discussed separate

7.1.3.1.1 Square lattice

For solid/fluid system in a square lattice, the periodic boundary condition (2.4.6) in

the fluid matrix can be expressed as

$$\tilde{\boldsymbol{p}}|_{\Gamma_1} = \tilde{\boldsymbol{p}}|_{\Gamma_3} e^{-ik_x a}, \quad \tilde{\boldsymbol{p}}|_{\Gamma_2} = \tilde{\boldsymbol{p}}|_{\Gamma_4} e^{-ik_y a}, \quad (7.1.11)$$

where $\tilde{\boldsymbol{p}}|_{\Gamma_i}$ ($i=1,2,3,4$) are the elements of the vector $\tilde{\boldsymbol{p}}$ corresponding to the unit-cell boundary $\boldsymbol{x} \in \Gamma_i$. The periodic boundary conditions (2.4.7) can be expressed as

$$\frac{\partial p}{\partial x}(\boldsymbol{x}_{\Gamma_1}) = \frac{\partial p}{\partial x}(\boldsymbol{x}_{\Gamma_3}) e^{-ik_x a}, \quad \frac{\partial p}{\partial y}(\boldsymbol{x}_{\Gamma_2}) = \frac{\partial p}{\partial y}(\boldsymbol{x}_{\Gamma_4}) e^{-ik_y a}. \quad (7.1.12)$$

By considering the RBF approximation (7.1.2), Eq. (7.1.12) can be rewritten as

$$\left(\frac{\partial \tilde{\boldsymbol{\varphi}}(\boldsymbol{x}_{\Gamma_1})}{\partial x} - \frac{\partial \tilde{\boldsymbol{\varphi}}(\boldsymbol{x}_{\Gamma_3})}{\partial x} e^{-ik_x a} \right) \tilde{\boldsymbol{p}} = 0, \quad (7.1.13)$$

$$\left(\frac{\partial \tilde{\boldsymbol{\varphi}}(\boldsymbol{x}_{\Gamma_2})}{\partial y} - \frac{\partial \tilde{\boldsymbol{\varphi}}(\boldsymbol{x}_{\Gamma_4})}{\partial y} e^{-ik_y a} \right) \tilde{\boldsymbol{p}} = 0. \quad (7.1.14)$$

7.1.3.1.2 Triangular lattice

In the solid/fluid system, the periodic boundary conditions are only applied to the acoustic wave field in the fluid matrix, which can be expressed as

$$\begin{aligned} \tilde{\boldsymbol{p}}|_{x_{\Gamma_1}} &= \tilde{\boldsymbol{p}}|_{x_{\Gamma_4}} e^{-i\left(k_x \frac{\sqrt{3}}{2} a + k_y \frac{a}{2}\right)}, \\ \tilde{\boldsymbol{p}}|_{x_{\Gamma_2}} &= \tilde{\boldsymbol{p}}|_{x_{\Gamma_5}} e^{-ik_y a}, \\ \tilde{\boldsymbol{p}}|_{x_{\Gamma_3}} &= \tilde{\boldsymbol{p}}|_{x_{\Gamma_6}} e^{-i\left(-k_x \frac{\sqrt{3}}{2} a + k_y \frac{a}{2}\right)}, \end{aligned} \quad (7.1.15)$$

in which $\tilde{\boldsymbol{p}}|_{\Gamma_i}$ ($i=1, \dots, 6$) denotes the elements of the vector $\tilde{\boldsymbol{p}}$ corresponding to $\boldsymbol{x} \in \Gamma_i$. The periodic pressure derivative boundary conditions (2.4.7) can be expressed as

$$\begin{aligned}
\frac{\partial p(\mathbf{x}_{\Gamma_1})}{\partial \mathbf{n}} &= \frac{\partial p(\mathbf{x}_{\Gamma_4})}{\partial \mathbf{n}} e^{-i\left(k_x \frac{\sqrt{3}}{2} a + k_y \frac{a}{2}\right)}, \\
\frac{\partial p(\mathbf{x}_{\Gamma_2})}{\partial \mathbf{n}} &= \frac{\partial p(\mathbf{x}_{\Gamma_5})}{\partial \mathbf{n}} e^{-ik_y a}, \\
\frac{\partial p(\mathbf{x}_{\Gamma_3})}{\partial \mathbf{n}} &= \frac{\partial p(\mathbf{x}_{\Gamma_6})}{\partial \mathbf{n}} e^{-i\left(-k_x \frac{\sqrt{3}}{2} a + k_y \frac{a}{2}\right)}.
\end{aligned} \tag{7.1.16}$$

By considering the RBF approximation (7.1.2), Eq. (7.1.16) can be recast into

$$\left(\frac{\partial \tilde{\varphi}(\mathbf{x}_{\Gamma_1})}{\partial \mathbf{n}} - \frac{\partial \tilde{\varphi}(\mathbf{x}_{\Gamma_4})}{\partial \mathbf{n}} e^{-i\left(k_x \frac{\sqrt{3}}{2} a + k_y \frac{a}{2}\right)} \right) \tilde{\mathbf{p}} = 0, \tag{7.1.17}$$

$$\left(\frac{\partial \tilde{\varphi}(\mathbf{x}_{\Gamma_2})}{\partial \mathbf{n}} - \frac{\partial \tilde{\varphi}(\mathbf{x}_{\Gamma_5})}{\partial \mathbf{n}} e^{-ik_y a} \right) \tilde{\mathbf{p}} = 0, \tag{7.1.18}$$

$$\left(\frac{\partial \tilde{\varphi}(\mathbf{x}_{\Gamma_3})}{\partial \mathbf{n}} - \frac{\partial \tilde{\varphi}(\mathbf{x}_{\Gamma_6})}{\partial \mathbf{n}} e^{-i\left(-k_x \frac{\sqrt{3}}{2} a + k_y \frac{a}{2}\right)} \right) \tilde{\mathbf{p}} = 0. \tag{7.1.19}$$

7.1.3.2 Fluid/solid phononic crystals

7.1.3.2.1 Square lattice

As shown in the Fig. 5.1, for the square lattice in fluid/solid the periodic boundary conditions are only applied to the elastic waves of the solid part, the periodic displacement boundary conditions (2.4.4) can be expressed as

$$\begin{aligned}
\tilde{\mathbf{u}}_x|_{\Gamma_1} &= \tilde{\mathbf{u}}_x|_{\Gamma_3} e^{-ik_x a}, & \tilde{\mathbf{u}}_y|_{\Gamma_1} &= \tilde{\mathbf{u}}_y|_{\Gamma_3} e^{-ik_x a}, \\
\tilde{\mathbf{u}}_x|_{\Gamma_2} &= \tilde{\mathbf{u}}_x|_{\Gamma_4} e^{-ik_y a}, & \tilde{\mathbf{u}}_y|_{\Gamma_2} &= \tilde{\mathbf{u}}_y|_{\Gamma_4} e^{-ik_y a},
\end{aligned} \tag{7.1.20}$$

where $\tilde{\mathbf{u}}_x|_{\Gamma_i}$ and $\tilde{\mathbf{u}}_y|_{\Gamma_i}$ denote the elements of the vectors $\tilde{\mathbf{u}}_x$ and $\tilde{\mathbf{u}}_y$ corresponding to the unit-cell boundary $\mathbf{x} \in \Gamma_i$. The periodic traction boundary conditions (2.4.5) can be expressed as

$$\begin{aligned}
T_x(\mathbf{x}_{\Gamma_1}) &= T_x(\mathbf{x}_{\Gamma_3}) e^{-ik_x a}, & T_y(\mathbf{x}_{\Gamma_1}) &= T_y(\mathbf{x}_{\Gamma_3}) e^{-ik_x a}, \\
T_x(\mathbf{x}_{\Gamma_2}) &= T_x(\mathbf{x}_{\Gamma_4}) e^{-ik_y a}, & T_y(\mathbf{x}_{\Gamma_2}) &= T_y(\mathbf{x}_{\Gamma_4}) e^{-ik_y a},
\end{aligned} \tag{7.1.21}$$

where $x \in \Gamma_1$, $x \in \Gamma_2$, $x \in \Gamma_3$, $x \in \Gamma_4$, $T_x(\mathbf{x})$ and $T_y(\mathbf{x})$ are the traction vectors.

By considering the following relations

$$\begin{aligned} T_x &= \sigma_{xx}n_x + \sigma_{xy}n_y = \left((\lambda + 2\mu) \frac{\partial u_x}{\partial x} + \lambda \frac{\partial u_y}{\partial y} \right) n_x + \mu \left(\frac{\partial u_x}{\partial y} + \frac{\partial u_y}{\partial x} \right) n_y, \\ &= \mathbf{O}(\mathbf{x})\tilde{\mathbf{u}}_x + \mathbf{Q}(\mathbf{x})\tilde{\mathbf{u}}_y, \end{aligned} \quad (7.1.22)$$

$$\begin{aligned} T_y &= \sigma_{xy}n_x + \sigma_{yy}n_y = \mu \left(\frac{\partial u_x}{\partial y} + \frac{\partial u_y}{\partial x} \right) n_x + \left((\lambda + 2\mu) \frac{\partial u_y}{\partial x} + \lambda \frac{\partial u_x}{\partial y} \right) n_y, \\ &= \mathbf{S}(\mathbf{x})\tilde{\mathbf{u}}_x + \mathbf{R}(\mathbf{x})\tilde{\mathbf{u}}_y, \end{aligned} \quad (7.1.23)$$

the periodic traction boundary conditions (7.1.21) can be expressed as

$$\left(\mathbf{O}(\mathbf{x}_{\Gamma_1}) - \mathbf{O}(\mathbf{x}_{\Gamma_3})e^{-ik_x a} \right) \tilde{\mathbf{u}}_x + \left(\mathbf{Q}(\mathbf{x}_{\Gamma_1}) - \mathbf{Q}(\mathbf{x}_{\Gamma_3})e^{-ik_x a} \right) \tilde{\mathbf{u}}_y = 0, \quad (7.1.24)$$

$$\left(\mathbf{S}(\mathbf{x}_{\Gamma_1}) - \mathbf{S}(\mathbf{x}_{\Gamma_3})e^{-ik_x a} \right) \tilde{\mathbf{u}}_x + \left(\mathbf{R}(\mathbf{x}_{\Gamma_1}) - \mathbf{R}(\mathbf{x}_{\Gamma_3})e^{-ik_x a} \right) \tilde{\mathbf{u}}_y = 0, \quad (7.1.25)$$

$$\left(\mathbf{O}(\mathbf{x}_{\Gamma_2}) - \mathbf{O}(\mathbf{x}_{\Gamma_4})e^{-ik_y a} \right) \tilde{\mathbf{u}}_x + \left(\mathbf{Q}(\mathbf{x}_{\Gamma_2}) - \mathbf{Q}(\mathbf{x}_{\Gamma_4})e^{-ik_y a} \right) \tilde{\mathbf{u}}_y = 0, \quad (7.1.26)$$

$$\left(\mathbf{S}(\mathbf{x}_{\Gamma_2}) - \mathbf{S}(\mathbf{x}_{\Gamma_4})e^{-ik_y a} \right) \tilde{\mathbf{u}}_x + \left(\mathbf{R}(\mathbf{x}_{\Gamma_2}) - \mathbf{R}(\mathbf{x}_{\Gamma_4})e^{-ik_y a} \right) \tilde{\mathbf{u}}_y = 0. \quad (7.1.27)$$

7.1.3.2.2 Triangular lattice

Fig. 5.2 shows the matrix and the scatterer in a unit-cell of a triangle lattice. The discretized periodic boundary conditions for the fluid/solid systems are presented separately in the following.

For the fluid/solid system in a triangle lattice, the discretized periodic boundary conditions are only applied to the elastic wave field of the solid matrix. The periodic displacement boundary conditions (2.4.4) can be expressed as

$$\begin{aligned} \tilde{\mathbf{u}}_x|_{x_{\Gamma_1}} &= \tilde{\mathbf{u}}_x|_{x_{\Gamma_4}} e^{-i\left(k_x \frac{\sqrt{3}}{2}a + k_y \frac{a}{2}\right)}, & \tilde{\mathbf{u}}_y|_{x_{\Gamma_1}} &= \tilde{\mathbf{u}}_y|_{x_{\Gamma_4}} e^{-i\left(k_x \frac{\sqrt{3}}{2}a + k_y \frac{a}{2}\right)}, \\ \tilde{\mathbf{u}}_x|_{x_{\Gamma_2}} &= \tilde{\mathbf{u}}_x|_{x_{\Gamma_5}} e^{-ik_y a}, & \tilde{\mathbf{u}}_y|_{x_{\Gamma_2}} &= \tilde{\mathbf{u}}_y|_{x_{\Gamma_5}} e^{-ik_y a}, \\ \tilde{\mathbf{u}}_x|_{x_{\Gamma_3}} &= \tilde{\mathbf{u}}_x|_{x_{\Gamma_6}} e^{-i\left(-k_x \frac{\sqrt{3}}{2}a + k_y \frac{a}{2}\right)}, & \tilde{\mathbf{u}}_y|_{x_{\Gamma_3}} &= \tilde{\mathbf{u}}_y|_{x_{\Gamma_6}} e^{-i\left(-k_x \frac{\sqrt{3}}{2}a + k_y \frac{a}{2}\right)}, \end{aligned} \quad (7.1.28)$$

where $\tilde{\mathbf{u}}_x|_{x_{\Gamma_i}}$ and $\tilde{\mathbf{u}}_y|_{x_{\Gamma_i}}$ ($i=1, \dots, 6$) are the elements of the vectors $\tilde{\mathbf{u}}_x$ and $\tilde{\mathbf{u}}_y$

corresponding to the unit-cell boundary $\mathbf{x} \in \Gamma_i$. The periodic traction boundary

conditions (2.4.5) can be expressed as

$$\begin{aligned}
T_x(\mathbf{x}_{\Gamma_1}) &= T_x(\mathbf{x}_{\Gamma_4}) e^{-i\left(k_x \frac{\sqrt{3}}{2} a + k_y \frac{a}{2}\right)}, & T_y(\mathbf{x}_{\Gamma_1}) &= T_y(\mathbf{x}_{\Gamma_4}) e^{-i\left(k_x \frac{\sqrt{3}}{2} a + k_y \frac{a}{2}\right)}, \\
T_x(\mathbf{x}_{\Gamma_2}) &= T_x(\mathbf{x}_{\Gamma_5}) e^{-ik_y a}, & T_y(\mathbf{x}_{\Gamma_2}) &= T_y(\mathbf{x}_{\Gamma_5}) e^{-ik_y a}, \\
T_x(\mathbf{x}_{\Gamma_3}) &= T_x(\mathbf{x}_{\Gamma_6}) e^{-i\left(-k_x \frac{\sqrt{3}}{2} a + k_y \frac{a}{2}\right)}, & T_y(\mathbf{x}_{\Gamma_3}) &= T_y(\mathbf{x}_{\Gamma_6}) e^{-i\left(-k_x \frac{\sqrt{3}}{2} a + k_y \frac{a}{2}\right)}.
\end{aligned} \tag{7.1.29}$$

By considering the RBF formulation in (7.1.22) and (7.1.23), the periodic boundary conditions (7.1.29) can be written as

$$\left(\mathbf{O}(\mathbf{x}_{\Gamma_1}) - \mathbf{O}(\mathbf{x}_{\Gamma_4}) e^{-i\left(k_x \frac{\sqrt{3}}{2} a + k_y \frac{a}{2}\right)} \right) \tilde{\mathbf{u}}_x + \left(\mathbf{Q}(\mathbf{x}_{\Gamma_1}) - \mathbf{Q}(\mathbf{x}_{\Gamma_4}) e^{-i\left(k_x \frac{\sqrt{3}}{2} a + k_y \frac{a}{2}\right)} \right) \tilde{\mathbf{u}}_y = 0, \tag{7.1.30}$$

$$\left(\mathbf{S}(\mathbf{x}_{\Gamma_1}) - \mathbf{S}(\mathbf{x}_{\Gamma_4}) e^{-i\left(k_x \frac{\sqrt{3}}{2} a + k_y \frac{a}{2}\right)} \right) \tilde{\mathbf{u}}_x + \left(\mathbf{R}(\mathbf{x}_{\Gamma_1}) - \mathbf{R}(\mathbf{x}_{\Gamma_4}) e^{-i\left(k_x \frac{\sqrt{3}}{2} a + k_y \frac{a}{2}\right)} \right) \tilde{\mathbf{u}}_y = 0, \tag{7.1.31}$$

$$\left(\mathbf{O}(\mathbf{x}_{\Gamma_2}) - \mathbf{O}(\mathbf{x}_{\Gamma_5}) e^{-ik_y a} \right) \tilde{\mathbf{u}}_x + \left(\mathbf{Q}(\mathbf{x}_{\Gamma_2}) - \mathbf{Q}(\mathbf{x}_{\Gamma_5}) e^{-ik_y a} \right) \tilde{\mathbf{u}}_y = 0, \tag{7.1.32}$$

$$\left(\mathbf{S}(\mathbf{x}_{\Gamma_2}) - \mathbf{S}(\mathbf{x}_{\Gamma_5}) e^{-ik_y a} \right) \tilde{\mathbf{u}}_x + \left(\mathbf{R}(\mathbf{x}_{\Gamma_2}) - \mathbf{R}(\mathbf{x}_{\Gamma_5}) e^{-ik_y a} \right) \tilde{\mathbf{u}}_y = 0, \tag{7.1.33}$$

$$\left(\mathbf{O}(\mathbf{x}_{\Gamma_3}) - \mathbf{O}(\mathbf{x}_{\Gamma_6}) e^{-i\left(-k_x \frac{\sqrt{3}}{2} a + k_y \frac{a}{2}\right)} \right) \tilde{\mathbf{u}}_x + \left(\mathbf{Q}(\mathbf{x}_{\Gamma_3}) - \mathbf{Q}(\mathbf{x}_{\Gamma_6}) e^{-i\left(-k_x \frac{\sqrt{3}}{2} a + k_y \frac{a}{2}\right)} \right) \tilde{\mathbf{u}}_y = 0, \tag{7.1.34}$$

$$\left(\mathbf{S}(\mathbf{x}_{\Gamma_3}) - \mathbf{S}(\mathbf{x}_{\Gamma_6}) e^{-i\left(-k_x \frac{\sqrt{3}}{2} a + k_y \frac{a}{2}\right)} \right) \tilde{\mathbf{u}}_x + \left(\mathbf{R}(\mathbf{x}_{\Gamma_3}) - \mathbf{R}(\mathbf{x}_{\Gamma_6}) e^{-i\left(-k_x \frac{\sqrt{3}}{2} a + k_y \frac{a}{2}\right)} \right) \tilde{\mathbf{u}}_y = 0, \tag{7.1.35}$$

7.1.4 Eigenvalue equations

7.1.4.1 Square lattice

By collocating the discretized governing wave equations (7.1.3)-(7.1.5), the discretized interface conditions (7.1.6), (7.1.9) and (7.1.10) on the N interior and boundary nodes, and the discretized periodic boundary conditions for the tractions in the fluid/solid system (i.e., Eqs. (7.1.21) and (7.1.29)) while for the normal derivative

of the pressure in the solid/fluid system (i.e., Eqs. (7.1.12) and (7.1.16)) we obtain the eigenvalue equation in the following matrix form

$$\mathbf{A}\mathbf{U} = -\omega^2 \mathbf{H}\mathbf{U}, \quad (7.1.36)$$

where ω denotes the eigenvalues to be determined, and the eigenvector is defined by

$$\mathbf{U} = [\tilde{\mathbf{u}}_x, \tilde{\mathbf{u}}_y, \tilde{\mathbf{p}}]^T. \quad (7.1.37)$$

The system matrices \mathbf{A} and \mathbf{H} have the same size and they are given in the Appendices A and B.

By invoking the discretized periodic boundary conditions for the displacements in the fluid/solid system (i.e., Eqs. (7.1.20) and (7.1.28)) and for the pressure in the solid/fluid system (i.e., Eqs. (7.1.11) and (7.1.15)) as described in the following subsections, some nodal unknowns on the unit-cell boundary can be eliminated. This leads to the following reduced generalized eigenvalue equation

$$\tilde{\mathbf{A}}\tilde{\mathbf{U}} = -\omega^2 \tilde{\mathbf{H}}\tilde{\mathbf{U}}, \quad (7.1.38)$$

where the reduced matrices $\tilde{\mathbf{A}}$ and $\tilde{\mathbf{H}}$ and the reduced vector $\tilde{\mathbf{U}}$ are dependent on the lattice form and the material combination (fluid/solid or solid/fluid systems), which are presented and described in the following.

System 1: Fluid/solid system

According to the periodic displacement boundary conditions in Eq. (7.1.20), the nodal displacements on Γ_3 and Γ_4 can be eliminated by using the nodal displacements on Γ_1 and Γ_2 , which results in the following reduced matrices and vector

$$\tilde{\mathbf{A}} = \left[\mathbf{A}_{x_0}, \mathbf{A}_{x_{\Gamma_0}^0}, \mathbf{A}_{x_1}, \mathbf{A}_{x_{\Gamma_0}^1}, \mathbf{A}_{x_{\Gamma_1}} + \mathbf{A}_{x_{\Gamma_3}} e^{ik_x a}, \mathbf{A}_{x_{\Gamma_2}} + \mathbf{A}_{x_{\Gamma_4}} e^{ik_y a} \right], \quad (7.1.39)$$

$$\tilde{\mathbf{H}} = \left[\mathbf{H}_{x_0}, \mathbf{H}_{x_{\Gamma_0}^0}, \mathbf{H}_{x_1}, \mathbf{H}_{x_{\Gamma_0}^1}, \mathbf{H}_{x_{\Gamma_1}}, \mathbf{H}_{x_{\Gamma_2}} \right], \quad (7.1.40)$$

$$\tilde{\mathbf{U}} = \left[\mathbf{U}_{x_1}, \mathbf{U}_{x_{\Gamma_0}^1}, \mathbf{U}_{x_0}, \mathbf{U}_{x_{\Gamma_0}^0}, \mathbf{U}_{x_{\Gamma_1}}, \mathbf{U}_{x_{\Gamma_2}} \right]^T, \quad (7.1.41)$$

where the subscript \mathbf{x} in $\mathbf{A}_{\mathbf{x}}$ and $\mathbf{H}_{\mathbf{x}}$ indicates the corresponding columns inside

the matrices \mathbf{A} and \mathbf{H} related to \mathbf{x} , while the subscript \mathbf{x} in $U_{\mathbf{x}}$ designates the corresponding rows of the vector \mathbf{U} corresponding to \mathbf{x} . The matrices $\tilde{\mathbf{A}}$ and $\tilde{\mathbf{H}}$ have the same size $N_1 \times N_1$, while the matrices \mathbf{A} and \mathbf{H} have the size $N_1 \times N_a$. The size of the reduced vector $\tilde{\mathbf{U}}$ is N_1 , while the size of the vector \mathbf{U} is N_a , where

$$N_1 = 2N_{x_0} + N_{x_1} + 2N_{x_{\Gamma_0}^0} + N_{x_{\Gamma_0}^1} + 2N_{x_{\Gamma_1}} + 2N_{x_{\Gamma_2}},$$

$$N_a = 2N_{x_0} + N_{x_1} + 2N_{x_{\Gamma_0}^0} + N_{x_{\Gamma_0}^1} + 2N_{x_{\Gamma_1}} + 2N_{x_{\Gamma_2}} + 2N_{x_{\Gamma_3}} + 2N_{x_{\Gamma_4}},$$

with $N_{\mathbf{x}}$ being the total number of the nodes on \mathbf{x} . Here, $x_{\Gamma_0}^0 \in \Gamma_0$ belongs to the domain D_0 , and $x_{\Gamma_0}^1 \in \Gamma_0$ belongs to the domain D_1 . The reduced vector $\tilde{\mathbf{U}}$ contains the nodal displacements in $D_0 \cup \Gamma_0^0 \cup \Gamma_1 \cup \Gamma_2$ and the nodal pressure values in $D_1 \cup \Gamma_0^1$.

System 2: Solid/fluid system

In this case, the periodic pressure boundary conditions (7.1.11) imply that the nodal pressure values on the unit-cell boundaries Γ_3 and Γ_4 can be eliminated by using the nodal pressure values on Γ_1 and Γ_2 . Thus, we obtain

$$\tilde{\mathbf{A}} = \left[\mathbf{A}_{x_0}, \mathbf{A}_{x_{\Gamma_0}^0}, \mathbf{A}_{x_1}, \mathbf{A}_{x_{\Gamma_0}^1}, \mathbf{A}_{x_{\Gamma_1}} + \mathbf{A}_{x_{\Gamma_3}} e^{ik_x a}, \mathbf{A}_{x_{\Gamma_2}} + \mathbf{A}_{x_{\Gamma_4}} e^{ik_x a} \right], \quad (7.1.42)$$

$$\tilde{\mathbf{H}} = \left[\mathbf{H}_{x_0}, \mathbf{H}_{x_{\Gamma_0}^0}, \mathbf{H}_{x_1}, \mathbf{H}_{x_{\Gamma_0}^1}, \mathbf{H}_{x_{\Gamma_1}}, \mathbf{H}_{x_{\Gamma_2}} \right], \quad (7.1.43)$$

$$\tilde{\mathbf{U}} = \left[\mathbf{U}_{x_1}, \mathbf{U}_{x_{\Gamma_0}^1}, \mathbf{U}_{x_0}, \mathbf{U}_{x_{\Gamma_0}^0}, \mathbf{U}_{x_{\Gamma_1}}, \mathbf{U}_{x_{\Gamma_2}} \right]^T, \quad (7.1.44)$$

where the matrices $\tilde{\mathbf{A}}$ and $\tilde{\mathbf{H}}$ have the same size $N_1 \times N_1$ while \mathbf{A} and \mathbf{H} have the size $N_1 \times N_a$, and

$$N_1 = N_{x_0} + 2N_{x_1} + 2N_{x_{\Gamma_0}^0} + N_{x_{\Gamma_0}^1} + N_{x_{\Gamma_1}} + N_{x_{\Gamma_2}},$$

$$N_a = N_{x_0} + 2N_{x_1} + 2N_{x_{\Gamma_0}^0} + N_{x_{\Gamma_0}^1} + N_{x_{\Gamma_1}} + N_{x_{\Gamma_2}} + N_{x_{\Gamma_3}} + N_{x_{\Gamma_4}}.$$

The reduced vector $\tilde{\mathbf{U}}$ contains the nodal displacements in $D_1 \cup \Gamma_0^1$ and the nodal pressure values in $D_0 \cup \Gamma_0^1 \cup \Gamma_1 \cup \Gamma_2$.

7.1.4.2 Triangular lattice

System 1: Solid/fluid system

In the case of the solid/fluid system with a triangular lattice, the periodic displacement boundary conditions (7.1.15) result in the following reduced matrices and vector

$$\tilde{\mathbf{A}} = \begin{bmatrix} \mathbf{A}_{x_0}, \mathbf{A}_{x_{\Gamma_0^0}}, \mathbf{A}_{x_1}, \mathbf{A}_{x_{\Gamma_0^1}}, \mathbf{A}_{x_{\Gamma_1}} + \mathbf{A}_{x_{\Gamma_4}} e^{i\left(k_x \frac{\sqrt{3}}{2}a + k_y \frac{a}{2}\right)}, \\ \mathbf{A}_{x_{\Gamma_2}} + \mathbf{A}_{x_{\Gamma_5}} e^{ik_y a}, \mathbf{A}_{x_{\Gamma_3}} + \mathbf{A}_{x_{\Gamma_6}} e^{i\left(-k_x \frac{\sqrt{3}}{2}a + k_y \frac{a}{2}\right)} \end{bmatrix}, \quad (7.1.45)$$

$$\tilde{\mathbf{H}} = \left[\mathbf{H}_{x_0}, \mathbf{H}_{x_{\Gamma_0^0}}, \mathbf{H}_{x_1}, \mathbf{H}_{x_{\Gamma_0^1}}, \mathbf{H}_{x_{\Gamma_1}}, \mathbf{H}_{x_{\Gamma_2}}, \mathbf{H}_{x_{\Gamma_3}} \right], \quad (7.1.46)$$

$$\tilde{\mathbf{U}} = \left[\mathbf{U}_{x_1}, \mathbf{U}_{x_{\Gamma_0^1}}, \mathbf{U}_{x_0}, \mathbf{U}_{x_{\Gamma_0^0}}, \mathbf{U}_{x_{\Gamma_1}}, \mathbf{U}_{x_{\Gamma_2}}, \mathbf{U}_{x_{\Gamma_3}} \right]^T, \quad (7.1.47)$$

where $\tilde{\mathbf{A}}$ and $\tilde{\mathbf{H}}$ are sparse matrices with the same size $N_1 \times N_1$, while the matrices \mathbf{A} and \mathbf{H} have the size $N_1 \times N_a$. Here,

$$N_1 = N_{x_0} + 2N_{x_1} + N_{x_{\Gamma_0^0}} + 2N_{x_{\Gamma_0^1}} + N_{x_{\Gamma_1}} + N_{x_{\Gamma_2}} + N_{x_{\Gamma_3}},$$

$$N_a = N_{x_0} + 2N_{x_1} + N_{x_{\Gamma_0^0}} + 2N_{x_{\Gamma_0^1}} + N_{x_{\Gamma_1}} + N_{x_{\Gamma_2}} + N_{x_{\Gamma_3}} + N_{x_{\Gamma_4}} + N_{x_{\Gamma_5}} + N_{x_{\Gamma_6}}.$$

The reduced vector $\tilde{\mathbf{U}}$ involves the nodal displacements in $D_1 \cup \Gamma_1^0$ and the nodal pressure values in $D_0 \cup \Gamma_0^0 \cup \Gamma_1 \cup \Gamma_2 \cup \Gamma_3$, respectively.

System 2: Fluid/solid system

For the fluid/solid system with a triangular lattice, the periodic displacement boundary conditions (7.1.28) yield the following reduced matrices and vector

$$\tilde{\mathbf{A}} = \begin{bmatrix} \mathbf{A}_{x_0}, \mathbf{A}_{x_{\Gamma_0}^0}, \mathbf{A}_{x_1}, \mathbf{A}_{x_{\Gamma_0}^1}, \mathbf{A}_{x_{\Gamma_1}}, \mathbf{A}_{x_{\Gamma_4}} e^{i\left(k_x \frac{\sqrt{3}}{2} a + k_y \frac{a}{2}\right)}, \\ \mathbf{A}_{x_{\Gamma_2}} + \mathbf{A}_{x_{\Gamma_5}} e^{ik_y a}, \mathbf{A}_{x_{\Gamma_3}} + \mathbf{A}_{x_{\Gamma_6}} e^{i\left(-k_x \frac{\sqrt{3}}{2} a + k_y \frac{a}{2}\right)} \end{bmatrix}, \quad (7.1.48)$$

$$\tilde{\mathbf{H}} = \left[\mathbf{H}_{x_0}, \mathbf{H}_{x_{\Gamma_0}^0}, \mathbf{H}_{x_1}, \mathbf{H}_{x_{\Gamma_0}^1}, \mathbf{H}_{x_{\Gamma_1}}, \mathbf{H}_{x_{\Gamma_2}}, \mathbf{H}_{x_{\Gamma_3}} \right], \quad (7.1.49)$$

$$\tilde{\mathbf{U}} = \left[\mathbf{U}_{x_1}, \mathbf{U}_{x_{\Gamma_0}^1}, \mathbf{U}_{x_0}, \mathbf{U}_{x_{\Gamma_0}^0}, \mathbf{U}_{x_{\Gamma_1}}, \mathbf{U}_{x_{\Gamma_2}}, \mathbf{U}_{x_{\Gamma_3}} \right]^T, \quad (7.1.50)$$

where the size of $\tilde{\mathbf{A}}$ and $\tilde{\mathbf{H}}$ is $N_1 \times N_1$ while the size of \mathbf{A} and \mathbf{H} is $N_1 \times N_a$

with

$$N_1 = 2N_{x_0} + N_{x_1} + 2N_{x_{\Gamma_0}^0} + N_{x_{\Gamma_0}^1} + 2N_{x_{\Gamma_1}} + 2N_{x_{\Gamma_2}} + 2N_{x_{\Gamma_3}},$$

$$N_a = 2N_{x_0} + N_{x_1} + 2N_{x_{\Gamma_0}^0} + N_{x_{\Gamma_0}^1} + 2N_{x_{\Gamma_1}} + 2N_{x_{\Gamma_2}} + 2N_{x_{\Gamma_3}} + 2N_{x_{\Gamma_4}} + 2N_{x_{\Gamma_5}} + 2N_{x_{\Gamma_6}}.$$

The reduced vector $\tilde{\mathbf{U}}$ contains the nodal displacements in $D_0 \cup \Gamma_0^0 \cup \Gamma_1 \cup \Gamma_2 \cup \Gamma_3$ and the nodal pressure values in $D_1 \cup \Gamma_1^0$.

7.2 Numerical results and discussions

7.2.1 Solid/fluid phononic crystals

For the solid/fluid system, we consider two different materials with different scatterer shapes. For iron scatterers embedded in the air matrix, the constants of the component materials are given by:

$$\rho_s = 7670 \text{ kg} / \text{m}^3, \quad \lambda = 1.17 \times 10^{11} \text{ N} / \text{m}^2, \quad \mu = 7.99 \times 10^{10} \text{ N} / \text{m}^2,$$

$$\rho_f = 1.21 \text{ kg} / \text{m}^3, \quad K = 139876 \text{ N} / \text{m}^2.$$

The acoustic impedance ratio of the considered phononic crystal is $\rho_f \sqrt{K / \rho_f} / (\rho_s \sqrt{\mu / \rho_s}) = 1.66 \times 10^{-5}$, where $\sqrt{K / \rho_f}$ is the acoustic wave speed of the fluid and $\sqrt{\mu / \rho_s}$ is the transverse wave velocity of the solid.

For aluminium scatterers embedded in the mercury matrix, the constants of the component materials are:

$$\rho_s = 2730 \text{ kg/m}^3, \quad \lambda = 4.59 \times 10^{10} \text{ N/m}^2, \quad \mu = 2.7 \times 10^{10} \text{ N/m}^2,$$

$$\rho_f = 13500 \text{ kg/m}^3, \quad K = 2.86 \times 10^{10} \text{ N/m}^2.$$

In this case, the acoustic impedance ratio of the considered phononic crystal is $\rho_f \sqrt{K/\rho_f} / (\rho_s \sqrt{\mu/\rho_s}) = 0.463$. Fig. 7.1 shows the node distribution of the phononic crystal in a square lattice with square scatterers. The filling fraction of the square lattice with square scatterers is 0.138, the area of the square scatterer is 0.4×0.4 and the unit-cell area is 1×1 . Totally 433 nodes are uniformly distributed due to the uniform distributed nodes are much better in convergence according to our previous work [143, 144]. By using this distribution, there are always nodes along the x or y direction so that the direct method is employed to treat the traction on the boundary and the common interface, the shape parameter is $\xi = 1$ and the number of the local nodes is 9. The green nodes are located at the interface, the blue nodes and red nodes are respectively representing the scatterers and the matrix.

Fig. 7.2 and Fig. 7.3 respectively show the bandgaps of aluminum/mercury and air/iron of phononic crystal in a square lattice with square scatterers, where the normalized frequency $\omega/(2\pi c_1)$ is introduced which $c_1 = \sqrt{\mu/\rho_s}$ in solid/fluid system and $c_1 = \sqrt{K/\rho_f}$ in fluid/solid system. The results of the LRBFCM depicted in red line are compared with the results of finite element method. Both of the figures show that results are fitting quite well, and the change of the materials does not affect the results in the LRBFCM.

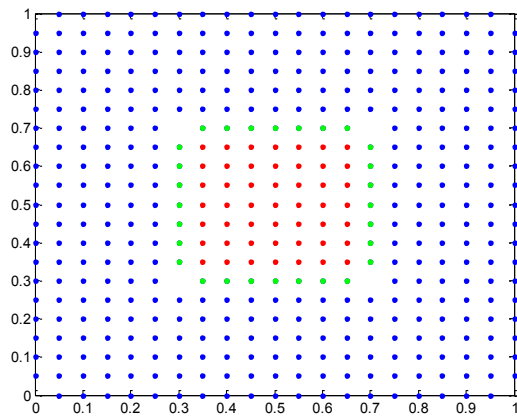


Fig. 7.1 Node distribution in a square lattice with square scatterers.

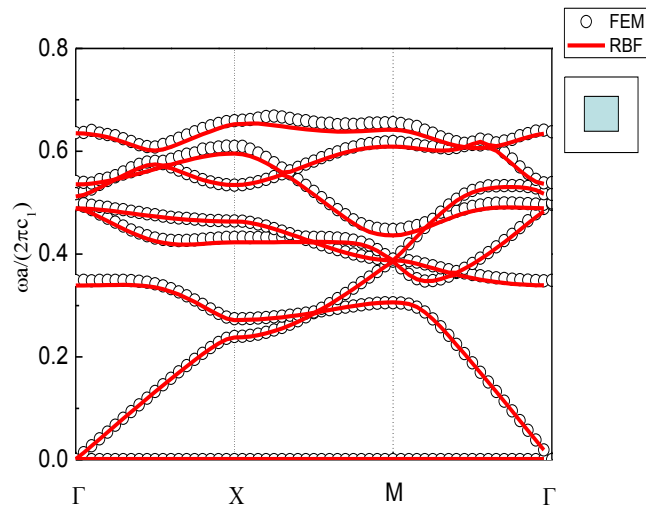


Fig. 7.2 Band structure of aluminum embedded in mercury.

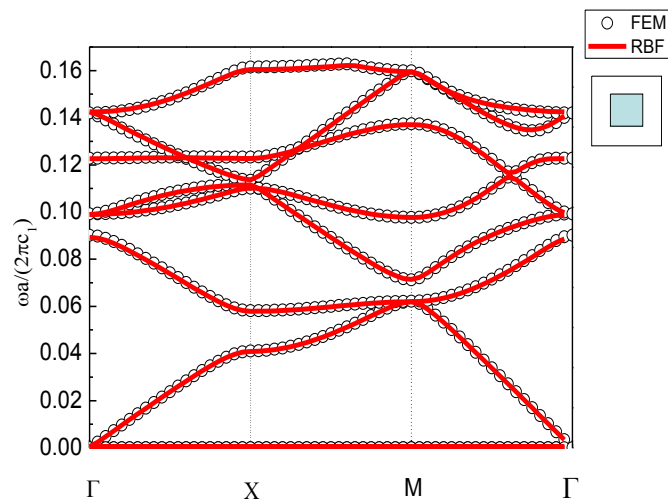


Fig. 7.3 Band structure of iron embedded in air.

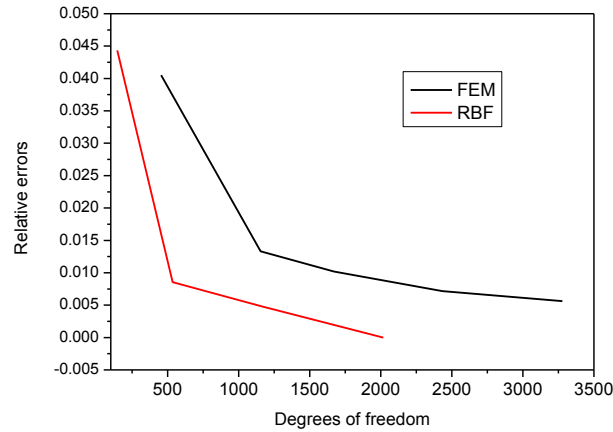


Fig. 7.4 Convergence rate of the averaged eigenvalues for the aluminum embedded in the mercury.

In Fig. 7.4, the convergence rate of the direct method for the average of all eigenvalues is given in terms of the relative error $(E_r - E_m)/E_r$, in which E_r is the result by using 1673 nodes and E_m is the result by using the current nodes number. From Fig. 7.4, it is obvious that the convergence rate of FEM is lower than LRBFCM in solving the solid/fluid system of the aluminum embedded in the mercury.

In the next example, a square lattice with circular scatterers is considered. The filling fraction is 0.2826, the radius of the circular scatterers is 0.3, and totally 1011 nodes are used as shown in Fig. 7.5. For the nodes on the circular interface, nodes in the x - or y - direction can always be found, then the indirect can be employed here to deal with the boundary conditions that required in the solid/fluid interface. The shape parameter $\xi = 1$ with 9 local number nodes is employed in this case. Fig. 7.6 and Fig. 7.7 show the results of the band structures of the FEM and RBF, the present numerical results and the FEM results are fitting quite well in general. This indicates that the geometry variation of the inclusions does not affect the results in the LRBFCM.

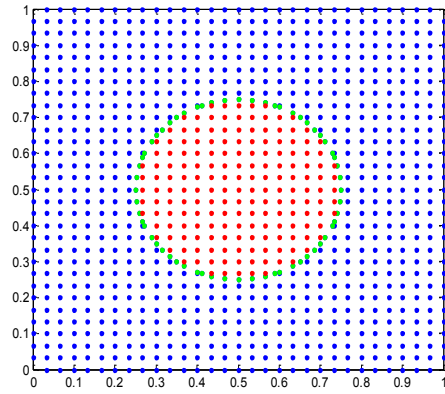


Fig. 7.5 Node distribution in a square lattice with circular scatterers.

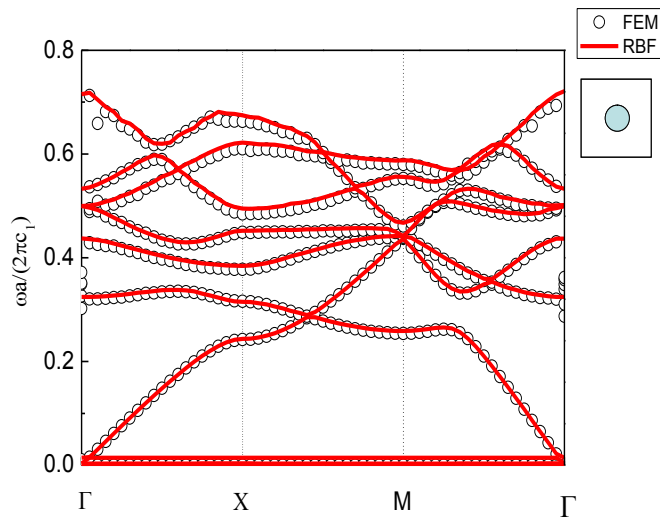


Fig. 7.6 Band structure of aluminum embedded in mercury.

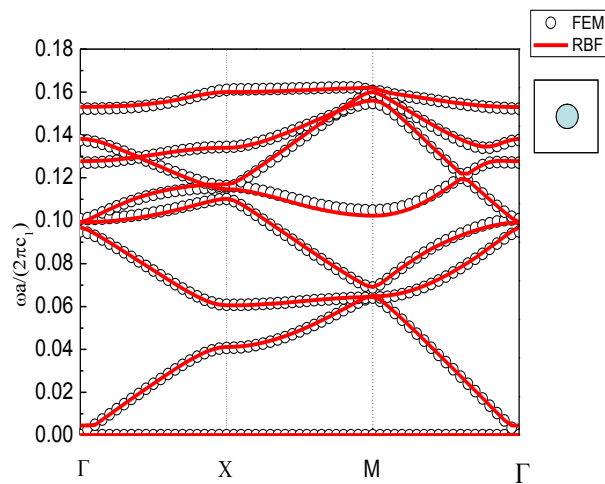


Fig. 7.7 Band structure of iron embedded in air.

In the next example, a triangular lattice with square scatterers is considered. The filling fraction is 0.08, the radius of the circular scatterers is 0.25, and totally 727 nodes are used as shown in Fig. 7.8. The shape parameter $\xi = 1$ with 9 local number nodes is employed in this case. Fig. 7.9 and Fig. 7.10 show the results of the band structures obtained by the LRBFCM and the FEM. Here again, a quite well agreement between the present numerical results and the FEM results is observed. By comparing this example with the previous examples, it can be concluded that the change of the lattice forms does not affect the accuracy of the LRBFCM as well.

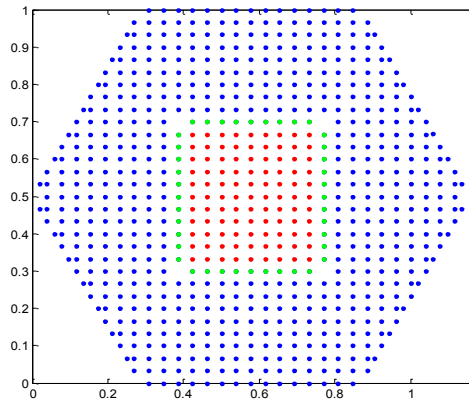


Fig. 7.8 Node distribution in a triangular lattice with square scatterers.

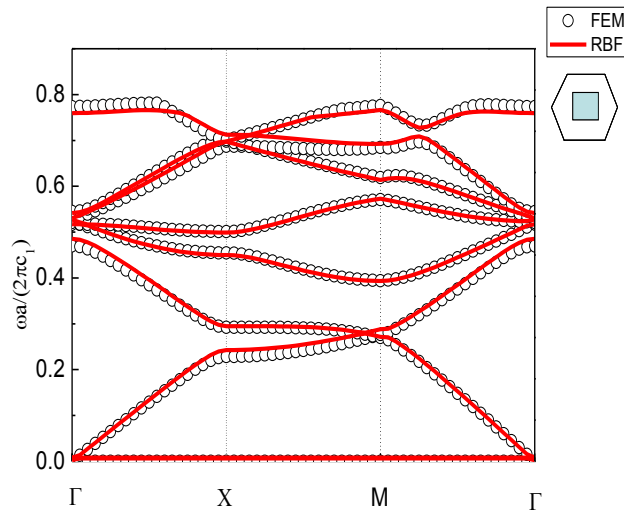


Fig. 7.9 Band structure of iron embedded in water.

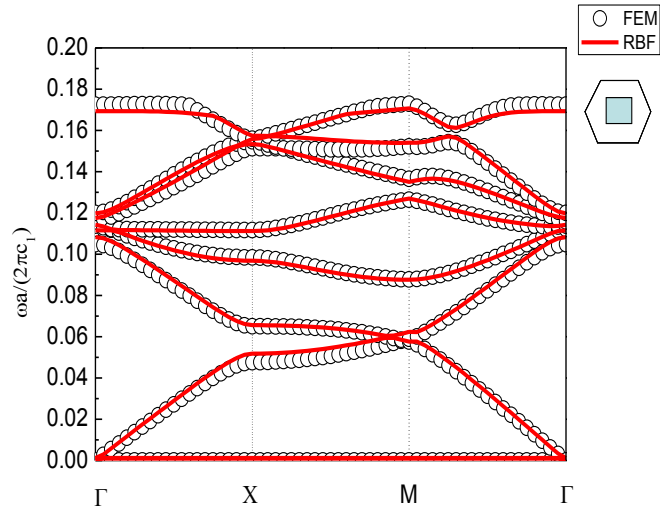


Fig. 7.10 Band structure of iron embedded in air.

In the next example, a triangular lattice with circular scatterers is considered. The filling fraction is 0.196, the radius of the circular scatterers is 0.25, and totally 775 nodes are used as shown in Fig. 7.11. The shape parameter $\xi = 1$ with 9 local number nodes is employed in this case. Fig. 7.12 and Fig. 7.13 show the results of the band structures of the FEM and RBF, the present numerical results and the FEM results are fitting quite well in general. The variation of the geometry and materials in both lattice and inclusions does not affect the results in LRBFCM.

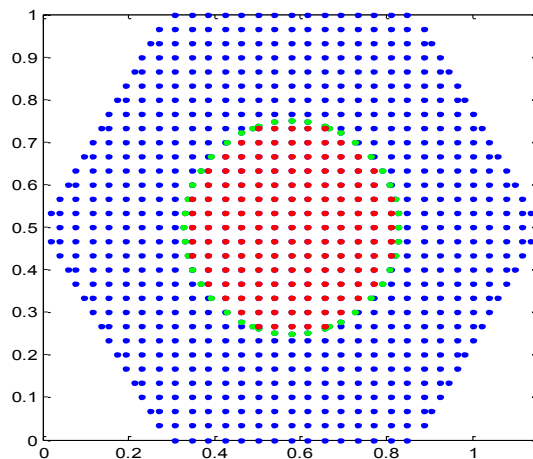


Fig. 7.11 Node distribution in a triangular lattice with circular scatterers.

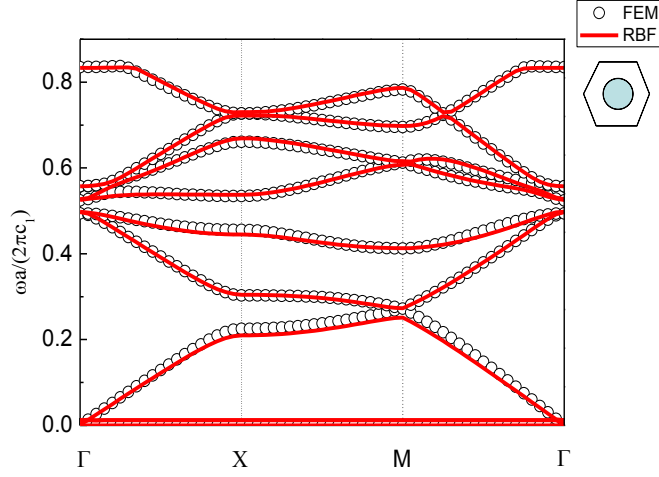


Fig. 7.12 Band structure of iron embedded in water.

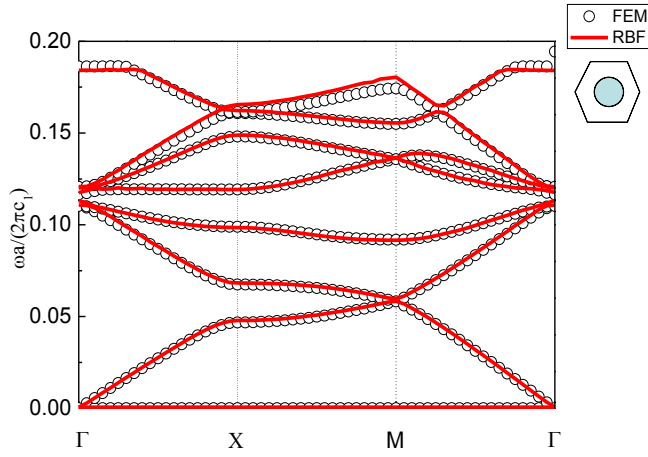


Fig. 7.13 Band structure of iron embedded in air.

7.2.2 Fluid/solid phononic crystals

In this part, we discuss the fluid/solid system, which the fluid is embedded in the solid. The water embedded in iron and air embedded in iron are going to be considered here. The materials property of water embedded in the iron are:

$$\rho_s = 7670 \text{ kg/m}^3, \quad \lambda = 1.17 \times 10^{11} \text{ N/m}^2, \quad \mu = 7.99 \times 10^{10} \text{ N/m}^2,$$

$$\rho_f = 1025 \text{ kg/m}^3, \quad K = 2.40 \times 10^9 \text{ N/m}^2.$$

In this case, the acoustic impedance ratio of the considered phononic crystal is

$$\frac{\rho_s \sqrt{\mu / \rho_s}}{\rho_f \sqrt{K / \rho_f}} = 15.77, \quad \sqrt{\mu / \rho_s} \quad \text{or} \quad \sqrt{K / \rho_f} \quad \text{is the wave speed. For air embedded in}$$

the iron, the parameters of the component materials are:

$$\rho_s = 7670 \text{ kg} / \text{m}^3, \quad \lambda = 1.17 \times 10^{11} \text{ N} / \text{m}^2, \quad \mu = 7.99 \times 10^{10} \text{ N} / \text{m}^2,$$

$$\rho_f = 1.21 \text{ kg} / \text{m}^3, \quad K = 139876 \text{ N} / \text{m}^2.$$

The acoustic impedance ratio of the considered phononic crystal is

$$\frac{\rho_s \sqrt{\mu / \rho_s}}{\rho_f \sqrt{K / \rho_f}} = 60241.$$

The band structures of the square lattice (solid) with square scatterers (fluid) are considered, the band structures of the water/iron and air/iron phononic crystals are compared with those obtained by the FEM in Fig. 7.15 and Fig. 7.16. 953 nodes are uniformly distributed as shown in Fig. 7.14, the shape parameter is taken as $\xi = 3$ and the number of the local nodes is chosen as 9. The present results are fitting quite well with the FEM results in general, however we have found that a higher number of nodes compared with the solid/fluid system must be employed to obtain accurate results both in the LRBFCM and the FEM. 953 nodes must be employed to guarantee the stability of the results in the LRBFCM however more than 40,000 degree of freedom should be employed in the FEM. The computational efficiency is very slow in FEM for the fluid/solid system here. All the FEM cases presented in the figures are using a high number of meshes.

Another interesting thing is the flat band, since the $c_1 = \sqrt{K / \rho_f}$ is employed here, the value of the flat band are almost the same level in Fig. 7.15 and Fig. 7.16. This is because of the large acoustic impedance ratio, when the solid materials property is much larger than fluid, the fluid has few influence to the solid at the interface, and the solid exhibits as a hard wall for the fluid with very tiny displacements in the solid. In the Fig. 7.15, the water is still influenced by iron and does not exhibit any bands as flat as air/iron due to the acoustic impedance ratio is not big enough, while in the Fig. 7.16, the wave speed of the air is much lower than iron

so that the flat bands are formed.

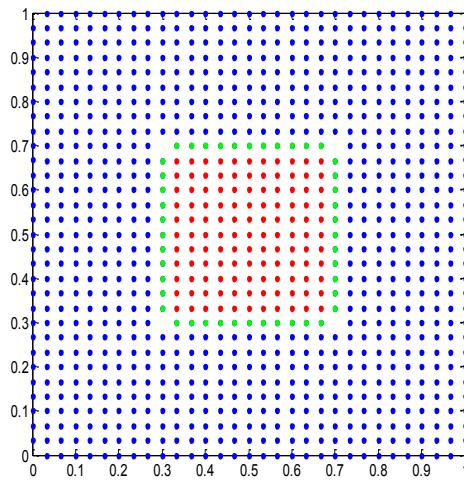


Fig. 7.14 Node distribution in a square lattice with square scatterers.

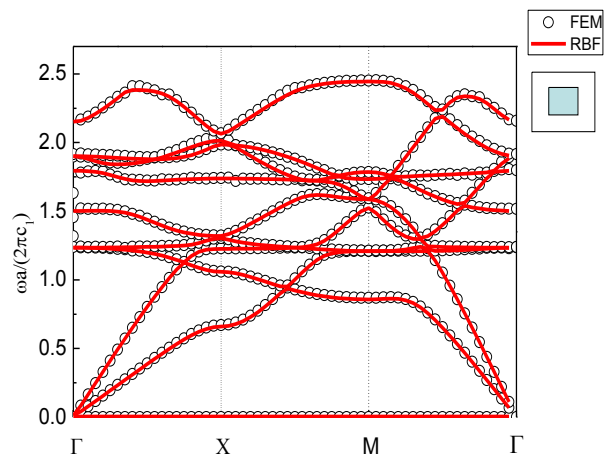


Fig. 7.15 Band structure of water embedded in iron.

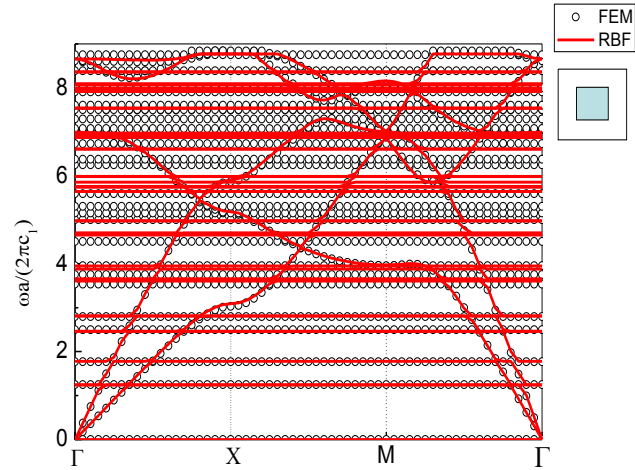


Fig. 7.16 Band structure of air embedded in iron.

The band structures of the square lattice (solid) with circular scatterers (fluid) are considered here, the iron/water and iron/air phononic crystals are compared with that obtained by the FEM in Fig. 7.18 and Fig. 7.19, 952 nodes are uniformly distributed as shown in Fig. 7.22, the shape parameter is taken as $\xi = 3$ and the number of the local nodes is chosen as 12 due to some nodes are very close at the interface. The present results are fitting quite well with the FEM results in general. The values of the flat band are almost the same level in Fig. 7.18 and Fig. 7.19, which are the same as pervious cases.

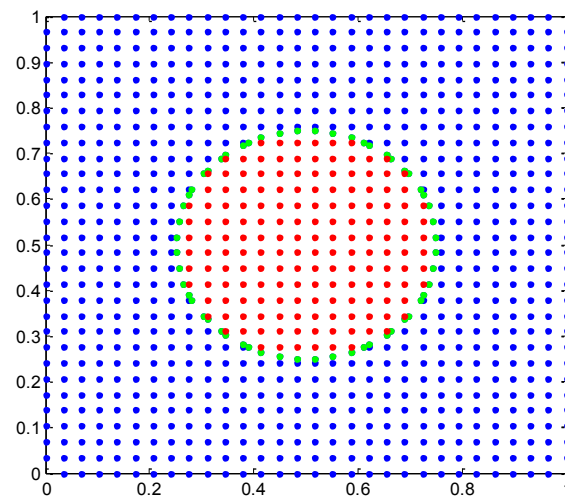


Fig. 7.17 Node distribution in a square lattice with circular scatterers.

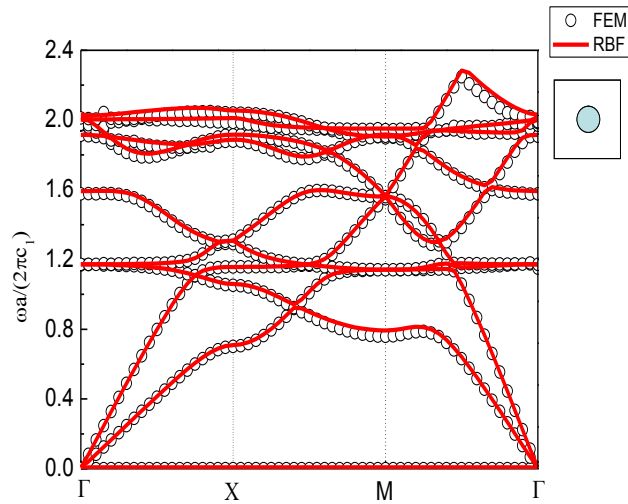


Fig. 7.18 Band structure of water embedded in iron.

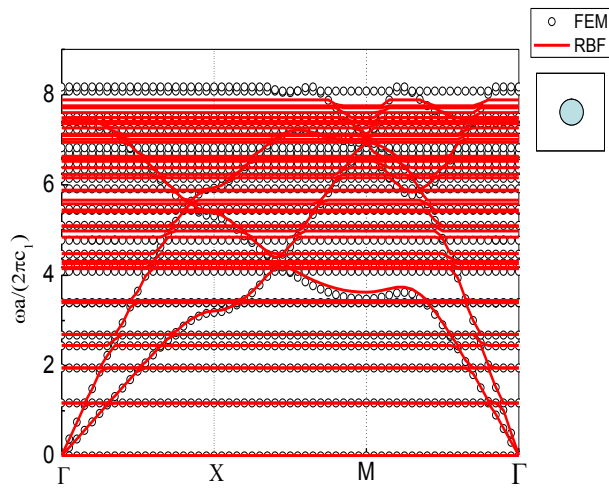


Fig. 7.19 Band structure of air embedded in iron.

The square lattice (solid) with circular scatterers (fluid) are considered here, the band structures of the iron/water and iron/air phononic crystals are compared that obtained by the LRBFCM are compared with FEM in Fig. 7.18 and Fig. 7.19. 952 nodes are uniformly distributed as shown in Fig. 7.22, the shape parameter is taken as $c_s = 3$ and the number of the local nodes is chosen as 9. The present results are fitting quite well with the FEM results in general. The eigenvalues of the flat band are almost the same level in both Fig. 7.18 and Fig. 7.19, which are the same as pervious cases.

This supported that the flat bands can be found when the wave speed of the fluid are much smaller than the solid.

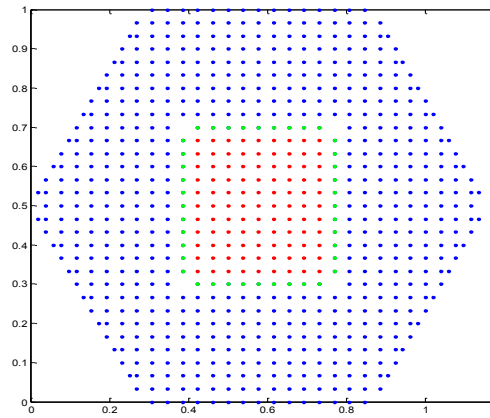


Fig. 7. 20 Node distribution in a triangular lattice with square scatterers.

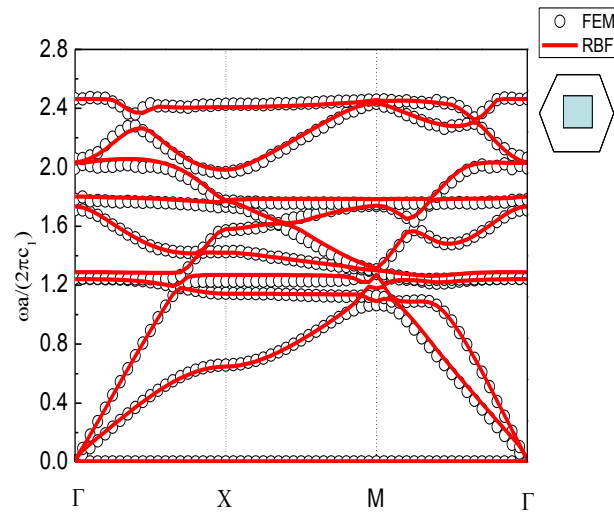


Fig. 7.21 Band structure of water embedded in iron.

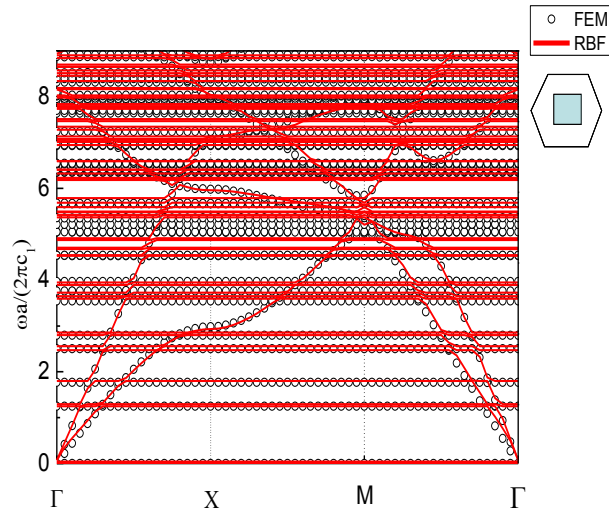


Fig. 7.22 Band structure of air embedded in iron.

The triangular lattice (solid) with square scatterers (fluid) are considered here, the band structures of the iron/water and iron/ air that obtained by the LRFCM are compared with FEM. In Fig. 7.21 and Fig. 7.22, 727 nodes are uniformly distributed as shown in Fig. 7.22, the shape parameter is taken as $\xi=3$ and the number of the local nodes is chosen as 9. The present results are fitting quite well with the FEM results in general. The values of the flat band are almost the same level in Fig. 7.21 and Fig. 7.22, which are the same as pervious cases. This supported that the flat bands can be found when the wave speed of the fluid are much smaller than the solid.

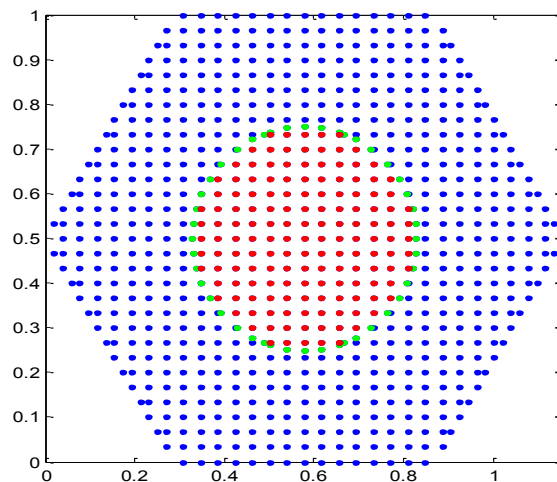


Fig. 7.23 Node distribution in a triangular lattice with circular scatterers.

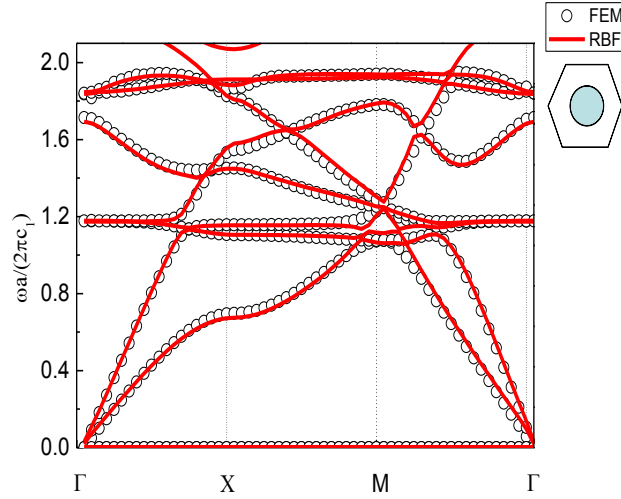


Fig. 7.24 Band structure of water embedded in iron.

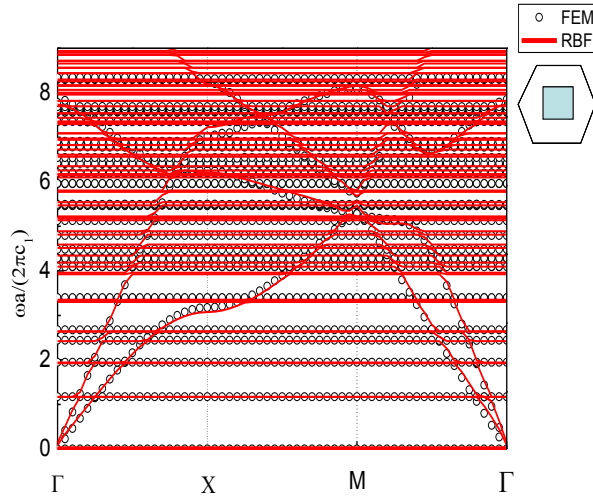


Fig. 7.25 Band structure of air embedded in iron.

The triangular lattice (solid) with circular scatterers (fluid) are considered here, the band structures of the iron/water and iron/air that obtained by the LRBFCM in are compared with FEM in Fig. 7.24 and Fig. 7.25. 727 nodes are uniformly distributed as shown in Fig. 7.23, the shape parameter is taken as $\xi = 3$ and the number of the local nodes is chosen as 9. The present results are fitting quite well with the FEM results in general. The eigenvalues of the flat band are almost at the same level in Fig. 7.24 and Fig. 7.25, which are the same as pervious cases. This supported that the flat bands can be found when the wave speed of the fluid are much smaller than the solid.

7.3 Analysis of the computational efficiency

In order to show the computational efficiency and accuracy of the present LRBFCM, the required computing time and the accuracy for the previously presented numerical examples are summarized in Table 7.1 to Table 7.4 compared with that of the FEM. Here, the numerical error is defined as

$$Error = \frac{\sum (E_f - E_r)}{\sum E_f} ,$$

where E_f is the result of the FEM by using COMSOL Multiphysics and E_r is the result of the present LRBFCM. All the computations are carried out on the same desktop with Intel(R) Core(TM) i7-2600 CPU, 3.40 GHz and 16 GB RAM. A minimum number of the meshes with acceptable results are employed to obtain higher computation speed in the FEM of COMSOL Multiphysics.

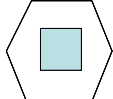
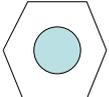
Lattice form		Square		Triangular	
Scatterer shape		Square	Circular	Square	Circular
					
RBF	Number of nodes	433	1017	727	775
	Degrees of freedom	538	1376	906	1014
	Time needed [s]	2.9550	7.098	4.3150	4.882
FEM	Degrees of freedom	2454	2058	1038	1584
	Time needed [s]	121	129	118	129
Comparison	Errors	0.0302	0.0312	0.0115	0.0364
	Time saving	97.55%	94.49%	96.34%	96.21%

Table 7.1 Computing time and accuracy comparisons for the aluminium/mercury phononic crystals.

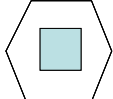
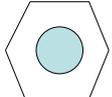
Lattice form		Square		Triangular	
Scatterer shape		Square	Circular	Square	Circular
					
RBF	Number of nodes	433	1011	727	775
	Degrees of freedom	538	1376	906	1014
	Time needed [s]	2.6660	7.098	4.3300	4.6930
FEM	Degrees of freedom	2454	2058	1038	1584
	Time needed [s]	121	122	118	129
Comparison	Errors	0.0030	0.0159	0.0091	0.0116
	Time saving	97.79%	94.18%	96.33%	96.36%

Table 7.2 Computing time and accuracy comparisons for the iron/air phononic crystals.

Table 7.1 and Table 7.2 show that the performance of the present LRBFCM proposed in this paper is much better than that of the FEM in general. Although the used degrees of freedom are different in both methods, we can conclude that the LRBFCM with a smaller number of nodes or degrees of freedom can reach a comparable accuracy as the FEM by using a larger number of the degrees of freedom, at least in the considered cases. A minimum element number with an acceptable accuracy in the numerical results is employed in the FEM to obtain a higher computational efficiency. In the case of the triangular lattice with square scatterers, the degrees of freedom in both methods are almost the same. However, the computing time needed by the FEM is much larger than that required by the LRBFCM. In all cases considered here, the saving in the computing time by using the present

LRBFCM is larger than 94%.

In Table 7.3, the efficiency and the accuracy of the presented LRBFCM in comparison with that of the FEM are given. Also here, the number of the used elements in the FEM is kept at a minimum to guarantee a satisfactory accuracy on the one hand and to reduce the required computing time on the other hand. Table 3 demonstrates again that the computational efficiency of the present LRBFCM is much higher than that of the FEM, at least for the considered fluid/solid phononic crystals. The accuracy of both methods is comparable, but the LRBFCM requires much less degrees of freedom compared with the FEM. Table 7.3 shows that the saving in the computing time by using the present LRBFCM is larger than 92% for the investigated water/iron phononic crystals.

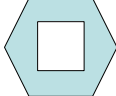
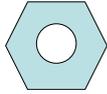
Lattice form		Square		Triangular	
Scatterer shape		Square	Circular	Square	Circular
					
RBF	Number of nodes	953	1676	727	803
	Degrees of freedom	1829	3132	1395	1485
	Time needed [s]	14.1170	26.027	10.068	9.370
FEM	Degrees of freedom	40513	42305	6057	2033
	Time needed [s]	375	364	165	139
Comparison	Errors	0.0011	0.0089	0.0078	0.0039
	Time saving	96.23%	92.84%	93.93%	93.25%

Table 7.3 Computing time and accuracy comparisons for the water/iron phononic crystals.

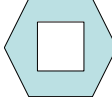
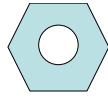
Lattice form		Square		Triangular	
Scatterer shape		Square	Circular	Square	Circular
					
RBF	Number of nodes	953	1676	727	803
	Degrees of freedom	1829	3132	1395	1485
	Time needed [s]	47.7660	129.3480	36.7830	49.3090
FEM	Degrees of freedom	40513	42305	6057	2033
	Time needed [s]	1793	1859	369	231
Comparison	Errors	0.0122	0.0078	0.0256	0.0136
	Time saving	99.88%	99.69%	90.03%	78.35%

Table 7.4 Computing time and accuracy comparisons for the air/iron phononic crystals.

Table 7.4 shows the comparisons of the computing time and the accuracy for the air/iron phononic crystals. Due to the existence of many flat bands, a larger number of the eigenvalues are needed to obtain the band structures by both the LRBFCM and the FEM. So the computing times in Table 7.4 are evaluated based on the numerical calculations of the first 100 eigenvalues by both the LRBFCM and the FEM. Here, we can see that the time saving by the present LRBFCM is more than 99% for the square lattice and more than 78% for the triangular lattice.

The accuracy in the case of the square lattice is evaluated by comparing the normalized eigenvalues that are smaller than 8 in the band structures of Fig. 7.16 and Fig. 7.19, while the accuracy for the triangular lattice is assessed by using the

normalized eigenvalues smaller than 7 in the band structures of Fig. 7.22 and Fig. 7.25. A comparison of Table 7.4 reveals that the numerical errors in the band structure calculations for the air/iron phononic crystals are generally larger than that for the water/iron phononic crystals due to the existence of many flat bands in the former case induced by the large acoustic impedance ratio. In the low frequency range, the numerically calculated flat bands by the present LRBFCM agree quite well with that by the FEM. However, the agreement between both results becomes worse in the high frequency range, which demands further validations and possible improvements in both methods.

7.4 Summary

In this chapter, the LRBFCM is presented for the band structure computations of the 2D solid/fluid and fluid/solid phononic crystals. Both systems of the periodic solid scatterers embedded in a fluid matrix (solid/fluid phononic crystals) and the periodic fluid scatterers embedded in a solid matrix (fluid/solid phononic crystals) are investigated by using the developed LRBFCM. The numerical results show that the present LRBFCM is suitable and accurate for computing the band structures of the 2D solid/fluid and fluid/solid phononic crystals when the shape parameter of the MQ RBF, the node distribution and the number of the involved local nodes are properly chosen. Numerical examples in this chapter also demonstrate that the present LRBFCM is much more efficient than the FEM for the band structure computations of the elastic and acoustic waves propagating in 2D solid/fluid and fluid/solid phononic crystals, when a comparable accuracy in both methods is required.

Chapter 8

Conclusions and outlook

8.1 Conclusions

In the present thesis, advanced radial basis function collocation methods (RBFCM) are developed and applied to the band structure computations of the one-dimensional (1D) and two-dimensional (2D) phononic crystals. Both the global and the local RBFCM are derived based on the strong-form formulation of the partial differential equations (PDEs) in conjunction with the corresponding boundary conditions and interface continuity conditions. The developed RBFCM represent a type of strong-form meshfree or meshless methods, which require only boundary and interior nodes instead of meshes or cells needed by the domain-type discretization methods like the FEM. Since the generation of distributed nodes is easier than the mesh or cell generation, the pre- and the post-processing as well as the adaptive implementation of the present RBFCM are advantageous in comparison with the domain-type discretization methods.

By utilizing the periodicity of the phononic crystals and based on the Bloch-theorem, a unit-cell with the appropriate periodic boundary conditions is considered. On the interface between the scatterer and the matrix, perfect continuity conditions for the displacement and stress components are assumed. The governing wave equations, the boundary conditions and the interface continuity conditions together form an eigenvalue problem for computing the dispersion relations or the band structures of the elastic or acoustic waves, which is solved numerically by using the developed RBFCM. In particular, three different special techniques, namely, the direct technique, the indirect technique and the fictitious nodes technique, are proposed for computing the spatial derivatives of the field quantities near or on the boundary/interface, which are required by the treatment of the boundary and the interface continuity conditions. These special techniques improve the stability and the accuracy of the conventional RBFCM significantly. Numerical examples for the

anti-plane elastic waves in 2D solid/solid phonic crystals as given in Chapter 5 illustrate that the direct and the indirect techniques outperform the fictitious nodes technique, though the latter is much more flexible with respect to the node distribution.

For the elastic wave propagation in 1D solid/solid phononic crystals, the effects of the shape parameter, the node distance and the type of the RBFs on the accuracy and the stability of the RBFCM are investigated and discussed, and a general rule for choosing the shape parameter is suggested. Besides, the influences of the node number and the node distribution (uniform and random) on the LRBFCM are also analysed for the anti-plane elastic waves in 2D phononic crystals. Then, the developed LRBFCM is extended and applied to the band structure calculations of the elastic waves in 2D solid/solid phononic crystals, and the elastic/acoustic waves in 2D solid/fluid (solid scatterers embedded in a fluid matrix) and fluid/solid (fluid scatterers embedded in an elastic solid matrix) phononic crystals. Since the acoustic impedance ratio is quite large, and the elastic and acoustic wave fields are rather different, the stability of the LRBFCM in this case is more severe than that in the case of the solid/solid phononic crystals, which demands a great deal of attention. The developed LRBFCM are verified by using the numerical results obtained by the FEM. A comparison with the FEM demonstrates that to guarantee a comparable accuracy the efficiency of the present LRBFCM is much higher than the FEM. This efficiency enhancement is attributed to the fact that the present LRBFCM rely on a strong-form formulation and do not involve any numerical integration required by the FEM based on the weak-form formulation of the PDEs.

Numerous representative numerical examples as presented in Chapters 4 to 7 show that the developed RBFCM in this thesis are accurate and efficient for the band structure calculations of the elastic and acoustic waves in 1D and 2D phononic crystals with different acoustic impedance ratios (small to large), material compositions (solid/solid, solid/fluid, fluid/solid), filling fractions (small to large) scatterer shapes (rectangular, square, circular and triangular), and lattice forms (square and triangular). By using these numerical examples, the effects of the key geometrical

and material parameters on the band structures, especially the passbands and the bandgaps, of 1D and 2D phononic crystals are also revealed and discussed.

8.2 Outlook

Based on the improved RBFCM presented in this thesis, further future research works on the topic are needed, which include for instance:

- Further improvement and extension of the three suggested special techniques, especially the fictitious technique, for computing the spatial derivatives of the field quantities near or on the boundaries and interfaces for more complex geometrical configurations.
- Further enhancement of the stability, the robustness and the flexibility of the RBFCM for the band structure calculations of elastic and acoustic waves in 2D phononic crystals.
- Sensitivity improvement of the RBFCM to the selections of the shape parameter and the type of the RBFs, the node number and the node distribution for 2D phononic crystals.
- Extension and applications of the present RBFCM to the band structure calculations of 3D phononic crystals.
- Extension and applications of the present RBFCM to transient wave propagation problems in 1D, 2D and 3D phononic crystals.

References

- [1] S.G. Johnson, J. D. Joannopoulos, Introduction to Photonic Crystals: Bloch's Theorem, Band Diagrams, and Gaps (but no defects), MIT, February (2003).
- [2] L Brillouin, Wave Propagation In Periodic Structures, John Wiley, New York, (1946).
- [3] E. Yablonovitch, Inhibited spontaneous emission in solid-state Physics and Electronics, *Physical Review Letters*, 58 (1987) 2059-2062.
- [4] S. John, Strong localization of photons in certain disordered dielectric superlattices, *Physical Review Letters*, 58 (1987) 2486-2489.
- [5] K.M. Ho, C.T. Chan, C.M. Soukoulis, Existence of a photonic gap in periodic dielectric structures, *Physical Review Letters*, 65 (1990) 3152-3155.
- [6] E. Yablonovitch, T.J. Gmitter, Photonic band structure: The face-centered-cubic case, *Physical Review Letters*, 63 (1989) 1950-1953.
- [7] E. Yablonovitch, T.J. Gmitter, K.M. Leung, Photonic band structure: The face-centered-cubic case employing nonspherical atoms, *Physical Review Letters*, 67 (1991) 2295-2298.
- [8] V. Narayanamurti, H.L. Störmer, M.A. Chin, A.C. Gossard, W. Wiegmann, Selective transmission of high-frequency phonons by a superlattice: the "dielectric" phonon filter, *Physical Review Letters*, 43 (1979) 2012-2016.
- [9] M.S. Kushwaha, P. Halevi, L. Dobrzynski, B. Djafari-Rouhani, Acoustic band structure of periodic elastic composites, *Physical Review Letters*, 71 (1993) 2022-2025.
- [10] R. Martinez-Sala, J. Sancho, J.V. Sanchez, V. Gomez, J. Llinares, F. Meseguer, Sound attenuation by sculpture, *Nature*, 378 (1995) 241-241.
- [11] F.R. Montero de Espinosa, E. Jiménez, M. Torres, Ultrasonic band gap in a periodic two dimensional composite, *Physical Review Letters*, 80 (1998) 1208-1211.
- [12] I. R. H. Olsson, I. El-Kady, Microfabricated phononic crystal devices and applications, *Measurement Science and Technology*, 20 (2009) 012002.
- [13] T. Gorishnyy, Hypersonic Phononic Crystals, PhD thesis, Department of Materials Science and Engineering at the Massachusetts Institute of Technology, (2007).
- [14] M.S. Kushwaha, P. Halevi, Band-gap engineering in periodic elastic composites, *Applied Physics Letters*, 64 (1994) 1085-1087.
- [15] M.S. Kushwaha, P. Halevi, G. Martínez, L. Dobrzynski, B. Djafari-Rouhani, Theory of acoustic band structure of periodic elastic composites, *Physical Review B*, 49 (1994) 2313-2322.
- [16] Z. Liu, C.T. Chan, P. Sheng, A.L. Goertzen, J.H. Page, Elastic wave scattering by periodic structures of spherical objects: theory and experiment, *Physical Review B*, 62 (2000) 2446-2457.
- [17] Z. Liu, X. Zhang, Y. Mao, Y.Y. Zhu, Z. Yang, C.T. Chan, P. Sheng, Locally resonant sonic materials, *Science*, 289 (2000) 1734-1736.
- [18] G. Wang, X. Wen, J. Wen, L. Shao, Y. Liu, Two-dimensional locally resonant phononic crystals with binary structures, *Physical Review Letters*, 93 (2004) 154302.
- [19] J.B. Li, Y.S. Wang, C. Zhang, Tuning of acoustic bandgaps in phononic crystals with helmholtz resonators, *Journal of Vibration and Acoustics*, 135 (2013) 031015-031015.
- [20] Y.F. Wang, Y.S. Wang, W. Litian, Complete bandgaps in three-dimensional holey phononic crystals with helmholtz resonators, in: *ultrasonics symposium (IUS), 2012 IEEE International*, 2012, 1766-1769.
- [21] Y.F. Wang, Y.S. Wang, Complete bandgaps in two-dimensional phononic crystal slabs with resonators, *Journal of Applied Physics*, 114 (2013) 043509.

- [22] R. James, S.M. Woodley, C.M. Dyer, V.F. Humphrey, Sonic bands, bandgaps, and defect states in layered structures-theory and experiment, *The Journal of the Acoustical Society of America*, 97 (1995) 2041-2047.
- [23] X.H. Wang, K.Q. Chen, B.Y. Gu, Localized mixed acoustic modes in superlattices with structural defects, *Journal of Applied Physics*, 92 (2002) 5113-5118.
- [24] M.M. Sigalas, Elastic wave band gaps and defect states in two-dimensional composites, *The Journal of the Acoustical Society of America*, 101 (1997) 1256-1261.
- [25] M.M. Sigalas, Defect states of acoustic waves in a two-dimensional lattice of solid cylinders, *Journal of Applied Physics*, 84 (1998) 3026-3030.
- [26] A. Khelif, B. Djafari-Rouhani, J.O. Vasseur, P.A. Deymier, P. Lambin, L. Dobrzynski, Transmittivity through straight and stublike waveguides in a two-dimensional phononic crystal, *Physical Review B*, 65 (2002) 174308.
- [27] A. Khelif, A. Choujaa, B. Djafari-Rouhani, M. Wilm, S. Ballandras, V. Laude, Trapping and guiding of acoustic waves by defect modes in a full-band-gap ultrasonic crystal, *Physical Review B*, 68 (2003) 214301.
- [28] A. Khelif, A. Choujaa, S. Benchabane, B. Djafari-Rouhani, V. Laude, Guiding and bending of acoustic waves in highly confined phononic crystal waveguides, *Applied Physics Letters*, 84 (2004) 4400-4402.
- [29] F. Wu, H. Zhong, S. Zhong, Z. Liu, Y. Liu, Localized states of acoustic waves in three-dimensional periodic composites with point defects, *The European Physical Journal B - Condensed Matter and Complex Systems*, 34 (2003) 265-268.
- [30] F.G. Wu, Z.Y. Liu, Y.Y. Liu, Splitting and tuning characteristics of the point defect modes in two-dimensional phononic crystals, *Physical Review E*, 69 (2004).
- [31] Z. Yan, Y.S. Wang, C.Z. Zhang, Wavelet method for calculating the defect states of two dimensional phononic crystals, *Acta Mechanica Solida Sinica*, 21 (2008) 104-109.
- [32] A.L. Chen, Y.S. Wang, G. Yu, Y.F. Guo, Z.D. Wang, Elastic wave localization in two-dimensional phononic crystals with one-dimensional quasi-periodicity and random disorder, *Acta Mechanica Solida Sinica*, 21 (2008) 517-528.
- [33] A.L. Chen, Y.S. Wang, Y.F. Guo, Z.D. Wang, Band structures of fibonacci phononic quasicrystals, *Solid State Communications*, 145 (2008) 103-108.
- [34] A.L. Chen, Y.S. Wang, Study on band gaps of elastic waves propagating in one-dimensional disordered phononic crystals, *Physica B: Condensed Matter*, 392 (2007) 369-378.
- [35] A.L. Chen, Y.S. Wang, J.B. Li, C.Z. Zhang, Localisation of elastic waves in two-dimensional randomly disordered solid phononic crystals, *Waves in Random and Complex Media*, 20 (2010) 104-121.
- [36] R.E. Vines, J.P. Wolfe, Scanning phononic lattices with surface acoustic waves, *Physica B: Condensed Matter*, 263-264 (1999) 567-570.
- [37] M. Torres, F.R. Montero de Espinosa, D. García-Pablos, N. García, Sonic band gaps in finite elastic media: surface states and localization phenomena in linear and point defects, *Physical Review Letters*, 82 (1999) 3054-3057.
- [38] Y. Tanaka, S.I. Tamura, Two-dimensional phononic crystals: surface acoustic waves, *Physica B: Condensed Matter*, 263-264 (1999) 77-80.
- [39] Z.Z. Yan, Y.S. Wang, Calculation of band structures for surface waves in two-dimensional phononic crystals with a wavelet-based method, *Physical Review B*, 78 (2008) 094306.

- [40] T.T. Wu, Z.G. Huang, S. Lin, Surface and bulk acoustic waves in two-dimensional phononic crystal consisting of materials with general anisotropy, *Physical Review B*, 69 (2004) 094301.
- [41] S. Benchabane, A. Khelif, J.Y. Rauch, L. Robert, V. Laude, Evidence for complete surface wave band gap in a piezoelectric phononic crystal, *Physical Review E*, 73 (2006) 065601.
- [42] A. Alvarez, Z. Ye, Effects of fish school structures on acoustic scattering, *ICES Journal of Marine Science: Journal du Conseil*, 56 (1999) 361-369.
- [43] R. Martínez-Sala, C. Rubio, L.M. García-Raffi, J.V. Sánchez-Pérez, E.A. Sánchez-Pérez, J. Linares, Control of noise by trees arranged like sonic crystals, *Journal of Sound and Vibration*, 291 (2006) 100-106.
- [44] B. Liang, B. Yuan, J.C. Cheng, Acoustic diode: rectification of acoustic energy flux in one dimensional systems, *Physical Review Letters*, 103 (2009) 104301.
- [45] B. Liang, X.S. Guo, J. Tu, D. Zhang, J.C. Cheng, An acoustic rectifier, *Nat Mater*, 9 (2010) 989-992.
- [46] S. Benchabane, A. Khelif, J.Y. Rauch, L. Robert, V. Laude, Evidence for complete surface wave band gap in a piezoelectric phononic crystal, *Physical Review E*, 73 (2006) 065601.
- [47] X. Zhang, Z. Liu, Y. Liu, F. Wu, Defect states in 2D acoustic band-gap materials with bend-shaped linear defects, *Solid State Communications*, 130 (2004) 67-71.
- [48] Y. Pennec, B. Djafari-Rouhani, J.O. Vasseur, H. Larabi, A. Khelif, A. Choujaa, S. Benchabane, V. Laude, Acoustic channel drop tunneling in a phononic crystal, *Applied Physics Letters*, 87 (2005) 261912.
- [49] M. Torres, F.R. Montero de Espinosa, Ultrasonic band gaps and negative refraction, *Ultrasonics*, 42 (2004) 787-790.
- [50] M. Ke, Z. Liu, C. Qiu, W. Wang, J. Shi, W. Wen, P. Sheng, Negative-refraction imaging with two dimensional phononic crystals, *Physical Review B*, 72 (2005) 064306.
- [51] S. Yang, J.H. Page, Z. Liu, M.L. Cowan, C.T. Chan, P. Sheng, Focusing of sound in a 3D phononic crystal, *Physical Review Letters*, 93 (2004) 024301.
- [52] F. Cervera, L. Sanchis, J.V. Sánchez-Pérez, R. Martínez-Sala, C. Rubio, F. Meseguer, C. López, D. Caballero, J. Sánchez-Dehesa, Refractive acoustic devices for airborne sound, *Physical Review Letters*, 88 (2001) 023902.
- [53] C. Qiu, Z. Liu, Acoustic directional radiation and enhancement caused by band-edge states of two dimensional phononic crystals, *Applied Physics Letters*, 89 (2006) 063106.
- [54] M.S. Kushwaha, P. Halevi, Giant acoustic stop bands in two-dimensional periodic arrays of liquid cylinders, *Applied Physics Letters*, 69 (1996) 31-33.
- [55] J.C. Hsu, T.T. Wu, Efficient formulation for band-structure calculations of two-dimensional phononic-crystal plates, *Physical Review B*, 74 (2006) 144303.
- [56] Z. Hou, B.M. Assouar, Modeling of Lamb wave propagation in plate with two-dimensional phononic crystal layer coated on uniform substrate using plane-wave-expansion method, *Physics Letters A*, 372 (2008) 2091-2097.
- [57] X.Z. Zhou, Y.S. Wang, C.Z. Zhang, Effects of material parameters on elastic band gaps of two dimensional solid phononic crystals, *Journal of Applied Physics*, 106 (2009) 014903.
- [58] Z.F. Mou F.G. Wu, X. Zhang, H.L. Zhong, Effect of translation group symmetry on phononic band gaps studied by supercell calculation, *Acta Physica Sinica*, 56 (2007) 4694-06
- [59] M.M. Sigalas, E.N. Economou, Elastic waves in plates with periodically placed inclusions, *Journal of Applied Physics*, 75 (1994) 2845-2850.

- [60] C. Charles, B. Bonello, F. Ganot, Propagation of guided elastic waves in 2D phononic crystals, *Ultrasonics*, 44, Supplement (2006) e1209-e1213.
- [61] J.J. Chen, H.L.W. Chan, J.C. Cheng, Large one-dimensional band gaps in three-component phononic crystal plates, *Physics Letters A*, 366 (2007) 493-496.
- [62] Y. Wang, F. Li, Y. Wang, K. Kishimoto, W. Huang, Tuning of band gaps for a two-dimensional piezoelectric phononic crystal with a rectangular lattice, *Acta Mechanica Sinica*, 25 (2009) 65-71.
- [63] Z.X. Ye, X.S. Zhu, L. Bin, C.J. Chun, Modulation of the bandgaps of in-plane elastic waves by out of plane wavenumber in the piezoelectric composite structures, *Smart Materials and Structures*, 20 (2011) 035009.
- [64] X. Zhang, Z.Y. Liu, J. Mei, Y.Y. Liu, Acoustic band gaps for a two-dimensional periodic array of solid cylinders in viscous liquid, *Journal of Physics: Condensed Matter*, 15 (2003) 8207.
- [65] M.M. Sigalas, J. Garcia, Importance of coupling between longitudinal and transverse components for the creation of acoustic band gaps: the aluminum in mercury case, *Applied Physics Letters*, 76 (2000) 2307-2309.
- [66] W. Axmann, P. Kuchment, An efficient finite element method for computing spectra of photonic and acoustic band-gap materials: I. scalar case, *Journal of Computational Physics*, 150 (1999) 468-481.
- [67] A. Khelif, B. Aoubiza, S. Mohammadi, A. Adibi, V. Laude, Complete band gaps in two dimensional phononic crystal slabs, *Physical Review E*, 74 (2006) 046610.
- [68] M. Aberg, P. Gudmundson, The usage of standard finite element codes for computation of dispersion relations in materials with periodic microstructure, *The Journal of the Acoustical Society of America*, 102 (1997) 2007-2013.
- [69] Y.F. Wang, Y.S. Wang, X.X. Su, Large bandgaps of two-dimensional phononic crystals with cross like holes, *Journal of Applied Physics*, 110 (2011) 113520.
- [70] Y.F. Wang, Y.S. Wang, Multiple wide complete bandgaps of two-dimensional phononic crystal slabs with cross-like holes, *Journal of Sound and Vibration*, 332 (2013) 2019-2037.
- [71] W. Liu, Y. Liu, X. Su, Z. Li, Finite element analysis of the interface/surface effect on the elastic wave band structure of two dimensional naosized phononic crystals, *International Journal of Applied Mechanics*, 06 (2014) 1450005.
- [72] Y. Tanaka, Y. Tomoyasu, S.I. Tamura, Band structure of acoustic waves in phononic lattices: Two-dimensional composites with large acoustic mismatch, *Physical Review B*, 62 (2000) 7387-7392.
- [73] T. Miyashita, C. Inoue, Numerical investigations of transmission and waveguide properties of sonic crystals by finite-difference time-domain method, *Japanese Journal of Applied Physics*, 40 (2001) 3488.
- [74] J.H. Sun, T.T. Wu, Propagation of surface acoustic waves through sharply bent two-dimensional phononic crystal waveguides using a finite-difference time-domain method, *Physical Review B*, 74 (2006) 174305.
- [75] Y. Cao, Z. Hou, Y. Liu, Finite difference time domain method for band-structure calculations of two dimensional phononic crystals, *Solid State Communications*, 132 (2004) 539-543.
- [76] J. Yuan, Y.Y. Lu, Photonic bandgap calculations with Dirichlet-to-Neumann maps, *Journal of the Optical Society of America A*, 23 (2006) 3217-3222.
- [77] J. Yuan, Y.Y. Lu, X. Antoine, Modeling photonic crystals by boundary integral equations and Dirichlet-to-Neumann maps, *Journal of Computational Physics*, 227 (2008) 4617-4629.

- [78] F.L. Li, Y.S. Wang, C.Z. Zhang, Bandgap calculation of two-dimensional mixed solid–fluid phononic crystals by Dirichlet-to-Neumann maps, *Physica Scripta*, 84 (2011) 055402.
- [79] N. Zhen, F.L. Li, Y.S. Wang, C.Z. Zhang, Bandgap calculation for mixed in-plane waves in 2D phononic crystals based on Dirichlet-to-Neumann map, *Acta Mechanica Sinica*, 28 (2012) 1143-1153.
- [80] N. Zhen, Y.S. Wang, C.Z. Zhang, Surface/interface effect on band structures of nanosized phononic crystals, *Mechanics Research Communications*, 46 (2012) 81-89.
- [81] N. Zhen, Y.S. Wang, C.Z. Zhang, Bandgap calculation of in-plane waves in nanoscale phononic crystals taking account of surface/interface effects, *Physica E: Low-dimensional Systems and Nanostructures*, 54 (2013) 125-132.
- [82] A. Sutradhar, G.H. Paulino, L.J. Gray, Transient heat conduction in homogeneous and non-homogeneous materials by the Laplace transform Galerkin boundary element method, *Engineering Analysis with Boundary Elements*, 26 (2002) 119-132.
- [83] F.J. Rizzo, D.J. Shippy, M. Rezayat, A boundary integral equation method for radiation and scattering of elastic waves in three dimensions, *International Journal for Numerical Methods in Engineering*, 21 (1985) 115-129.
- [84] L. C. Wrobel, M. H. Aliabadi, *The Boundary Element Method*, John Wiley: New York, (2002).
- [85] M. H. Aliabadi, *The Boundary Element Method: Applications in Solids and Structures*, John Wiley, New York, (2002).
- [86] F.L. Li, Y.S. Wang, C.Z. Zhang, G.L. Yu, Boundary element method for band gap calculations of two-dimensional solid phononic crystals, *Engineering Analysis with Boundary Elements*, 37 (2013) 225-235.
- [87] F.L. Li, Y.S. Wang, C.Z. Zhang, G.L. Yu, Bandgap calculations of two-dimensional solid–fluid phononic crystals with the boundary element method, *Wave Motion*, 50 (2013) 525-541.
- [88] F.L. Li, Y.S. Wang, Band gap analysis of two-dimensional phononic crystals based on boundary element method, in: *Ultrasonics Symposium, 2008. IUS 2008. IEEE, 2008.* 245-248.
- [89] V.P. Nguyen, T. Rabczuk, S. Bordas, M. Duflot, Meshless methods: A review and computer implementation aspects, *Mathematics and Computers in Simulation*, 79 (2008) 763-813.
- [90] X. Ben, H.L. Yi, X.B. Yin, H.P. Tan, Direct collocation meshless method for vector radiative transfer in scattering media, *Journal of Quantitative Spectroscopy and Radiative Transfer*, 163 (2015) 50-62.
- [91] Y. Gu, W. Chen, B. Zhang, Stress analysis for two-dimensional thin structural problems using the meshless singular boundary method, *Engineering Analysis with Boundary Elements*, 59 (2015) 1-7.
- [92] X. Zhang, P. Zhang, Meshless modeling of natural convection problems in non-rectangular cavity using the variational multiscale element free Galerkin method, *Engineering Analysis with Boundary Elements*, 61 (2015) 287-300.
- [93] B.J. Zheng, X.W. Gao, K. Yang, C.Z. Zhang, A novel meshless local Petrov-Galerkin method for dynamic coupled thermoelasticity analysis under thermal and mechanical shock loading, *Engineering Analysis with Boundary Elements*, 60 (2015) 154-161.
- [94] M. Ilati, M. Dehghan, The use of radial basis functions (RBFs) collocation and RBF-QR methods for solving the coupled nonlinear sine-Gordon equations, *Engineering Analysis with Boundary Elements*, 52 (2015) 99-109.
- [95] C.M. Fan, C.S. Chien, H.F. Chan, C.L. Chiu, The local RBF collocation method for solving the

- double-diffusive natural convection in fluid-saturated porous media, *International Journal of Heat and Mass Transfer*, 57 (2013) 500-503.
- [96] M. Dehghan, M. Abbaszadeh, A. Mohebbi, A meshless technique based on the local radial basis functions collocation method for solving parabolic-parabolic Patlak-Keller-Segel chemotaxis model, *Engineering Analysis with Boundary Elements*, 56 (2015) 129-144.
- [97] D. Stevens, H. Power, K.A. Cliffe, A solution to linear elasticity using locally supported RBF collocation in a generalised finite-difference mode, *Engineering Analysis with Boundary Elements*, 37 (2013) 32-41.
- [98] M.D. Buhmann, *Radial Basis Functions, Theory and Implementations*, Cambridge university press, (2003).
- [99] E.J. Kansa, Multiquadrics-A scattered data approximation scheme with applications to computational fluid-dynamics-II solutions to parabolic, hyperbolic and elliptic partial differential equations, *Computers & Mathematics with Applications*, 19 (1990) 147-161.
- [100] E.J. Kansa, Multiquadrics-A scattered data approximation scheme with applications to computational fluid-dynamics-I surface approximations and partial derivative estimates, *Computers & Mathematics with Applications*, 19 (1990) 127-145.
- [101] E. Oñate, S. Idelsohn, O.C. Zienkiewicz, R.L. Taylor, C. Sacco, A stabilized finite point method for analysis of fluid mechanics problems, *Computer Methods in Applied Mechanics and Engineering*, 139 (1996) 315-346.
- [102] S.N. Atluri, T.L. Zhu, The meshless local Petrov-Galerkin (MLPG) approach for solving problems in elasto-statics, *Computational Mechanics*, 25 (2000) 169-179.
- [103] M.A. Golberg, C.S. Chen, The method of fundamental solutions for potential, helmholtz and diffusion problems, In M.A. Golberg, editor, *Boundary Integral Methods: Numerical and Mathematical Aspects*, (1998) 103-176.
- [104] W. Chen, M. Tanaka, A meshless, integration-free, and boundary-only RBF technique, *Computers & Mathematics with Applications*, 43 (2002) 379-391.
- [105] G.R. Liu, K.Y. Dai, K.M. Lim, Y.T. Gu, A point interpolation mesh free method for static and frequency analysis of two-dimensional piezoelectric structures, *Computational Mechanics*, 29 (2002) 510-519.
- [106] M. Zerroukat, H. Power, C.S. Chen, A numerical method for heat transfer problems using collocation and radial basis functions, *International Journal for Numerical Methods in Engineering*, 42 (1998) 1263-1278.
- [107] B. Sarler, A radial basis function collocation approach in computational fluid dynamics, *Computer Modeling in Engineering & Sciences*, 7 (2005) 185-193.
- [108] W.R. Madych, S.A. Nelson, Multivariate interpolation and conditionally positive definite functions. II, *Mathematics of Computation*, 54 (1990) 211-230.
- [109] C. Micchelli, Interpolation of scattered data: Distance matrices and conditionally positive definite functions, *Constructive Approximation*, 2 (1986) 11-22.
- [110] X. Zhang, K.Z. Song, M.W. Lu, X. Liu, Meshless methods based on collocation with radial basis functions, *Computational Mechanics*, 26 (2000) 333-343.
- [111] W. Chen, New RBF collocation schemes and kernel RBFs with applications, *Lecture Notes in Computational Science and Engineering*, 26 (2002) 75-86.
- [112] E.J. Kansa, Y.C. Hon, Circumventing the ill-conditioning problem with multiquadric radial basis functions: applications to elliptic partial differential equations, *Computers & Mathematics with*

- Applications, 39 (2000) 123-137.
- [113] M.D. Nam, C.T. Thanh, Mesh-free radial basis function network methods with domain decomposition for approximation of functions and numerical solution of Poisson's equations, *Engineering Analysis with Boundary Elements*, 26 (2002) 133-156.
- [114] C. Shu, H. Ding, K.S. Yeo, Local radial basis function-based differential quadrature method and its application to solve two-dimensional incompressible Navier–Stokes equations, *Computer Methods in Applied Mechanics and Engineering*, 192 (2003) 941-954.
- [115] N.A. Libre, A. Emdadi, E.J. Kansa, M. Rahimian, M. Shekarchi, A stabilized RBF collocation scheme for neumann type boundary value problems, *Computer Modeling in Engineering and Science*, 24 (2008) 61-80.
- [116] C.S. Chen, M. Ganesh, M.A. Golberg, A.H.D. Cheng, Multilevel compact radial functions based computational schemes for some elliptic problems, *Computers & Mathematics with Applications*, 43 (2002) 359-378.
- [117] Y.C. Hon, R. Schaback, X. Zhou, An adaptive greedy algorithm for solving large RBF collocation problems, *Numerical Algorithms*, 32 (2003) 13-25.
- [118] L. Ling, R. Schaback, Stable and convergent unsymmetric meshless collocation methods, *SIAM Journal on Numerical Analysis*, 46 (2008) 1097-1115.
- [119] C.S. Huang, C.F. Lee, A.H.D. Cheng, Error estimate, optimal shape factor, and high precision computation of multiquadric collocation method, *Engineering Analysis with Boundary Elements*, 31 (2007) 614-623.
- [120] C.K. Lee, X. Liu, S.C. Fan, Local multiquadric approximation for solving boundary value problems, *Computational Mechanics*, 30 (2003) 396-409.
- [121] B. Sarler, R. Vertnik, Meshfree explicit local radial basis function collocation method for diffusion problems, *Computers & Mathematics with Applications*, 51 (2006) 1269-1282.
- [122] D. Stevens, H. Power, C.Y. Meng, D. Howard, K.A. Cliffe, An alternative local collocation strategy for high-convergence meshless PDE solutions, using radial basis functions, *Journal of Computational Physics*, 254 (2013) 52-75.
- [123] Y.C. Hon, B. Šarler, D.F. Yun, Local radial basis function collocation method for solving thermo-driven fluid-flow problems with free surface, *Engineering Analysis with Boundary Elements*, 57 (2015) 2-8.
- [124] W. Li, X. Liu, G. Yao, A local meshless collocation method for solving certain inverse problems, *Engineering Analysis with Boundary Elements*, 57 (2015) 9-15.
- [125] H.Y. Hu, J.S. Chen, W. Hu, Weighted radial basis collocation method for boundary value problems, *International Journal for Numerical Methods in Engineering*, 69 (2007) 2736-2757.
- [126] H.Y. Hu, J.S. Chen, W. Hu, Weighted radial basis collection method for boundary value problems, *International Journal for Numerical Methods in Engineering*, 69 (2007) 2736-2757.
- [127] L. Wang, J.S. Chen, H.Y. Hu, Radial basis collocation method for dynamic analysis of axially moving beams, *Interaction and Multiscale Mechanics*, 2 (2009) 19.
- [128] S.W. Chi, J.S. Chen, H.Y. Hu, A weighted collocation on the strong form with mixed radial basis approximations for incompressible linear elasticity, *Computational Mechanics*, 53 (2014) 15.
- [129] G. Wang, J. Wen, Y. Liu, X. Wen, Lumped-mass method for the study of band structure in two-dimensional phononic crystals, *Physical Review B*, 69 (2004) 184302.
- [130] C. Goffaux, J. Sánchez-Dehesa, Two-dimensional phononic crystals studied using a variational method: Application to lattices of locally resonant materials, *Physical Review B*, 67 (2003)

144301.

- [131] Z.Z. Yan, C.Z. Zhang, Y.S. Wang, Elastic wave localization in two-dimensional phononic crystals with one-dimensional random disorder and aperiodicity, *Physica B: Condensed Matter*, 406 (2011) 1154-1161.
- [132] X. Checoury, J.M. Lourtioz, Wavelet method for computing band diagrams of 2D photonic crystals, *Optics Communications*, 259 (2006) 360-365.
- [133] W. Kohn, N. Rostoker, Solution of the Schrödinger equation in periodic lattices with an application to metallic lithium, *Physical Review*, 94 (1954) 1111-1120.
- [134] L.M. Li, Z.Q. Zhang, Multiple-scattering approach to finite-sized photonic band-gap materials, *Physical Review B*, 58 (1998) 9587-9590.
- [135] L. Rayleigh, On the remarkable phenomenon of crystalline reflexion described by Prof. Stokes, *Philosophical Magazine Series 5*, 26 (1888) 256-265.
- [136] H. Zheng, C. Zhang, W. Chen, J. Sladek, V. Sladek, The radial basis function methods for wave propagation analysis, *International Conference on Boundary Elements and Meshless Techniques*, (2013) 243-250.
- [137] E.E. Hart, S.J. Cox, K. Djidjeli, Compact RBF meshless methods for photonic crystal modelling, *Journal of computational physics*, 230 (2011) 4910-4921.
- [138] B. Fornberg, C. Piret, On choosing a radial basis function and a shape parameter when solving a convective PDE on a sphere, *Journal of Computational Physics*, 227 (2008) 2758-2780.
- [139] G.E. Fasshatier, J.G. Zhang, On choosing "optimal" shape parameters for RBF approximation, *Numerical Algorithms*, 45 (2007) 345-368.
- [140] C.H. Tsai, J. Kolibal, M. Li, The golden section search algorithm for finding a good shape parameter for meshless collocation methods, *Engineering Analysis with Boundary Elements*, 34 (2010) 738-746.
- [141] S. Hernandez, I. Flores, J.A. Vazquez, Improved golden-section algorithm for the multi-item replenishment problem, *Journal of Applied Research and Technology*, 10 (2012) 388-397.
- [142] E.E. Hart, S.J. Cox, K. Djidjeli, V.O. Kubytskyi, Solving an eigenvalue problem with a periodic domain using radial basis functions, *Engineering Analysis with Boundary Elements*, 33 (2009) 258-262.
- [143] H. Zheng, C.Z. Zhang, Y.S. Wang, J. Sladek, V. Sladek, A meshfree local RBF collocation method for anti-plane transverse elastic wave propagation analysis in 2D phononic crystals, *Journal of Computational Physics*, 305 (2015) 997-1014.
- [144] H. Zheng, C.Z. Zhang, Y.S. Wang, J. Sladek, V. Sladek, Band structure computation of in-plane elastic waves in 2D phononic crystals by a meshfree local RBF collocation method, *Engineering Analysis with Boundary Elements*, 66 (2016) 77-90.

Publications

- [1] **Hui Zheng**, Wen Chen, Chuanzeng Zhang. Multi-domain boundary knot method for ultra-thin coating problems. *Computer Modeling in Engineering & Sciences*; 90 (2013): 179-195
- [2] **Hui Zheng**, Chuanzeng Zhang, Wen Chen, Jan Sladek, Vladimir Sladek. The Radial Basis Function Methods for Wave Propagation Analysis. *International Conference on Boundary Elements and Meshless Techniques*; 2013
- [3] **Hui Zheng**, Chuanzeng Zhang, Yuesheng Wang, Jan Sladek, Vladimir Sladek. A meshfree local RBF collocation method for anti-plane transverse elastic wave propagation analysis in 2D phononic crystals. *Journal of Computational Physics*; 305 (2015): 997-1014
- [4] **Hui Zheng**, Chuanzeng Zhang, Yuesheng Wang, Jan Sladek, Vladimir Sladek. Band structure calculations of in-plane elastic waves in 2D phononic crystals by a meshfree RBF collocation method. *Engineering Analysis with Boundary Elements*; 66 (2016): 77-90
- [5] **Hui Zheng**, Chuanzeng Zhang, Yuesheng Wang, Wen Chen, Jan Sladek, Vladimir Sladek. A local RBF collocation method for band structure computations of 2D solid/fluid and fluid/solid phononic crystals. *International Journal for Numerical Methods in Engineering*; in press, 2016
- [6] Chunqiu Wei, Zhizhong Yan, **Hui Zheng**, Chuanzeng Zhang. RBF collocation method and stability analysis for phononic crystals. *Applied Mathematics and Mechanics*; 37 (2016): 627-638
- [7] Zhizhong Yan, Chunqiu Wei, **Hui Zheng**, Chuanzeng Zhang. Phononic band structures and stability analysis using radial basis function method with consideration of different interface models. *Physica B: Condensed Matter*; 489 (2016): 1-11